Title

Characterization of Ion Transport in Liquid Electrolytes by Combining Electrochemical Methods and Electrophoretic NMR

Author

Hickson, Darby

Publication Date

2024

Peer reviewed|Thesis/dissertation

Characterization of Ion Transport in Liquid Electrolytes by Combining Electrochemical Methods and Electrophoretic NMR

By

Darby Hickson

A dissertation submitted in partial satisfaction of the

requirements for the degree of

Doctor of Philosophy

in

Chemical Engineering

in the

Graduate Division

of the

University of California, Berkeley

Committee in charge:

Professor Nitash Balsara, Chair
Professor Bryan McCloskey
Professor Gerbrand Ceder

Summer 2024

Characterization of Ion Transport in Liquid Electrolytes by Combining Electrochemical Methods and Electrophoretic NMR

Abstract

Characterization of Ion Transport in Liquid Electrolytes by Combining Electrochemical Methods and Electrophoretic NMR

by

Darby Hickson

Doctor of Philosophy in Chemical Engineering

University of California, Berkeley

Professor Nitash P. Balsara, Chair

Improving ion transport in the electrolyte is important for developing lithium-ion batteries that can meet increasingly demanding applications, including low temperature cycling and fast charging. All practical battery electrolytes are composed of concentrated solutions that are difficult to fully characterize due to ion-ion interactions, cation solvation, and thermodynamic nonidealities. Although conductivity is often used as the primary metric to screen the viability of a given electrolyte, electrolytes are only fully described with two additional transport properties – the salt diffusion coefficient and cation transference number with respect to the solvent velocity – and a thermodynamic factor. Newman's concentrated theory provides a framework to study these properties, which has been extensively used to describe polymer electrolytes. This methodology involves four independent experiments that can be combined to determine the cation transference number. Error from each experiments compounds and reduces precision in the derived transference number. Characterization of liquid electrolytes poses additional challenges because of the inherent reactivity against lithium metal.

In this Dissertation, we present and implement a new method for characterizing liquid electrolytes by combining electrochemical methods with electrophoretic NMR. In Chapter 2, we detail this novel methodology for characterizing bulk ion transport in liquid electrolytes for an exemplar electrolyte, LiTFSI salt dissolved in tetraglyme. Electrochemical characterization involves ac impedance spectroscopy to measure conductivity, restricted diffusion to measure salt diffusion coefficient, polarization experiments to measure current fraction, and concentration cells to measure the change in open circuit potential with respect to log of molality. In accordance with traditional methods, these four experiments are combined to give estimates of the transference number and thermodynamic factor. The intrinsic coupling between parameters obtained by electrochemical methods results in large error bars in the transference number that obscure the transport behavior of the electrolyte. We use electrophoretic NMR to directly determine electric-field-induced cation, anion, and solvent velocities to determine the cation transference number. Electrophoretic NMR more precisely determines cation transference numbers and additionally enables precise determination of the thermodynamic factor. This method demonstrates a more robust approach for complete characterization of battery electrolytes.

We use and evaluate this methodology for the remainder of the dissertation. In Chapter 3, we examine the issues of low temperature ion transport. Sluggish ion transport through the electrolytic phase leads to poor performance at low temperatures for rechargeable batteries. We study the dependence of transport and thermodynamic properties over a wide temperature range, between -20 and 45°C. At cold temperatures, species in the electrolyte tend to move slower, leading to decreases in conductivity, salt diffusion coefficient, and cation and anion velocities. However, the cation transference number can have a nonmonotonic dependence on temperature depending on salt concentration. This behavior is strongly linked to the solvent velocity. The overall impact of worsened transport at cold temperatures is a predicted steady current for a given polarization that's two orders of magnitude lower than at warm or ambient temperatures.

Chapter 4 reexamines the discrepancy in the transference number between electrochemical methods and electrophoretic NMR. We use concentrated solution theory to predict concentration and potential gradients using two methods – one based on transference numbers from electrochemical methods and one based on transference number measured via electrophoretic NMR. Due to more negative transference numbers, the modeled concentration gradients are larger for electrochemical methods compared to electrophoretic NMR. We find that the expected potential gradients, however, are remarkably similar. Based on current-voltage relationships alone, it is not possible to distinguish between the two transference numbers, calling into question the unique determination of this parameter.

In Chapters 5 and 6, we further examine ion transport in glyme-based electrolytes. In Chapter 5, we examine the impact of chain length on ion transport in oligoether solvents, including tetraglyme, pentaglyme, and octaglyme. We find adding even one repeat unit to the solvent drastically lowers conductivity, diffusion coefficient, and cation and anion velocities. The transference numbers measured in these three electrolytes shows a characteristic "V-shaped" dependence on salt concentration. The minimum in the transference number is well predicted by cation solvation motifs determined in molecular dynamic simulations. In Chapter 6, we study the impact of high salt concentration on transport properties. Similar to the results of Chapter 3 and Chapter 5, we find increased viscosity at high salt concentrations causes a decrease in conductivity, salt diffusion coefficient, and cation and anion velocities. At high salt concentrations, we also find the transference number is near or below zero. Predicted concentration and potential gradients indicate concentration polarization is much worse at high concentrations due to the worsening of transport properties.

This work describes a new, robust methodology for studying ion transport in liquid electrolytes. This technique is used to evaluate the impact of various factors on ion transport, including temperature, salt concentration, and solvent chain length.

Table of Contents

List of Figures

List of Tables

Acknowledgments

No part of my academic journey has taken a village quite like my PhD. I am eternally grateful to the many people that make up my village for the endless support I was given over the past five years.

Nitash, I am so thankful for the guidance and mentorship you provided. You gave me immense freedom to pursue what was most interesting to me and supported me in turning fledgling ideas into finished projects. Your passion for science was contagious and I've learned so much from you. Most importantly, you've cultivated a wonderful group culture that values collaboration, mentorship, and friendship, and I will always be grateful that I had the opportunity to work in this group.

I think one of the greatest strengths of the Balsara Lab is the post-docs. Every post-doc I worked with had the great Balsara Lab combo of being incredibly hardworking, wonderful mentors, and great fun. Hee Jeung and I barely overlapped at all, but you made me feel instantly welcomed and included in the group. Youngwoo, even though we never worked together on a project, I learned much from your scientific contributions. Louise, you met with me when I still didn't know anything about electrochemistry and were extremely patient with all of my questions. I only started to feel like I knew what I was doing after your generous mentorship. You always cultivated a great group culture by getting people together for happy hours and other social events, a practice we've tried our best to continue since you left. Xiaopeng, you are a dedicated researcher and an innovative thinker. You also helped me with lab maintenance tasks, especially ones I was too weak to do, for which I am very grateful. Jaeyong, you're a great researcher and somehow manage to do the work of several people. I've learned so much from you, and you've always been willing to teach me something new. You're also an amazing cook, and I've enjoyed eating your food on ski trips and barbecues immensely. Rounak, I've loved having you as a desk buddy and getting to know you since you joined. Thank you for answering my panicked synthesis questions and laughing with me when things fail. Keisuke, you've just joined the lab but I've already learned so much from you. The lab is lucky to have you.

David and Saheli, I owe you extra special thanks. Saheli, I loved sitting by your desk in Tan. You are a great scientist and have an immense talent for synthesis - I am deeply grateful to have learned from you. You fostered an excellent boba culture in the group and I always enjoyed all of the long conversations we got to have about research failings, family, and life. You helped me not to be too emotionally attached to my work and helped me see that failures in science are normal and expected. David – I honestly don't know what I would have done in my PhD if we hadn't developed this wonderful collaboration between electrochemistry and eNMR. Your scientific contributions and mentorship are present throughout this dissertation. I have learned so much from you, and I am grateful for your constant advice, whether it be on presentation slides or data analysis. I wish you the best setting up your new lab, you're going to be an amazing professor.

Deep, Jackie, and Whitney were the leaders of the group when I joined and set the tone for my expectations of lab culture and what I could aspire to achieve during my PhD. You are all brilliant people while also being extremely fun to be around. Deep, you established the path for me to do liquid characterization in an entirely polymers group. I've learned so much from your work and

your papers. Whitney and Jackie, you've both been kind and helpful to me post-leaving the lab, and I'm very grateful to know you both.

Mike, you helped mentor me during a very difficult period of adjusting to working in the lab in a new-to-me research field and adjusting to working during a worldwide pandemic while I still knew nothing. I'm grateful you helped me move to Tan – I think that changed the trajectory of my PhD for the better. You also have an amazing, capable attitude when it comes to dealing with challenging problems, which inspired me whenever I encountered issues (especially equipment related) later on. Gumi, your kindness about mentorship has stayed with me. You were always willing to answer questions, regardless of how small or silly, and I always aimed to be like that when mentoring people myself.

Kevin, you contributed so much scientifically to the group and I learned so much from your careful characterization of electrolytes. Lorena, I honestly can't imagine going through grad school without knowing you (partly because our conversations at recruitment convinced me to come to Berkeley). You have been such a mentor to me, answering my same repeated questions about NMR or lab safety responsibilities or whatever, but you are also one of kindest and most generous people I met during grad school. You're an amazing teacher and all of your future students are so lucky to have you.

Neel, Alec, and Zach, I think you guys were the best group of students to have in the year directly ahead of me. You all represent the best of the Balsara Lab culture, being incredibly smart, hardworking, and kind, and also being great friends. Neel, you were the best Tan Hall buddy. Our cathartic complaining about failed experiments and the frustrations of science in the dungeon or over boba helped me push through hard times and deal with setbacks. Thank you for all of your advice. You're a great friend and I'm grateful to know you. Zach – you're a great scientist but an even better person. I lost track of all of the electrochemistry questions I asked you during your time at Berkeley, but I owe so much of my understanding of echem and ion transport to you. Alec, you're a brilliant scientist and I'm glad I had the opportunity to learn about x-ray tomography from you. I'm grateful for the great beamtime parties we've had, but I do wish you were worse at games, especially Monopoly Deal.

Morgan, my cohort and lab buddy, I'm so grateful you're staying in the Bay so we can still hang out. You're a great researcher and a wonderful scientific communicator – which is why I feel like I understand your research even though it has nothing to do with mine. Despite the fact you did a completely different project from what people in our group typically research, you found ways to establish yourself as a leader and fostered a welcoming environment – whether it be in summer softball or through social events.

Vivaan, you are the perfect person to take over as leader of the group for this upcoming year. You are generous and kind when it comes to mentorship and smart and hardworking on your own projects. I've had so much fun talking to you about your projects, especially late at night at the beamline, and have learned so much from you. You're never afraid to ask a question and that's what makes you such a great scientist. You've also made some delicious baked goods and I've loved our conversations and books and life.

Emily, Michael and Lily, you have all developed so much as researchers during your time at Berkeley and it's impressive to see the work that you've done. Lily, you're a very unique person

and you add a lot to the energy of our group. You've already studied so many different systems and techniques while in the group and I look forward to seeing what you accomplish. Emily, I'm awed by you and how smart, hardworking, and competent you are. You're an excellent leader and I can only imagine what you'll do during the rest of your PhD. You've also been a great friend, and I've enjoyed talking about books (the good and the bad), food and cooking, and of course, Crybaby nights. Michael, I'm impressed by the tenacity you've shown in dealing with experimental challenges. I've learned so much from you asking challenging questions and pushing on the limits of our understanding of electrodes and electrolytes. Hanging out at the beamline with you is always fun and I'll forever be impressed by how well you can function on no sleep.

Zirong, I'm already so impressed by what you've learned and accomplished in your first year. I knew the future direction of the lab would be good when you joined, and I can see you're on your way to becoming a truly excellent scientist.

I was fortunate enough to work with several undergraduate researchers during my time at Berkeley. Aakash, you made great contributions to the low temperature project and I enjoyed working with you. Quynh Nhi, it has been such a joy to work with you. You're a careful scientist and very driven – I know you'll accomplish whatever you set out to do. I am very grateful for the contributions you made to Chapter 5 of this work. Julia, although I was not your mentor, it was great working with you on the eNMR/echem collaboration. You have the talent of a researcher much later in their career, and I know you'll go on to do great things.

I am grateful to people outside of the group who contributed to my understanding of various concepts related to this work. Helen Bergstrom, you were very helpful to me early on as I struggled to do electrochemical experiments. I am grateful for your help and scientific discussions. Dr. Chris Takacs, you are brilliant and manage to take on the responsibilities of multiple jobs. I wish we could have done more with our x-ray microscopy collaboration, but I'm so grateful to have worked with you and learned from you.

I am grateful to the administrative support offered by Joseph Nolan and Carlet Altamirano over the last five years. I am also grateful to facility support, including Carl Lamey in Shipping and Receiving and Douglas Scudder and Clint Jessel in the Machine Shop. Doug, I enjoyed our talks about family and the Midwest greatly.

Friendships outside of lab have also been essential. I am also deeply grateful to be a part by the 2019 Cohort. Since day one, you all have been amazing people to hang out and not talk about science with. I am especially grateful for the Loud House friendships, I've loved going to wine country, game nights, and cohort trips with all of you. I am also grateful that I had the opportunity to be a part of two book clubs during grad school – I've loved reading books and learning with all of you.

Joining a lab two months before the start of a global pandemic created a lot of unexpected challenges. I am deeply grateful to several friends from before grad school who provided emotional support throughout the last five years - Gina, Rachel, Karine, Embud, Lexi, and Katie. Whether on extended phone calls or facetimes at the beginning of the pandemic or during visits later on, I am so grateful to have each of your in my life.

I owe so much to my family, who raised me to value education and gave me to the tools and support to embark on this journey. I want to first thank my grandparents – Grandpa Robin,

Grandma Anne, Grandma Eleanor, Grandpa Jordan, and Grandma Mary – who showed up at graduations and taught me how important school was. To my parents, I owe you everything. You always supported me to do what I wanted, but never pushed me too hard in any direction. I am grateful for the freedom you gave me to argue, think independently, and explore life on my own. I am so thankful to my sister, Hayley, who takes credit for teaching me how to read. You have been a huge support for me since childhood. Living in the Bay with you has been so fun, and I'm deeply grateful to you and Pranav for letting me move in during the pandemic.

Finally, I want to thank my partner, Mark. You have been the greatest support and empowered me to trust myself when that was most difficult. I have learned so much about coding from you, which has helped with various parts of this work. You're so smart and it's so cool how much of this dissertation you'll probably understand. You've pushed me intellectually and encouraged me to keep going through failures and frustrations, and I am forever thankful to know you.

FUNDING ACKNOWLEDGMENT

Early work in this thesis was supported by the Assistant Secretary for Energy Efficiency and Renewable Energy, Vehicle Technologies Office, of the U.S. Department of Energy under Contract DE-AC02-05CH11231, under the Low Temperature Electrolyte program. Later work was supported by the Vehicle Technologies Office of the U.S. Department of Energy's Office of Energy Efficiency and Renewable Energy under the guidance of the Advanced Battery Cell Research Program (eXtreme fast charge Cell Evaluation of Lithium-ion batteries, XCEL). Hard x-ray experiments were performed at the Advanced Light Source, which is supported by the Director, Office of Science, Office of Basic Energy Sciences, of the U.S. Department of Energy under Contract No. DE-AC02-05CH11231. The NMR instrument used in this work was supported by the National Science Foundation under grant no. 2018784.

1 Introduction

1.1 Motivation

The transportation sector is the largest producer of greenhouse gas emissions in the U.S., accounting for almost 30% of total emissions.[1] The electrification of personal vehicles is one method to reduce the emissions associated with transportation. Over the last decade, the sale and use of electric vehicles (EVs) has dramatically increased due to the improvement in lithium-ion batteries. Batteries for electric vehicles still need to bolster reliability and range in order to appeal to the consumer, which requires improvement in battery technology related to safety, cost, discharge rates, and energy density.[1] One of the main challenges impacting lithium-ion batteries today is worsened performance at low temperatures, which is a major hindrances to the adoption of EVs in colder climates.[2–4] The state-of-the-art lithium-ion battery includes a graphitic anode, a carbonate-based liquid electrolyte, and a transition-metal-oxide cathode. Current lithium-ion battery electrolytes comprise mixtures of solvents such as ethylene carbonate (EC), a high dielectric constant solvent with high viscosity, and dimethyl carbonate (DMC), a low dielectric constant solvent with low viscosity. A large portion of the literature has focused on increasing ionic conductivities in these electrolytes and improving long-term cycling properties for lithium-ion batteries. However, there is still much to learn about the mechanisms of ion transport in liquid electrolytes. The goal of this work is to understand the impact of various factors on ion transport to elucidate rational design strategies for improved liquid electrolytes.

1.2 Ion Transport

Newman's concentrated solution theory provides a framework for describing ion transport in concentrated electrolyte solutions using measurable transport properties.[5] Three transport properties can fully describe a simple, binary electrolyte. These three properties are the ionic conductivity, the salt diffusion coefficient, and the cation transference number with respect to the solvent velocity. A thermodynamic factor describing the ideality of the electrolyte should also be known.

Ionic conductivity describes the ability of an electrolyte to conduct current and reflects the total movement across all ions in response to an applied electric field. The salt diffusion coefficient describes the relaxation of all ions in response to concentration gradients. The cation transference number describes the proportion of the current carried by the cation in an electrolyte of uniform composition. We use a solvent reference frame to measure and report the transference number. The thermodynamic factor quantifies the change in mean molal salt activity coefficient with salt concentration; deviations from ideality in concentrated solutions reflect ion-ion interactions and ion-solvent interactions. In traditional electrochemical characterization methods, the transference number and thermodynamic factor are derived parameters. They can be determined by combining measurements of ionic conductivity and salt diffusion coefficient with two additional experiments – current fraction measured in chronoamperometry experiments and concentration cell experiments.[6–8] Additional information about experimental methods is given in Chapter 2. The combination of multiple independent experiments to determine one parameter compounds error and reduces precision in the derived parameters.[9] Characterization of liquid electrolytes is

especially challenging, given the need for polarization experiments conducted in lithium-lithium symmetric cells and the inherent reactivity of liquid electrolytes against lithium metal.

The cation transference number can be determined directly from other techniques. One of these methods is electrophoretic NMR (eNMR), a technique in which cation, anion, and solvent velocities can be directly measured under an applied electric field.[10–12] eNMR is an extension of nuclear magnetic resonance spectroscopy (NMR), a nucleus specific technique that distinguishes isotopes by their resonance frequencies. There is one NMR active species in the cation (^{7}Li), anion (^{19}F), and the solvent (^{1}H). ENMR applies a magnetic and an electric field, which induces ion migration, for a very short period of time. The average distance each species moves is used to determine species' velocities individually for the cation, anion, and solvent. The cation transference number is directly related to these three velocities.[13] The transference number can be combined with concentration cell experiments to determine the thermodynamic factor. Combining electrochemical methods with electrophoretic NMR enables complete characterization of liquid electrolytes with greater precision in both the transference number and the thermodynamic factor. The complete characterization of all transport and thermodynamic properties of an electrolyte enables the prediction of concentration gradients, potential gradients, and the limiting current.[14] More information on these predictions is given in Chapters 3 and 4.

1.3 Glyme-Based Electrolytes

Oligoether glyme-based solvents have been widely studied for their potential as liquid electrolytes in various battery technologies due to their stability and nonflammability compared to conventional carbonate electrolytes.[15] A glyme-based solvent has the molecular structure of $CH_3O[CH_2CH_2O]_nCH_3$. All glymes strongly solvate lithium cations due to electronegative oxygens on the solvent backbone. Depending on the size of the solvent molecule, salt concentration, and temperature, the mechanism of solvation and ion-ion interactions can vary greatly.[16–18] The mechanism of ion transport in various glyme solvents has been the focus of many modeling studies.[19–23] The longest glyme solvent, poly(ethylene oxide), or PEO, conducts ions via an ion-hopping mechanism due to the interconnectivity of polymer chains.[20,21,23] Liquid glyme solvents tend to conduct ions via a vehicular mechanism.[19] Some comparative studies on smaller glymes, such as monoglyme, diglyme, triglyme, and tetraglyme, already exist.[16,17,24] Little work has been done to bridge the gap in understanding of ion transport in low molecular weight glyme-based liquid solvents and polymeric glymes.

Chain length in glyme-based solvents drastically impacts transport properties and the overall utility of a given electrolyte. Due to the differences in mechanism of ion conduction, the residence time of solvation also varies greatly with chain length. Transport and thermodynamic properties are also strongly dependent on salt concentration. Glyme-based electrolytes are an interesting candidate to evaluate the impact of concentration on transport properties, as a significant body of work exists evaluating the solvation structure of glymes containing lithium salts.[15,25–29] Research has specifically focused on distinguishing between electrolytes that function as concentrated solutions or as solvate ionic liquids (SILs).[18,30–34] This classification is entirely salt concentration dependent.

1.4 Structure of the Dissertation

This dissertation characterizes ion transport in liquid electrolytes using a novel method that combines electrochemical methods with electrophoretic NMR.

Chapter 2 introduces this methodology and compares obtained transference numbers and thermodynamic factors with conventional techniques. Chapter 3 uses this technique to investigate the challenges with ion transport at low temperatures. Results are used to model concentration profiles within the electrolyte, and concentration polarization is expected to be much worse at cold temperatures. Chapter 4 evaluates two methods of modeling these concentration gradients, one involving transference numbers determined using electrochemical methods and one involving transference numbers using electrophoretic NMR. Concentration gradients are expected to be larger based on electrochemical methods, but potential gradients and current-voltage characteristics are remarkable similar between both methods. Chapter 5 studies the impact of solvent chain length on transport and thermodynamic properties for oligoether solvents. The cation transference number is the only transport property that doesn't decrease with increasing chain length, but rather exhibits a characteristic dependence on salt concentration across all electrolytes. Chapter 6 evaluates the impact of high salt concentration on transport properties. Higher salt concentration worsens ion transport, leading to increasing concentration and potential gradients with increasing salt concentration.

2 Complete Characterization of a Lithium Battery Electrolyte Using a Combination of Electrophoretic NMR and Electrochemical Methods

2.1 Abstract

Improving transport properties of the electrolyte is important for developing lithium-ion batteries for future energy storage applications. In Newman's concentrated solution theory, electrolytes are characterized by three transport parameters, conductivity, diffusion coefficient, and transference number, in addition to the thermodynamic factor. In this work, these parameters are all determined for an exemplar liquid electrolyte, lithium bis(trifluoromethanesulfonyl)imide mixed in tetraethylene glycol dimethyl ether, using electrochemical methods. The intrinsic coupling between parameters obtained by electrochemical methods results in large error bars in the transference number that obscure the transport behavior of the electrolyte. Here, we use electrophoretic NMR (eNMR) to measure the electric-field-induced ion and solvent velocities to obtain the transference number directly, which enables determination of the thermodynamic factor with greater certainty. Our work indicates that the combination of eNMR and electrochemical methods provides a robust approach for complete characterization of battery electrolytes.

2.2 Introduction

Over the last decade, the sale and use of electric vehicles (EVs) has dramatically increased due to the improvement in lithium-ion batteries. Batteries for electric vehicles still need to bolster reliability and range in order to appeal to the consumer, which requires improvement in battery technology related to safety, cost, discharge rates, and energy density.[35] The state-of-the-art lithium-ion battery includes a graphitic anode, a carbonate-based liquid electrolyte, and a transition-metal-oxide cathode. Modeling ion transport through the battery requires complete characterization of the electrolyte, which comprises a lithium salt dissolved in an organic solvent (or a mixture of organic solvents). In Newman's concentrated solution theory,[5] complete characterization implies knowledge of the thermodynamic factor and three transport parameters – conductivity, κ, salt diffusion coefficient, D, and the cation transference number with respect to the solvent velocity, t_+^0. Conductivity and salt diffusion coefficient are relatively easy to measure: κ is measured by ac impedance spectroscopy and D is measured by restricted diffusion. Data from each of these experiments can be used to determine κ and D directly. In contrast, the transference number is difficult to measure accurately because it typically requires combining three or four separate electrochemical experiments, depending on the particular approach used.[8,36–39] Similar difficulties apply to the thermodynamic factor.

The thermodynamic factor, T_f, is defined as[5]

$$T_f = 1 + \frac{d\ln\gamma_{+-}}{d\ln m}, \tag{2.1}$$

where γ_{+-} is the mean molal activity coefficient of the salt and m is the molality of the electrolyte. An experiment that is often used to determine the thermodynamic factor involves a concentration cell,[40] shown schematically in Figure 2.1. The cell comprises two compartments separated by a porous glass frit. Two solutions at different molalities, m and m_r, are placed in the two compartments, and the open circuit potential, U, is measured using lithium metal electrodes. Care

is taken to ensure that the measurements are made before significant diffusion occurs across the glass frit. For a univalent salt, the relationship between U and γ_{+-} is given by equation 2.2,[5]

$$FU = 2RT \int_{m_r}^{m} t_-^0 \left(1 + \frac{d\ln\gamma_{+-}}{d\ln m}\right) d\ln m. \tag{2.2}$$

Equation 2.2 may be used to determine the dependence of γ_{+-} on m, but this requires knowledge of the anion transference number, t_-^0, at all concentrations between m_r and m. This knowledge is traditionally obtained by additional electrochemical experiments as demonstrated first by Ma et al.[8] In this work, the additional experiment used was the current interrupt technique wherein a constant current density, i, is applied to a lithium-electrolyte-lithium symmetric cell for a short period of time, t, and the open circuit potential right after the current is interrupted, U_{ci}, is measured as a function of applied current density. The slope of a plot of U_{ci} versus $it^{1/2}$ is related to t_+^0. However, in addition to the transference number, this slope also depends on D and T_f. One therefore needs a third experiment to measure D. In the work of Ma et al., the restricted diffusion experiment was used to determine D. In related work, Pesko et al. used measurements of the current fraction, ρ_+, as the additional experiment for determining t_+^0.[36] ρ_+ is defined as the ratio of the steady-state current to the initial current measured in a lithium-electrolyte-lithium symmetric cell. The importance of ρ_+ was recognized in the pioneering works of Bruce and coworkers[41,42] and Watanabe and coworkers.[43] The uncertainty in the measured transference number using either electrochemical method discussed in this paragraph is large because of its dependence on multiple parameters with their own experimental error.[9]

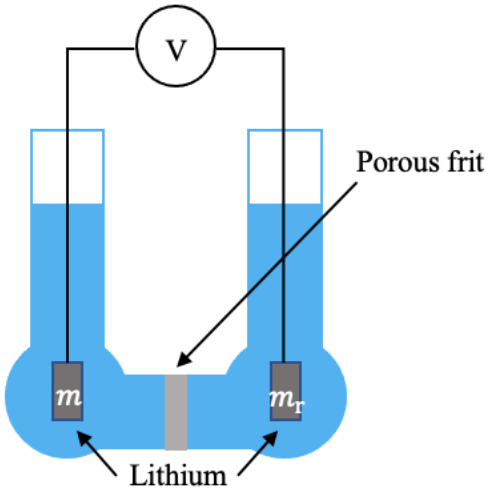

Figure 2.1. Schematic of a concentration cell.

One additional problem arises when lithium-electrolyte-lithium symmetric cells are used to obtain transport properties. Most liquid electrolytes react irreversibly with lithium metal, especially under applied electric fields, and this results in the formation of a variety of protrusions, such as dendrites, globules, and mossy and tree-like structures.[44,45] While the importance of these structures in the context of commercializing rechargeable batteries with lithium metal electrodes has received considerable attention, their relevance in the context of electrolyte characterization is

seldom discussed. The expressions used to analyze the data from symmetric cells to obtain t_+^0, D, U_{ci}, and ρ_+ are invalid if the lithium electrodes are nonplanar.

The objective of this paper is to present a new approach for complete characterization of liquid electrolytes. The electrolyte chosen for this study is a mixture of lithium bis(trifluoromethanesulfonyl)imide (LiTFSI) salt in tetraethylene glycol dimethyl ether (tetraglyme). Our work adds to the body of knowledge that already exists on ion transport in LiTFSI/tetraglyme mixtures.[24,33,46,47] The application of electrophoretic NMR (eNMR) to electrolytes is well established.[10–12] eNMR directly measures the velocities of the cation, v_+, anion, v_-, and the solvent, v_0, under an applied electric field. It has been shown[13] using concentrated solution theory that

$$t_+^0 = \frac{v_+ - v_0}{v_+ - v_-}. \tag{2.3}$$

The measured species' velocities in equation 2.3 are ensemble averages over all the different environments present in the electrolyte. This includes disassociated individual ions, charged clusters containing ions, charged solvent-ion clusters, and uncharged clusters like ion pairs. Since the average species' velocities can be measured with high precision, t_+^0 values obtained by this technique have small uncertainties. This in turn enables determination of the thermodynamic factor using concentration cells as shown in equation 2.2; the uncertainty in T_f thus obtained is also smaller than that obtained by combining three electrochemical experiments. We also present measurements of κ using blocking electrodes, D using restricted diffusion, and ρ_+ using symmetric cells. This enables comparison of measured values of T_f and t_+^0 determined by the eNMR/electrochemical combination and those determined solely by electrochemical methods. Although eNMR has previously been used to characterize many different liquid electrolytes,[12,47] it has not yet been combined with electrochemical methods to completely characterize ion transport.

In addition to performing electrochemical and eNMR experiments, we have quantified the nature of the lithium-tetraglyme interfaces in cycled symmetric cells using hard X-ray microtomography. X-ray tomography is a 3D, nondestructive imaging technique[48] that has been used to image a variety of electrochemical cells to study phenomena such as electrode expansion[49] and dendrite growth in cells containing both liquid[50,51] and polymer electrolytes.[52] The results of these experiments ensure the validity of expressions used to obtain transport parameters from data obtained in lithium-LiTFSI/tetraglyme-lithium symmetric cells.

2.3 Experimental

2.3.1 Electrolyte Preparation

Tetraethylene glycol dimethyl ether (tetraglyme) and lithium bis(trifluoromethanesulfonyl)imide (LiTFSI) salt were obtained from Sigma-Aldrich and dried under active vacuum in a glovebox antechamber for three days at 60°C and 100°C, respectively. All electrolytes were made in an argon glovebox, with water and oxygen levels kept below 1 ppm. Electrolytes were prepared by dissolving a known mass of LiTFSI salt in a given volume of tetraglyme and stirring overnight at 25°C. Concentrations of electrolyte varied between an r value of 0.008 and 0.112, where r is a measure of salt concentration corresponding to the ratio of lithium ions to ether oxygens in

tetraglyme, r = ([Li^+]/[O]). We also provide salt concentration in units of molality (moles of LiTFSI per kilogram of tetraglyme), m. The concentrations used in this study are summarized in Table S2.1.

2.3.2 Conductivity

Conductivity was measured using a Mettler Toledo InLab-751 conductivity probe with platinum blocking electrodes. Temperature was measured via the probe and maintained at 30°C ± 1°C during the measurement. The conductivity probe was calibrated using a 1413 μS/cm potassium chloride conductivity standard to determine the cell constant prior to measurement. Conductivity was also measured using ac impedance spectroscopy. Five layers of Celgard 2500 separators soaked in electrolyte were sandwiched between stainless steel shims (MTI Corp.) and assembled in CR2032 coin cell parts (MTI Corp). The Celgard separators were cut to 19 mm and have a thickness of 25 μm. The stainless steel shims had a diameter of 15.5 mm and a thickness of 0.2 mm. Cells were made in triplicate for each concentration and cycled in an environmental chamber to maintain a temperature of 30°C. Impedance measurements were taken using a Biologic VMP300 potentiostat, where impedance spectra were obtained for a frequency range of 100 mHz to 1 MHz with a voltage amplitude of 5 mV. Series resistance values, R_s, were obtained from the impedance spectra and related to the conductivity via:

$$\kappa = \frac{\tau}{\varphi_c}\frac{l}{R_s A}, \tag{2.4}$$

where τ is the separator tortuosity, φ_c is the volume fraction of the conducting phase, l is the thickness of the separator, and A is the surface area of the electrodes. For Celgard 2500, φ_c is taken as 0.55, the porosity according to the manufacturer. The utilization of two conductivity measurements enables the determination of τ for the Celgard separator:[53] τ = 2.93.

2.3.3 Current Fraction and Restricted Diffusion

Polarization experiments were performed on lithium-LiTFSI/tetraglyme-lithium symmetric cells assembled in coin cells. Layers of five or ten Celgard 2500 separators were soaked in electrolyte and stacked between 14 mm lithium chips with a thickness of 600 μm (MTI Corp). The cell stack was topped with a 15.5 mm stainless steel shim and a wave spring before crimping. At least three cells were made for each thickness and concentration. Cells were cycled inside an environmental chamber to maintain a temperature of 30°C, which was corroborated using a thermocouple.

To establish a stable solid electrolyte interphase (SEI) between lithium metal and the electrolyte, cells were preconditioned by positively polarizing the cell at 0.02 mA/cm^2 for four hours, letting the cell rest for one hour, and negatively polarizing the cell at 0.02 mA/cm^2 for four hours. Six conditioning cycles were performed to stabilize the interfacial resistance. After conditioning, the cell was polarized at ΔV = 10 mV, -10 mV, 20 mV, and -20 mV to make sure measurements were independent of applied potential. To obtain the current fraction, the steady-state current, I_{ss}, was measured for one hour and impedance measurements were taken every 20 minutes, including before and after polarization. The current fraction was then determined using equation 5.[7,41,42]

$$\rho_+ = \frac{I_{ss}}{I_\Omega}\left(\frac{\Delta V - I_\Omega R_{i,0}}{\Delta V - I_{ss}R_{i,ss}}\right). \quad (2.5)$$

$R_{i,0}$ and $R_{i,ss}$ are the interfacial resistance before polarization and after I_{ss}, the steady-state current, has been reached. I_Ω is the initial current in the cell, calculated by dividing the applied polarization, ΔV, by the summation of the initial bulk and interfacial resistances in the cell. This calculation is based on Ohm's law, assuming no concentration gradients exist at the first instant of polarization in the cell.

The diffusion coefficient was measured using restricted diffusion.[54] After polarization, the cell was allowed to relax for one hour and the open circuit potential (U) was measured every 0.5 seconds. The relaxation of the concentration gradient in the cell was measured via the relaxation of the potential. This was fitted to an exponential, $U(t) = k_0 + ae^{-bt}$, where k_0 is an offset voltage and a and b are fit parameters; $1/b$ is the characteristic decay time. The diffusion coefficient through the separator, D_s, was determined using the following equation, $D_s = \frac{l^2 b}{\pi^2}$. The relaxation potential is fit over a time window such that $\alpha = \frac{D_s t}{l^2} > 0.03$, which ensures the fit is independent of the shape of the steady-state concentration gradient formed during polarization.[55] For the five Celgard cells, D_s was obtained from the first 15 minutes of the relaxation profile. For the ten Celgard cells, D_s was obtained from the first 60 minutes of the relaxation profile. This is because increasing l by a factor of two results in a fourfold increase in characteristic decay time. The salt diffusion coefficient was calculated by correcting D_s for the tortuosity of the separator, so that $D = \tau D_s$.

2.3.4 Concentration Cells

The thermodynamic factor was determined using concentration cells[40] as described previously. Custom made glass U-cells were obtained from Adams and Chittenden. The U-cells contain a porous glass frit separating the two chambers to prevent rapid mixing, with an average pore size of 1.0-1.6 μm. One side of the U-cell was filled with a reference electrolyte (r = 0.064) and the other side filled with a test concentration. Each side was filled with equal volumes of electrolyte to equilibrate the heights in the two chambers and minimize pressure differences. Lithium electrodes were submerged into each side of the U-cell and U was measured for one hour for each test concentration to ensure the potential plateaued. Electrodes were connected so that a positive potential was measured when $m_r > m$. Measurements were taken at least twice for each concentration. Temperature was maintained at 30°C ± 1°C for the duration of the experiment.

2.3.5 Cell Design for X-ray tomography

Lithium-LiTFSI/tetraglyme-lithium symmetric cells were assembled in an airtight custom made cell holder made from polyether ethyl ketone (PEEK) as described by Ho et al.[56] The cell consisted of a 4 mm diameter lithium electrode, one 5 mm diameter Celgard 2500 separator soaked in electrolyte (r = 0.032), and another 4 mm diameter lithium electrode. Lithium electrodes had a thickness of 300 μm. A stainless steel spacer was placed on top of the stack to protect the lithium from deformation. The entire stack was topped with a spring and placed between stainless steel current collecting pins. Various cycling treatments were used to study the effect of current density, i, on lithium plating. One cell was uncycled to image the clean interface. Another cell underwent preconditioning only, five cycles of $i = \pm 0.01$ mA/cm^2 for four hours each. Tomographic imaging

was conducted in accordance with the work done by Maslyn et al[57] at Beamline 8.3.2 at the Advanced Light Source at Lawrence Berkeley National Laboratory.

2.3.6 Electrophoretic NMR

eNMR experiments were conducted in accordance with the method described by Halat et al.[58] The design and execution of eNMR experiments is discussed elsewhere.[10,59] ^{7}Li, ^{19}F, and ^{1}H NMR measurements were used to determine cation, anion, and solvent velocities, respectively. All experiments were conducted at 30°C.

2.4 Results and Discussion

X-ray tomography was used to study the electrode-electrolyte interfaces in lithium-LiTFSI/tetraglyme-lithium symmetric cells. A Celgard separator was used to construct the cells (see experimental section). In Figure 2.2a, we show a typical cross-sectional slice through an uncycled cell. Here we see two clean planar interfaces between the electrode and the electrolyte. In Figure 2.2b, we a show a typical tomographic slice through a preconditioned symmetric cell cycled at i = 0.01 mA/cm^2. This represents the typical polarization experiment for electrochemical characterization. The two clean interfaces seen in Figure 2.2b indicate that expressions for interpreting electrochemical data from symmetric cells with planar electrodes are valid. We note in passing that mossy lithium deposits can be seen in tomographic cross-sectional images obtained from cells cycled at i = 0.1 mA/cm^2; these images are not shown for brevity.

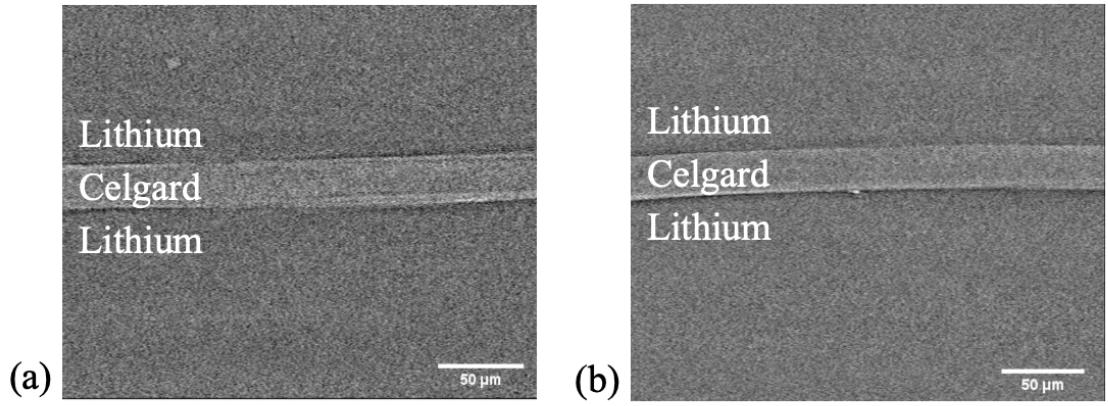

Figure 2.2. Typical tomographic slices of a lithium-LiTFSI/tetraglyme soaked Celgard separator-lithium symmetric cell. Comparison of an uncycled cell (a) and a preconditioned cell (b). No discernible mossy lithium is present when the cell undergoes low current cycling for short cycling times.

In Figure 2.3a, we plot conductivity, κ, as a function of both salt concentration, r, and molality, m, shown in the top x-axis. The figure shows conductivity values obtained using the conductivity probe and coin cells with blocking electrodes. Good agreement between the two methods is seen across the concentration range. Conductivity shows a nonmonotonic dependence on concentration, with an increase at low concentrations until a maximum is reached, and then a decrease across the rest of the concentration range. Conductivity increases at low concentrations due to the increase in the number of charge carriers. At higher salt concentrations, the increase in viscosity causes a decrease in the overall conductivity. In Figure 2.3b, we plot the current fraction, ρ_+, as a function of r and m. ρ_+ generally decreases with increasing r. The values of ρ_+ are small, usually below

0.20. The reproducibility of the measurement at r = 0.01 is low, presumably due to the low concentration of charge carriers. In Figure 2.3c, we plot the diffusion coefficient, D, as a function of r and m. Within experimental error, D is independent of r, taking on values between 2×10^{-7} to 7×10^{-7} cm^2/s. We have averaged data obtained from both five and ten Celgard cells; data from both kinds of cells were more-or-less consistent with each other; individual data sets obtained from the two types of Celgard cells are shown in Figure S2.7. The data in Figures 2.3c and S2.7 differ substantially from the measurements of Fawdon et al., who determined D from time resolved Raman microscopy.[60] Such discrepancies are often found in the literature.[37,61,62] Further work is needed to resolve such discrepancies. In Figure 2.3d, we plot U as a function of ln$m$. The variance of measured values of U is significantly smaller than that of the other parameters in Figure 2.3. U is a monotonic function of ln(m). The general characteristics of the U versus ln$m$ data in Figure 2.3d are similar to those published previously on mixtures of LiTFSI in poly(ethylene oxide).[36] This is not surprising because of the similarity in the chemical structures of tetraglyme and poly(ethylene oxide).

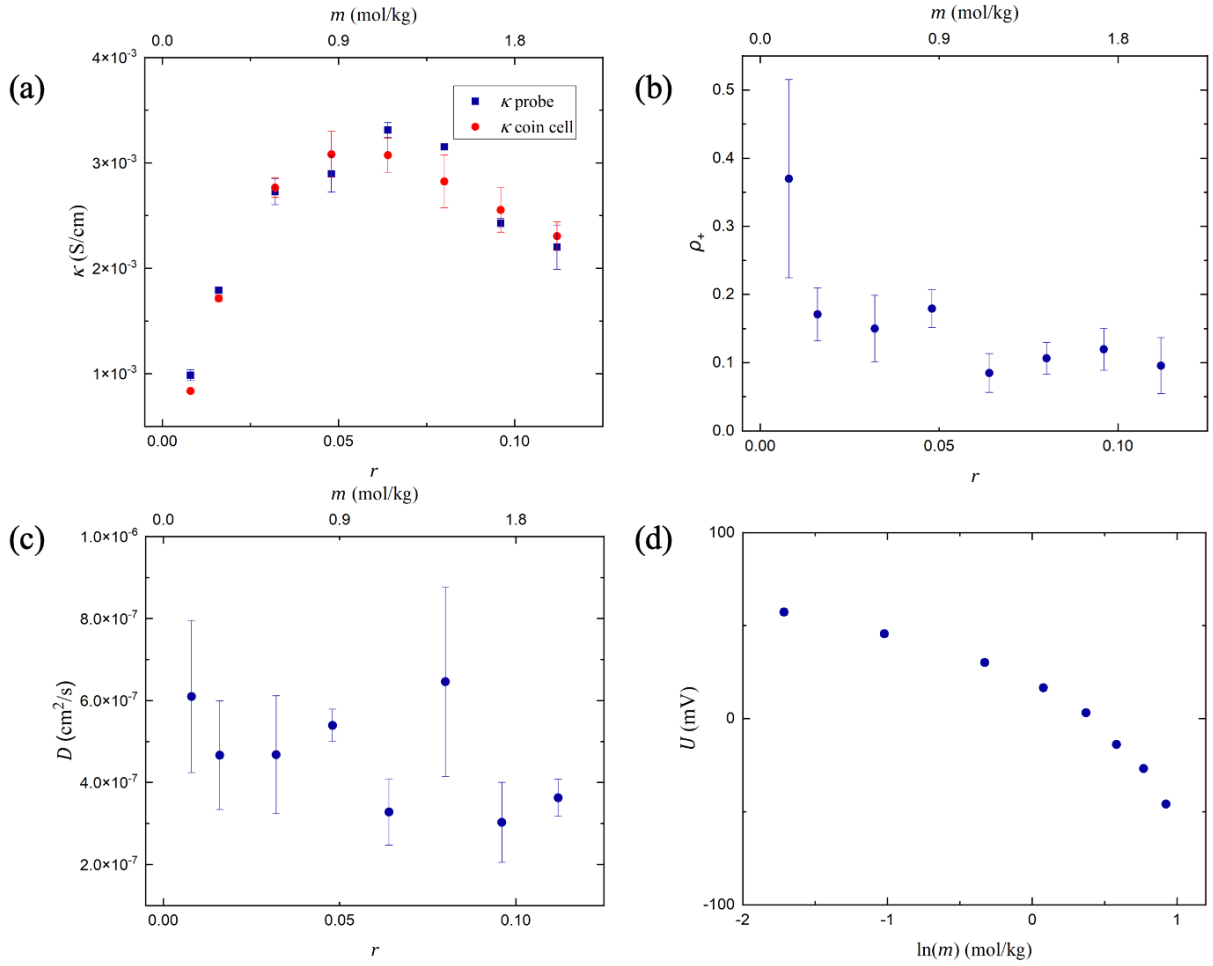

Figure 2.3. Electrochemical data for LiTFSI/tetraglyme. a) Conductivity, κ, as a function of r obtained using a conductivity probe and ac impedance spectroscopy; probe data was previously published by Halat et al.[58] b) Current fraction, ρ_+, as a function of r obtained using polarization experiments. c) Salt diffusion coefficient, D, as a function of r determined from restricted diffusion. d) Open circuit potential, U, as a function of log of molality obtained using concentration cells with a reference concentration of r = 0.064. All data was collected at 30°C.

For a univalent salt, the differential form of equation 2.2 is used to relate U, T_f, and t_+^0.[5]

$$T_f = -\frac{F}{2RT(1-t_+^0)}\frac{dU}{d\ln m} \tag{2.6}$$

The term $(1-t_+^0)$ can be expressed in terms of measured parameters κ, D, ρ_+, and U to give:[6,63]

$$T_f = \frac{\kappa}{2RTDc\left(\frac{1}{\rho_+}-1\right)}\left(\frac{dU}{d\ln m}\right)^2. \tag{2.7}$$

To calculate $\frac{dU}{d\ln m}$ at a given m, we use a finite difference approach. At all of the concentrations except the lowest and highest concentrations, $\frac{dU}{d\ln m}$ is taken to be the average of the finite difference slopes obtained on either side of that concentration. At the lowest and highest concentration, $\frac{dU}{d\ln m}$ is based on a single slope. This enables determination of T_f as a function of m. Finally, t_+^0 can be determined as a function of m using equation 2.8,[6,63]

$$t_+^0 = 1 - \sqrt{\frac{F^2Dc}{2\kappa RTT_f}\left(\frac{1}{\rho_+}-1\right)}. \tag{2.8}$$

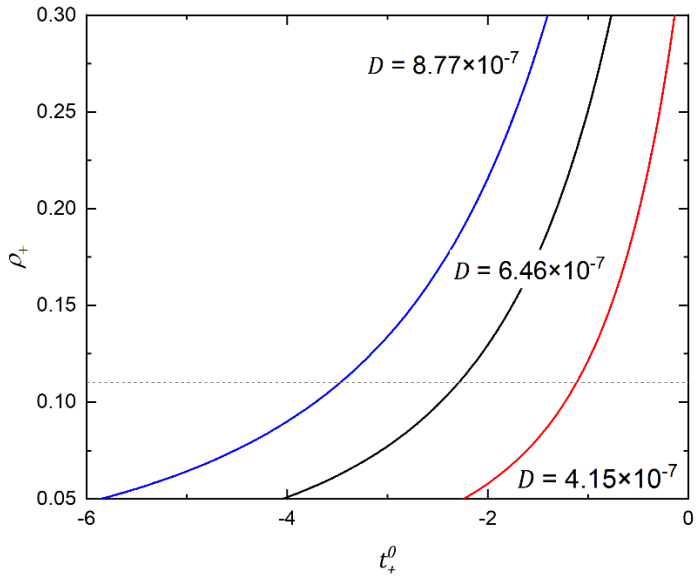

Figure 2.4. Dependence of the current fraction on the transference number for fixed transport parameters (r = 0.08, c = 0.00152 mol/cm^3, κ = 3.15×10^{-3} S/cm). Calculations are shown for three values of D, as indicated on the figure, and corresponding values of T_f. The dashed line at ρ_+ = 0.11 corresponds to the average value of the current fraction at this salt concentration.

Accurate determination of the transference number using multiple electrochemical experiments is difficult due to the compounding of errors. The transference number depends on three measured parameters, ρ_+, D, and κ, and one indirectly measured parameter, T_f (see equation 2.8). It is evident from Figure 2.3 that the variability in the measured values of ρ_+ and D is larger than that

of the measured values of κ and U. In Figure 2.4, we thus focus on how t_+^0 depends on ρ_+ and D.[64] For concreteness, we have used the measured parameters for r = 0.08 and the dependence of ρ_+ on t_+^0 for selected values of D is shown in Figure 2.4. These selected values cover the uncertainty in D reported in Figure 2.3c. At this value of r, the average value of ρ_+ is 0.11. However, individual experiments gave ρ_+ values as high as 0.15 and values as low as 0.07. It is evident from Figure 2.4 that the estimated value of t_+^0 is greatly influenced by the assumed value of D. A t_+^0 value of -1.1 is obtained using $D = 4.15\times10^{-7}$. In contrast, a t_+^0 value of -3.5 is obtained using $D = 8.77\times10^{-7}$. This uncertainty increases rapidly as ρ_+ decreases. It is important to note that uncertainties in ρ_+ and D are only two of the four sources of uncertainty in t_+^0. There is clearly a need to explore other avenues for determining t_+^0. It is widely accepted that values of t_+^0 in the vicinity of 0 or lower imply the presence of complex clusters involving multiple ions and solvent molecules.[65,66] Not only are these systems challenging to model, they are also difficult to study from the characterization point of view due to complex interactions between different species (cations, anions, and solvent) within the electrolyte.[5,8,33,43,47,58,66,67]

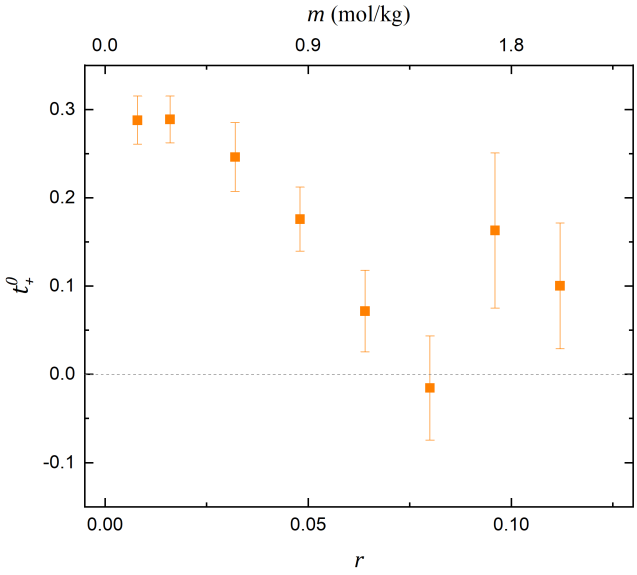

Figure 2.5. The transference number as a function of m and r determined from eNMR. This data was previously published by authors Halat et al.[58]

The transference number can also be measured directly using eNMR.[10–12] In this technique, velocities for the cation, anion, and solvent are directly measured and used to calculate the transference number according to equation 2.3. The dependence of t_+^0 on m determined by this method is shown in Figure 2.5.[58] The transference number has a nonmonotonic dependence on concentration; it decreases at low concentrations until a minimum close to 0 is reached at r = 0.08 and then increases again. t_+^0 value of 0 implies that under an applied electric field, the solvent and cation velocity are the same, suggesting strong complexation between all lithium ions and solvent molecules.[58] The increase of t_+^0 above r = 0.08 indicates the presence of more complex solvation structures and ion clustering.

In Figure 2.6a, we compare transference numbers determined by eNMR based on equation 2.3, referred to as $t_{+,eNMR}^0$, and electrochemical methods based on equation 2.8, referred to as $t_{+,echem}^0$.

The electrochemical data showed no evidence of a systematic dependence of t_+^0 on r. $t_{+,echem}^0$ reaches a minimum at r = 0.08. This is qualitatively similar to $t_{+,eNMR}^0$, which also shows a minimum at the same salt concentration. The absolute values of t_+^0 obtained by the two methods, however, are very different. Whereas t_+^0 from eNMR is positive over the salt concentration range, t_+^0 determined by electrochemical methods is almost exclusively negative. If our methods to estimate the uncertainty of t_+^0 by electrochemical methods were robust, we would expect the error bars corresponding to these values to include more accurately determined values of t_+^0 based on eNMR. We posit that our methods to estimate the uncertainty in our electrochemical characterization, which assumes that the errors in the four parameters needed to calculate t_+^0 are independent, are inadequate. Our results for ρ_+ and D are based on three replicates for each salt concentration and cell thickness, while our results for κ and $\frac{dU}{dlnm}$ are based on three and two replicates, respectively, measured in the same cell geometry. Perhaps increasing the number of samples by an order of magnitude would result in more robust estimates of error bars. It seems likely that our assumption regarding the independence of individual errors is too simplistic. Additional complications may arise in liquid electrolytes due to the need for a separator, convection effects, and instability of the electrode-tetraglyme interface.

Accurate determination of t_+^0 also leads to accurate determination of T_f. In Figure 2.6b, we plot the thermodynamic factor determined using equation 2.6 with t_+^0 determined by eNMR. Also included in this figure is the thermodynamic factor determined using equation 2.7, which relies on four electrochemical characterization experiments. The former is referred to as $T_{f,eNMR}$ and the latter $T_{f,echem}$. While there are discrepancies between $T_{f,eNMR}$ and $T_{f,echem}$, they are significantly smaller than those between $t_{+,eNMR}^0$ and $t_{+,echem}^0$. Both thermodynamic factors are assumed to be equal to unity at r = 0, as required by thermodynamics. They both decrease up to $r \cong 0.025$ and then increase over the rest of the concentration range. Measurements of T_f indicate that the electrolyte is non-ideal. The decrease of T_f to values below unity at low concentrations reflects Debye-Huckel interactions,[5,68] which dominate dilute electrolytes. The increase of T_f at higher concentrations reflects more complex ion-ion and ion-solvent interactions. Whereas measurement of $T_{f,echem}$ requires knowledge of four measured quantities (see equation 2.7), measurement of $T_{f,eNMR}$ only requires knowledge of two parameters determined from independent experiments: t_+^0 from eNMR and $\frac{dU}{d\ln m}$ from concentration cell experiments (see equation 2.6). Neither of these methods require stripping and plating of lithium metal, which eliminates any complications related to the reactive interface. While the dependence of $T_{f,echem}$ and $T_{f,eNMR}$ on salt concentration is similar, $T_{f,eNMR}$ is significantly larger that $T_{f,echem}$, especially at high salt concentrations. The diffusion coefficient, D, gives the flux of salt based on concentration gradients. This transport parameter is affected by both frictional and thermodynamic effects. We expect D to decrease with increasing r due to the increase in frictional effects. However, the significant increase in the thermodynamic factor with increasing r (Figure 2.6b) indicates that the gradient in chemical potential corresponding to the same concentration gradient increases with increasing r; this increase is larger when eNMR results are included in the analysis. The frictional and thermodynamic effects cancel out, resulting in a diffusion coefficient that is, at best, a weak function of r (Figure 2.3c).

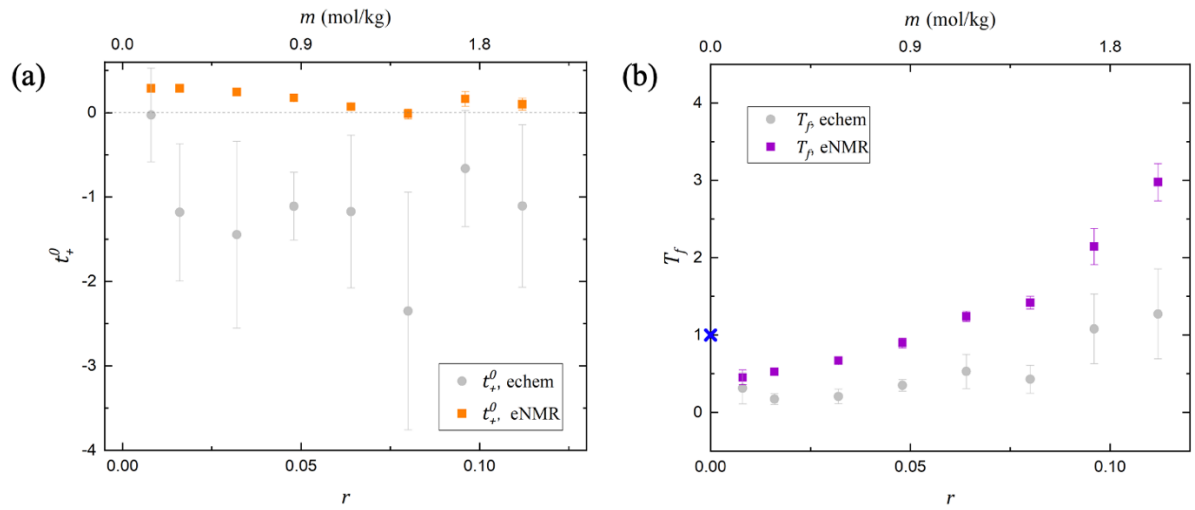

Figure 2.6. Comparison of electrochemical techniques and electrophoretic NMR for (a) transference number and (b) thermodynamic factor. The thermodynamic factor is unity at r = 0, shown in blue, based on the thermodynamic requirement that all solutions are ideal in the limit of infinite dilution.

2.5 Conclusion

In this work, we present complete electrochemical characterization of the bulk transport properties for an exemplar liquid electrolyte, LiTFSI salt dissolved in tetraglyme. Experiments included measurement of κ using ac impedance spectroscopy, D using restricted diffusion, ρ_+ using polarization experiments, and $\frac{dU}{d\ln m}$ using concentration cells. The results of these four experiments were combined to give estimates of t_+^0 and T_f. We also measured t_+^0 directly from eNMR measurements of ion and solvent velocities. The eNMR experiment requires specialized instrumentation while electrochemical characterization can be performed on commercially available potentiostats. We then used these measurements to determine T_f from concentration cell data. By combining eNMR and electrochemical techniques, we present complete electrochemical characterization of a liquid electrolyte with much smaller uncertainty in both t_+^0 and T_f.

2.6 Acknowledgments

This chapter is adapted from Hickson, D. T.; Halat, D. M.; Ho, A. S.; Reimer, J. A.; Balsara, N. P. Complete Characterization of a Lithium Battery Electrolyte Using a Combination of Electrophoretic NMR and Electrochemical Methods. *Phys. Chem. Chem. Phys.* **2022**, *24* (43), 26591–26599. https://doi.org/10.1039/D2CP02622H.

This work was primarily supported by the Assistant Secretary for Energy Efficiency and Renewable Energy, Vehicle Technologies Office, of the U.S. Department of Energy under Contract DE-AC02-05CH11231, under the Low Temperature Electrolyte program. D. M. H. and J. A. R. acknowledge the Joint Center for Energy Storage Research, an Energy Innovation Hub funded by the U.S. Department of Energy. A. S. H. was supported by a National Science Foundation Graduate Research Fellowship DGE-2020294884. Hard X-ray experiments were performed at the Advanced Light Source, which is supported by the Director, Office of Science, Office of Basic Energy Sciences, of the U.S. Department of Energy under Contract No. DE-AC02-

05CH11231. D. M. H performed and analyzed electrophoretic NMR experiments. A. S. H. performed x-ray tomography experiments. D. T. H. performed and analyzed electrochemical experiments. D. T. H. and N. P. B interpreted results and prepared the manuscript. N. P. B. and J. A. R. conceptualized and supervised the research. Helen Bergstrom is also gratefully acknowledged for helpful discussions and suggestions.

2.7 Supplemental Information

2.7.1 Salt Concentration Determination for LiTFSI/tetraglyme Electrolytes

Concentrations of the electrolytes used in this work are given in Table S2.1, showing the conversion between r, corresponding to the ratio of lithium ions to ether oxygens in tetraglyme (r = ([Li^+]/[O])) and molality, m, or moles of LiTFSI salt per kilogram of tetraglyme.

Table S2.1. Salt concentration equivalencies for LiTFSI/tetraglyme electrolytes

r ([Li^+]/[O])	m (mol/kg)
0.008	0.18
0.016	0.36
0.032	0.72
0.048	1.08
0.064	1.45
0.08	1.79
0.096	2.16
0.112	2.52

2.7.2 Diffusion Coefficient Fitting

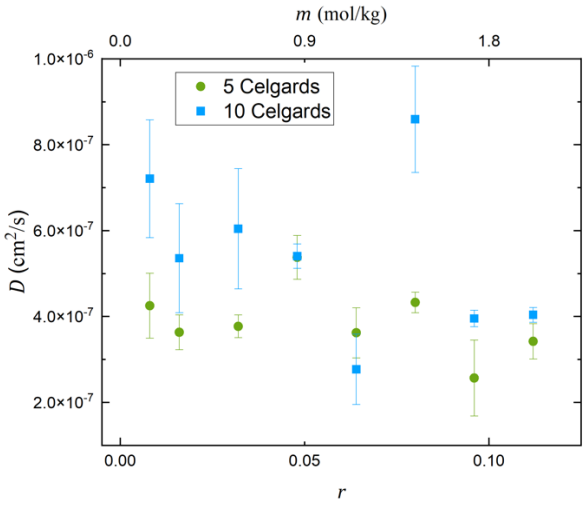

Figure S2.7. Comparison of averaged D from coin cells made with five and ten Celgards. For cells made with five Celgards, the first 15 minutes of relaxation were fit to determine D. For cells made with 10 Celgards, the first hour of relaxation was fit to determine D. Values are more-or-less consistent with each other.

2.7.3 Error determination

This section of the SI details equations used to determine error for all of the derived parameters in this work. Error formulas are based on standard error propagation. Error for measured parameters is based on standard deviation of multiple measurements.

Formula for determining error in $\frac{\mathrm{d}U}{\mathrm{dln}m}$ based on the finite difference method, where x_1 and y_1 refer to the ln(molality) and OCV, respectively, for the first data point:

$$\delta\left(\frac{y_3 - y_1}{x_3 - x_1}\right) = \left|\frac{y_3 - y_1}{x_3 - x_1}\right| * \left|\frac{\sqrt{(\delta y_3)^2 + (\delta y_1)^2}}{y_3 - y_1}\right| \tag{S2.1}$$

Error formula for thermodynamic factor based on electrochemical methods, $T_{f,\mathrm{echem}}$:

$$\delta\left(1 + \frac{dln\gamma_{\pm}}{dlnm}\right) = \left|1 + \frac{dln\gamma_{\pm}}{dlnm}\right| \sqrt{\left(\frac{\delta\kappa}{\kappa}\right)^2 + \left(\frac{\delta D}{D}\right)^2 + \left(\frac{\delta\rho_+}{\rho_+}\right)^2 + 2 * \left(\frac{\delta\left(\frac{dU}{dlnm}\right)}{\frac{dU}{dlnm}}\right)^2} \tag{S2.2}$$

Error formula for the transference number based on electrochemical methods, $t^0_{+,echem}$:

$$\delta t^0_+ = |t^0_-| \sqrt{\left(\frac{\delta\kappa}{\kappa}\right)^2 + \left(\frac{\delta D}{D}\right)^2 + \left(\frac{\delta\rho_+}{\rho_+}\right)^2 + \left(\frac{\delta\left(\frac{dU}{dlnm}\right)}{\frac{dU}{dlnm}}\right)^2} \tag{S2.3}$$

Error formula for calculation of the thermodynamic factor using eNMR and concentration cells, $T_{f,\mathrm{eNMR}}$:

$$\delta\left(1+\frac{dln\gamma_{\pm}}{dlnm}\right)=\left|1+\frac{dln\gamma_{\pm}}{dlnm}\right|\sqrt{\left(\frac{\delta t_{-}^{0}}{t_{-}^{0}}\right)^{2}+\left(\frac{\delta\left(\frac{dU}{dlnm}\right)}{\frac{dU}{dlnm}}\right)^{2}} \tag{S2.4}$$

2.8 Nomenclature

κ	Ionic conductivity (S cm^{-1})
D	Salt diffusion coefficient (cm^2 s^{-1})
t_+^0	Cation transference number with respect to the solvent velocity
T_f	Thermodynamic factor
γ_{+-}	Mean molar activity coefficient
m	Molality (mol kg^{-1})
U	Open circuit potential (mV)
F	Faraday's constant (C mol^{-1})
m_r	Reference molality (mol kg^{-1})
R	Universal gas constant (8.314 J mol^{-1} K^{-1})
T	Temperature (°C)
t_-^0	Anion transference number
i	Current density (mA cm^{-2})
t	Time (s)
U_{ci}	Open circuit potential from current interrupt technique (mV)
ρ_+	Current fraction
v_+	Cation velocity (μm cm^{-1})
v_-	Anion velocity (μm cm^{-1})
v_0	Solvent velocity (μm cm^{-1})
r	Measure of ratio of lithium ions to oxygen atoms in solvent
τ	Tortuosity of separator
φ_c	Volume fraction of conducting phase in separator
l	Thickness of the separator (cm)
R_s	Series resistance (Ω)
A	Area of electrodes (cm^2)
ΔV	Applied polarization potential (mV)
I_{ss}	Steady-state current (mA)
I_Ω	Initial current calculated via Ohm's law, $I_\Omega = \Delta V/R_T$ (mA)
$R_{i,0}$	Initial interfacial resistance (Ω)
$R_{i,ss}$	Steady-state interfacial resistance (Ω)
k_0	Offset voltage (mV)
a	Fit parameter for restricted diffusion
b	Fit parameter for restricted diffusion

3 Low Temperature Characterization of a Nonaqueous Liquid Electrolyte for Lithium Batteries

3.1 Abstract

Rechargeable batteries exhibit poor performance at low temperatures due to sluggish ion transport through the electrolytic phase. Ion transport is governed by three transport parameters – conductivity, diffusion coefficient, and the cation transference number with respect to the solvent velocity – and the thermodynamic factor. Understanding how these parameters change with temperature is necessary for designing improved electrolytes. In this work, we combine electrochemical techniques with electrophoretic NMR to determine the temperature dependence of these parameters for a liquid electrolyte, LiTFSI salt dissolved in tetraglyme between -20 and 45°C. At colder temperatures, all species in the electrolyte tend to move more slowly due to increasing viscosity, which translates to a monotonic decrease in conductivity and diffusion coefficient with decreasing temperature. Surprisingly, we find that the field-induced velocity of solvent molecules at a particular salt concentration is a nonmonotonic function of temperature. The cation transference number with respect to the solvent velocity thus exhibits a complex dependence on temperature and salt concentration. The measured thermodynamic and transport properties are used to predict concentration gradients that will form in a lithium-lithium symmetric cell under a constant applied potential as a function of temperature using concentrated solution theory. The calculated steady current at -20°C is lower than that at 45°C by roughly two orders of magnitude.

3.2 Introduction

Lithium ion batteries suffer from worsened performance when operated at low ambient temperatures, which is a major hindrance to the adoption of electric vehicles (EVs) in colder climates.[2–4] Slow transport within a battery causes decreased range and power for EVs in the winter and charging at cold temperatures increases the likelihood of plating and cell failure.[69] Previous studies have identified many issues with operation at low temperature, including increased charge transfer resistance,[70–72] slow desolvation,[73] increased resistance through the solid electrolyte interphase (SEI),[74] and slow transport through porous electrodes.[75] Sluggish transport through the bulk electrolyte at low temperatures is one of the central reasons why battery performance suffers.[76] A transport property that is relatively easy to measure is ionic conductivity, and the temperature dependence of this property has been reported in several prior studies.[62,77,78] Current lithium ion battery electrolytes comprise mixtures of solvents such as ethylene carbonate (EC), a high dielectric constant solvent with high viscosity, and dimethyl carbonate (DMC), a low dielectric constant solvent with low viscosity. Reduced conductivity at low temperatures has been correlated to increases in electrolyte viscosity for EC/DMC and other common carbonate based electrolytes.[77–79] Reducing the amount of EC has been investigated as an approach to lower the solvent viscosity and improve transport properties.[80–82] However, "EC-lean" electrolytes suffer from reduced conductivity and unstable electrode/electrolyte interfaces.[3,79,83] Generally, changing the solvent composition impacts the overall dielectric constant of the solvent and ion agglomeration,[79] which can impact the overall conductivity.[66,84,85] Engineering next generation electrolytes that will perform better over a wider temperature range is complex and must balance many material properties. Added complications arise due to the fact that ion transport in electrolytes depends on three additional properties that are seldom reported – salt diffusion

coefficient, transference number, and the thermodynamic factor. These properties are much more difficult to measure and, not surprisingly, knowledge of their temperature dependence is limited.

The cation transference number, t_+^0, quantifies the fraction of the current carried by the cation with respect to the solvent velocity in an electrolyte of uniform concentration. Determining t_+^0 based exclusively on electrochemical methods is complex and requires combining data from multiple experiments. Even studies at ambient temperatures have produced varying transference numbers for carbonate-based electrolytes, with each study utilizing a unique set of experiments with different levels of precision.[38,62,86–88] Comparison between transference numbers measured at ambient temperature has been reported elsewhere.[62,86] In the limited literature reporting transference numbers at multiple temperatures, conflicting trends have been reported. For a conventional, carbonate-based electrolyte, Ringsby et al. found that transference numbers were constant between 25 and -30°C using MD simulations.[79] This contrasted with experimental measurements of t_+^0 obtained for the same electrolyte by Landesfeind and Gasteiger, who found that t_+^0 decreased with decreasing temperature.[37] While there is no question that conductivity decreases with decreasing temperature, it is not clear if the same holds true for cation transference.

The experimental data described in the preceding paragraph are based on the quantification of cation transference based on electrochemical methods alone. In this approach, four independent experiments are used to determine the four relevant properties: conductivity, κ, salt diffusion coefficient, D, transference number, t_+^0, and a thermodynamic factor, T_f. The intrinsic coupling between t_+^0 and T_f in the measured quantities compounds error and reduces measurement certainty.

In this work, we have characterized a liquid electrolyte, lithium bis(trifluoromethanesulfonyl)imide (LiTFSI) salt dissolved in tetraethylene glycol dimethyl ether (tetraglyme). This simple binary liquid electrolyte has been widely studied,[24,33,47,89] but its transport and thermodynamic properties have not been fully characterized over a wide temperature range. We use electrophoretic NMR (eNMR) to determine t_+^0 directly by measuring the electric-field-induced cation, anion, and solvent velocities.[10–12] In addition, we also conduct the four electrochemical experiments indicated in the preceding paragraph. Combining these five experiments significantly reduces measurement uncertainty in t_+^0 and T_f. The electrochemical experiments were conducted over a wide temperature window from -20 to 45°C. Due to instrument limitations, the eNMR experiments could only be conducted from 15 to 45°C. In spite of this limitation, our measurements enable a comprehensive understanding of the many factors that underpin low ion transport rates at low temperatures in LiTFSI/tetraglyme mixtures. The four parameters, κ, D, ρ_+, and T_f, are necessary for predicting the response of our electrolyte to an applied current. We use our measurements of these parameters to predict the steady-state salt concentration profiles and current-potential relationships as a function of temperature in LiTFSI/tetraglyme mixtures.

3.3 Experimental

3.3.1 Electrolyte Preparation

Lithium bis(trifluoromethanesulfonyl) imide (LiTFSI) salt and tetraethylene glycol dimethyl ether (tetraglyme) were both acquired from Sigma-Aldrich and dried in a glovebox antechamber under active vacuum for three days at 60°C and 100°C, respectively. Electrolytes were prepared in an

argon glovebox, where oxygen and water levels were kept below 1 ppm and stirred overnight at 25°C. The concentrations of electrolytes used in this study are listed in Table S3.1. The unit of concentration r corresponds to the ratio of lithium cations in LiTFSI to ether oxygens in tetraglyme, r = ([Li^+]/[O]).

3.3.2 Material Characterization

Density of each electrolyte was determined using an Anton Paar DMA 4101 density meter for each salt concentration between 10 and 100°C. Density (ρ) data is fully reported in Table S3.2. Density data was used to calculate molarity of electrolytes at each temperature, which is reported in Table S3.3. Viscosity (η) data was collected using an electromagnetically spinning viscometer (Kyoto Electronics). Viscosity measurements were obtained for each salt concentration and temperature between 0 and 100°C and are presented in Figure 3.2b. The full set of viscosity data is listed in Table S3.4.

3.3.3 Conductivity

Coin cells were assembled using CR2032 coin cell parts (MTI Corp.) with five layers of Celgard 2500 separators soaked in electrolyte. Separators were sandwiched between two stainless steel blocking electrodes (MTI. Corp), 15.5 mm in diameter and 500 μm thick. At least three cells were made for each concentration, and cells were cycled in an environmental chamber (JEIO Tech) at a given temperature setpoint (45, 30, 15, 0, -20°C). Temperatures within the environmental chamber were corroborated using a thermocouple. Ac impedance spectroscopy measurements were obtained using a Biologic VMP300 potentiostat, using a frequency range of 1 MHz to 100 mHz with a sinus amplitude of 5 mV. Series resistance values, R_s, were obtained from the impedance spectra and can be related to the conductivity of an electrolyte via equation 3.1.[53]

$$\kappa = \frac{\tau}{\varphi_c}\frac{l}{R_s A}, \tag{3.1}$$

τ is the separator tortuosity, φ_c is the volume fraction of the conducting phase, l is the thickness of the separator, and A is the surface area of the electrodes. For Celgard 2500, φ_c is the porosity, 0.55. The tortuosity of the Celgard was previously determined and is 2.93.[89]

3.3.4 Current Fraction and Restricted Diffusion

Lithium-LiTFSI/tetraglyme-lithium symmetric cells were assembled in CR2032 coin cell parts (MTI Corp.) using five, ten, or fifteen layers of electrolyte soaked Celgard 2500 separators. Separators were sandwiched between lithium chips (MTI Corp.), 14 mm in diameter and 600 μm thick. A minimum of three cells were made for each concentration and thickness. Cells were cycled in an environmental chamber (JEIO Tech) to maintain a given temperature, which was corroborated using a thermocouple.

Cells were preconditioned to stabilize the SEI between the lithium metal electrodes and electrolyte. Alternating current densities of $\pm$0.02 mA/cm^2 were applied for four hours using a potentiostat (Biologic, VMP300) until the interfacial resistance, R_i, was stable. Cells were allowed to rest for one hour in between polarizations. To measure the current fraction, ρ_+, also sometimes referred to as the ideal transference number or the Bruce-Vincent transference number,[41–43] cells were polarized at ΔV = 10 mV, -10 mV, 20 mV, and -20 mV for one hour. Multiple potentials were used

to ensure the value of the current fraction was independent of applied potential. During polarization, the steady-state current, I_{ss}, was measured. Impedance measurements were taken before, during, and after polarization to determine $R_{i,0}$ and $R_{i,ss}$, the initial and steady-state interfacial resistances in the cell, respectively. I_Ω, the initial current in the cell, was determined using Ohm's law, assuming there are no concentration gradients within the cell at the start of polarization. The current fraction was calculated in accordance with equation 3.2.[41–43]

$$\rho_+ = \frac{I_{ss}}{I_\Omega}\left(\frac{\Delta V - I_\Omega R_{i,0}}{\Delta V - I_{ss}R_{i,ss}}\right). \tag{3.2}$$

After polarization, the cell was allowed to relax and the open circuit potential, U, was monitored. Cells were allowed to relax for either 15 minutes, 1 hour, or 2.25 hours, for the five, ten, and fifteen Celgard cells, respectively, as relaxation times scale with length squared. The relaxation of the potential corresponds to the relaxation of the concentration gradient using the method of restricted diffusion.[54] U was fitted to an exponential, $U(t) = k_0 + ae^{-bt}$, where k_0 is an offset voltage and a and b are determined from fitting. The diffusion coefficient through the separator, D_s, is related to the fit coefficient, b, via $D_s = \frac{l^2 b}{\pi^2}$. A minimum time cutoff is used such that $\alpha = \frac{D_s t}{l^2} > 0.03$, which ensures the fit is independent of the steady-state concentration gradient formed during polarization.[55] The salt diffusion coefficient, D, was calculated by correcting D_s for the tortuosity of the separator, so that $D = \tau D_s$.

3.3.5 Concentration Cells

Previously, the thermodynamic factor was determined using large volume concentration cells made from glass U-cells.[40,89] This method was effective for room temperature measurements of the open circuit potential, but did not allow for the precise control of temperature. In this work, pouch-based concentration cells were built following the procedure published by Landesfeind et al.[37] A 1 cm wide, 10 cm long, and 25 μm thick Celgard 2500 separator was placed in a pouch cell (5 cm wide, 13 cm long). The long separator ensures that complete mixing of the electrolyte via mutual diffusion will not occur during the measurement period.[37] The separator was placed on top of lithium foil electrodes (MTI Corp.), which were affixed to nickel tabs using sealing tape. One side of the separator was wet with a reference electrolyte, r = 0.064, and the other side was wet with a test electrolyte. Care was taken to ensure the separator was fully wet without having excess electrolyte spill into the cell volume. The pouch cell was then sealed under argon.

The pouch cells were then moved to an environmental chamber (JEIO tech) and placed between metal blocks to ensure temperature equilibration during the measurement, which was measured using a thermocouple. The open circuit potential for each concentration cell, U, was monitored at each temperature setpoint for 10 minutes and then the average value was taken. At least two pouch cells were made for each concentration.

3.3.6 Electrophoretic NMR

Details of electrophoretic NMR (eNMR) experiments have been previously reported.[58,90] Instrumentation was based on the work done by Fang et al.[91] Samples were prepared by filling a dried eNMR cell with electrolyte under an inert argon atmosphere. A convection-compensated double stimulated-echo (DSTE) PFG-NMR pulse program was used, with electric field pulses of

opposite polarity applied.[92–94] Applied voltages ranged between 10 and 50 V, and all velocities were normalized to 1 V/mm. The electric field was applied for a constant drift time, Δ, of 100 ms. The electric field was allowed to equilibrate between electric field pulses using recycle delays of 75 seconds. The electric field was calibrated at 25°C using a 10mM solution of tetramethylammonium bromide (TMABr) dissolved in D_2O (P & L Scientific, Stockholm, SE). eNMR phase shifts were manually analyzed by calculating phase shifts as previously described.[58] ^{7}Li, ^{19}F, and ^{1}H NMR measurements were used to determine cation, anion, and solvent velocities, respectively. Experiments were performed at a field strength of 9.4 T using a 400 MHz Bruker NEO spectrometer and a Bruker 5 mm water-cooled double resonance broadband diffusion (diffBB) probe, which was equipped with *z*-axis gradient capabilities (maximum gradient strength of 17 T m^{-1}) and a variable-temperature control. Experiments were conducted at 45, 30, and 15 °C, $\pm$ 1 °C. The temperature range for measuring velocities from eNMR was limited to a minimum temperature of 15°C as the species' velocities at this temperature were close to the instrumental measurement limits.

3.4 Results and Discussion

In Figure 3.1a, we plot conductivity, κ, shown as a function of temperature for all salt concentrations. Conductivity shows a nonmonotonic dependence on salt concentration at all temperatures, increasing in the low concentration regime due to an increase in charge carriers and decreasing in the high concentration regime due to frictional effects (Figure S3.17). At lower temperatures, conductivity markedly decreases: at -20°C, the electrolyte retains less than 12% of the 45°C conductivity at all salt concentrations. The conductivity decrease that occurs as temperature decreases has been well documented in literature.[3,79] A third order polynomial was fit through each temperature data set (Figure S3.17) in order to determine the conductivity peak at a given temperature. The salt concentration where the conductivity maximum occurs, r_{max}, is plotted in Figure 3.1b. κ_{max}, the value at which the conductivity peaks, is also shown. Both r_{max} and κ_{max} decrease as temperature decreases. The fact that κ_{max} decreases by a factor of 17 over the temperature range is not very surprising. What is more surprising is the reduction of r_{max} by a factor of two. The onset of frictional effects occurs at significantly lower concentrations when temperature is reduced. Consequently, decreasing temperature has a more deleterious effect on conductivity in concentrated electrolytes; compare the spread of the data in Figure 3.1a for low and high salt concentrations.

In Figure 3.2a, the molar conductivity (conductivity divided by salt concentration in mol/cm^3), Λ, is shown as a function of temperature (from -20 to 45°C). At the highest salt concentration, r = 0.112, Λ decreases by a factor of about 100, whereas at r = 0.008, the conductivity only decreases by a factor of about 10 over the same temperature range. In Figure 3.2b, we show the dependence of the viscosity, η, of our electrolyte on salt concentration and temperature (between 0 and 100°C). η decreases by about a factor of 42 at r = 0.112 and by a factor of 7 at r = 0.008 over the measured range of temperatures. From this data, we can also see that the viscosity of the most concentrated electrolyte also changes much more rapidly with temperature than the most dilute electrolyte.

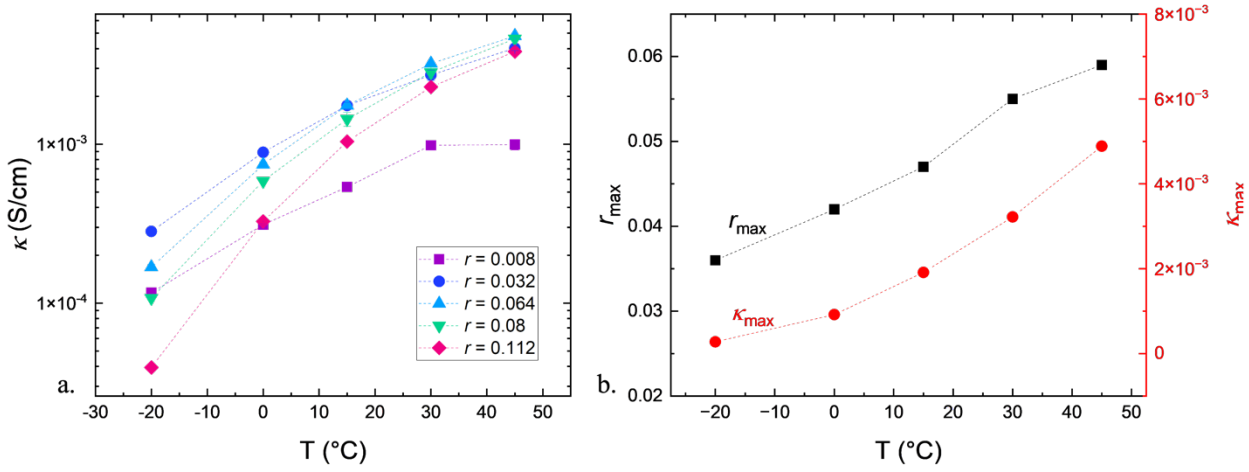

Figure 3.1. a) Conductivity data as a function of temperature for all salt concentrations, obtained using ac impedance spectroscopy. Error bars are smaller than the size of the data markers. b) Concentration at which conductivity peaks, r_{max}, plotted as a function of temperature. r_{max} was determined by fitting a third order polynomial to the measured conductivity data and determining the maximum. The corresponding conductivity at a given temperature, κ_{max}, is also plotted on the right y-axis.

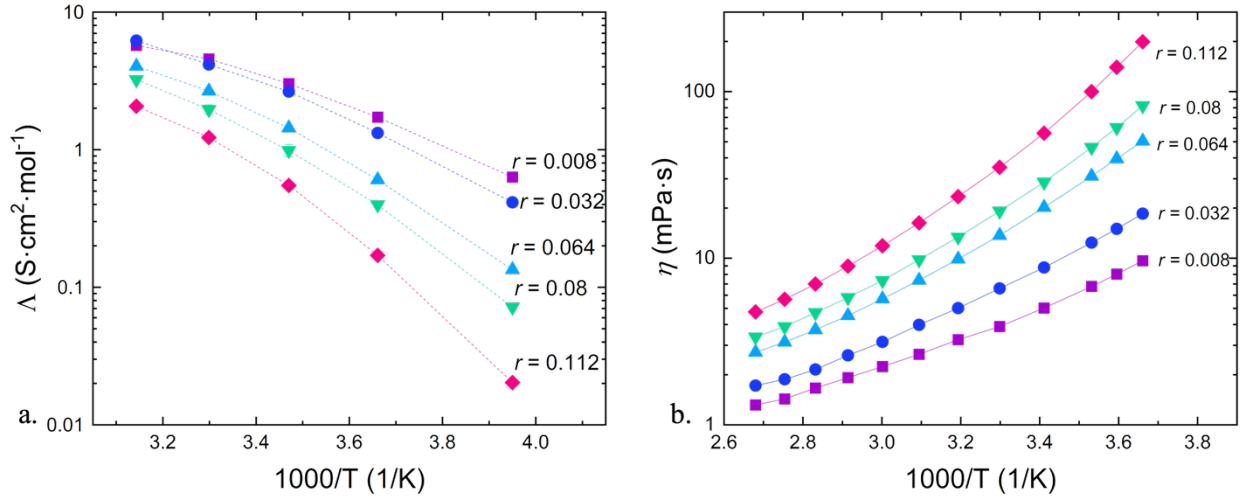

Figure 3.2. a) Molar conductivity is plotted as a function of inverse temperature. b) Viscosity data for corresponding salt concentrations is plotted as a function of inverse temperature. In both graphs, error bars are smaller than the size of the data markers.

The inverse relationship between conductivity and viscosity in liquid electrolytes is well established.[77,95,96] In the limit of infinite dilution, Walden observed that the product of the viscosity of pure water and molar conductivity was independent of temperature, also referred to as the Walden rule.[97,98] To examine this relationship in our system, we plot the product $\kappa\eta$ as a function of temperature in Figure 3.3. This product increases with increasing salt concentration but is a weak function of temperature at all salt concentrations. The dependence on temperature becomes

slightly stronger at higher salt concentrations. This indicates that the change in conductivity with temperature of LiTFSI/tetraglyme arises mainly due to changes in viscosity. Deviations from the Walden rule at higher concentrations are usually attributed to ion association.[99,100]

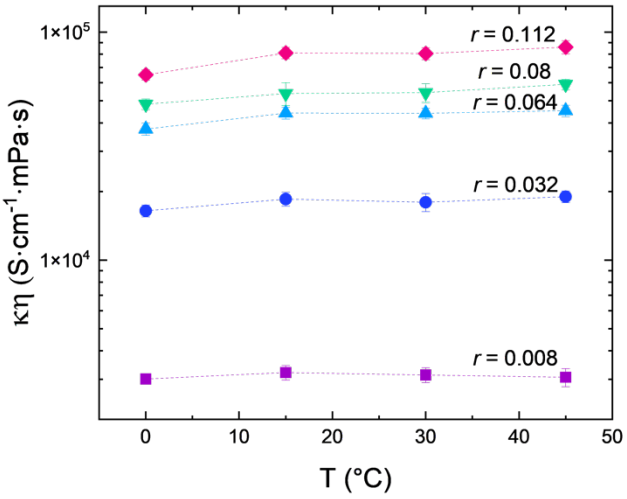

Figure 3.3. The product of conductivity multiplied by viscosity is shown as a function of temperature for all salt concentrations. In most cases, the error bars are smaller than the size of the data markers.

The decrease in conductivity with decreasing temperature is well established in the literature.[62,77,78] However, there are relatively few studies of the effect of temperature on other transport parameters. In Figure 3.4a, we show the dependence of current fraction, ρ_+, on salt concentration and temperature. Across all salt concentrations, ρ_+ decreases as temperature decreases. While κ is a more sensitive function of temperature at high salt concentrations, ρ_+ depends more strongly on temperature at low salt concentrations. In Figure 3.4b, we plot the product of $\kappa\rho_+$ as a function of temperature. In the limit of a small, applied dc potential, this product is proportional to the current that would be obtained in a given electrolyte.[7] The data obtained from different values of r seem to collapse when plotted in this format (see Figure 3.4b). This is a manifestation of the compensating dependencies of κ and ρ_+ on salt concentration mentioned above. In the concentration range, $0.064 < r < 0.112$, $\kappa\rho_+$ decreases by a factor of 200 ± 16 over our temperature window. This factor reduces systematically with decreasing concentration: at $r = 0.032$, this factor is 131, while at $r = 0.008$, this factor is 43.

The diffusion coefficient, D, measured using the restricted diffusion method,[54] is shown in Figure 3.5. At a given salt concentration, D is a weaker function of temperature when compared to κ. At r = 0.008, D decreases by a factor of 8 in our temperature window. This is somewhat lower than the decrease by a factor of 14 in κ. However, at $r = 0.112$, D only decreases by a factor of 4 while κ decreases by a factor of 100. Generally speaking, D deceases with increasing salt concentration. The surprising result in Figure 3.5 is D at -20°C is virtually independent of salt concentration (within experimental error). It is clear that D is not as strongly affected by solution viscosity as κ. The nonintuitive results in Figure 3.5 reflect the fact that D is affected by both thermodynamic and frictional contributions. We will attempt to separate these contributions in the discussion below.

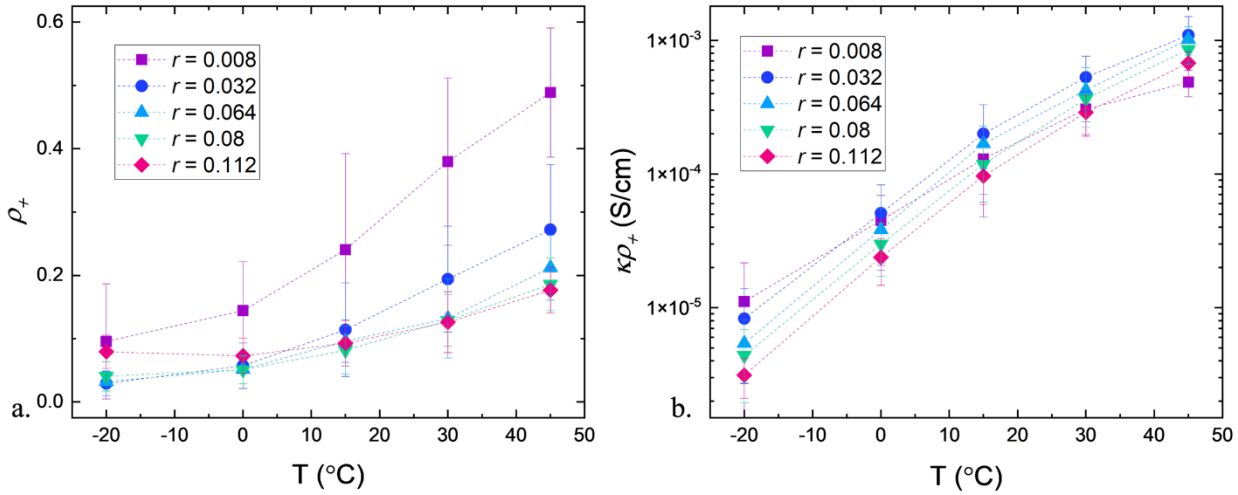

Figure 3.4. a) Current fraction and b) effective conductivity, both plotted as a function of temperature for all salt concentrations.

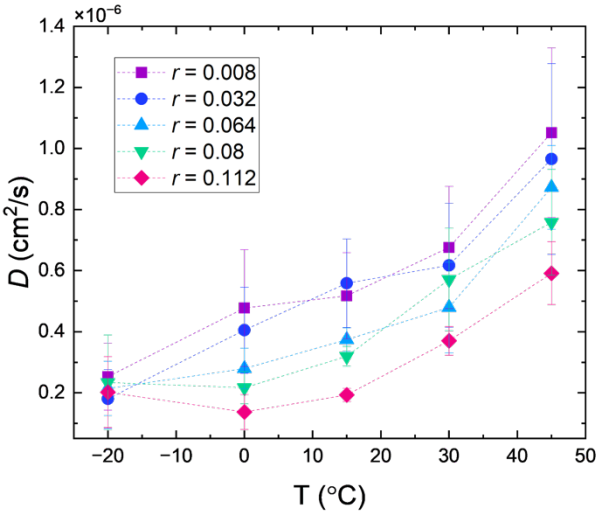

Figure 3.5. Diffusion coefficients obtained using restricted diffusion, plotted as a function of temperature for all salt concentrations.

Transference numbers, t_+^0, in the temperature range of 15 to 45°C were determined using electrophoretic NMR. The species' velocities were determined under an applied potential of 1 V/mm; v_+ is the cation velocity, v_0 is the solvent velocity, and v_- is the anion velocity. t_+^0 is given in equation 3.4.[13]

$$t_+^0 = \frac{v_+ - v_0}{v_+ - v_-}. \tag{3.4}$$

Measured values for v_+, v_0, and v_- using the laboratory reference frame are shown in Figure S3.13. Velocities of species in the direction of the negative electrode are defined as positive. For

all electrolytes, v_+ and v_0 are positive while v_- is negative. In general, the magnitude of all species' velocities decreases with decreasing temperature. The only exception to this is the solvent velocity for r = 0.08, which is a nonmonotonic function of temperature. The experimentally determined dependence of t_+^0 on r and temperature is shown in Figure 3.6. In the most dilute electrolyte, r = 0.008, t_+^0 is nearly independent of temperature. In the electrolyte with r = 0.032, t_+^0 decreases slightly with increasing temperature. More complex, nonmonotonic dependencies are seen in more concentrated electrolytes. The complex dependence of t_+^0 on temperature arises mainly due to the complex dependence of v_0 on salt concentration and temperature. The magnitude of v_+ relative to the overall ion velocities, $v_+ - v_-$, is not a strong function of temperature or salt concentration and varies between ~0.3 and 0.42 (see Figure S3.15). The lowest value of the t_+^0, -0.17, is obtained at r = 0.08 and T = 30°C. Under these conditions, the field-induced solvent velocity is larger than that of the cation.

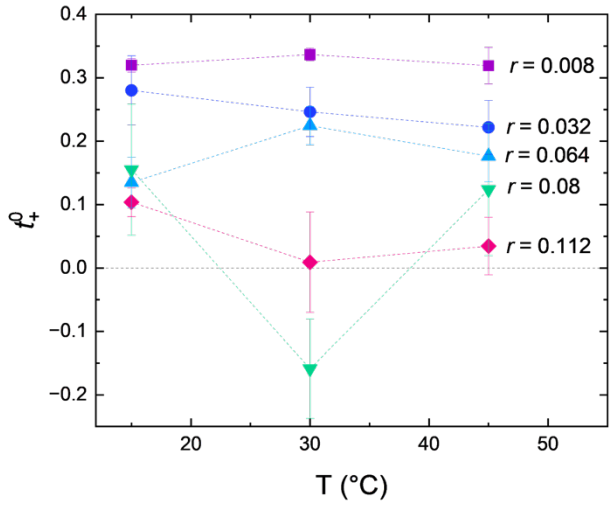

Figure 3.6. Cation transference number with respect to the solvent velocity, determined using electrophoretic NMR, plotted as a function of temperature for all salt concentrations.

The open circuit potential measured in a concentration cell, U, is plotted in Figure 3.7 as a function of ln(m) and temperature. The reference solution concentration was r = 0.064. U depends mostly on salt concentration and is a weak function of temperature. U is a more sensitive function of salt concentration at low temperatures. Our approach requires evaluation of dU/dln(m), which we obtain using a finite difference approach, described previously.[89]

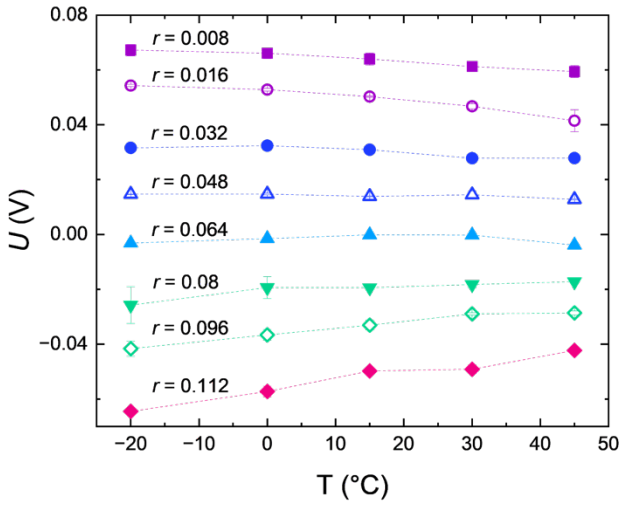

Figure 3.7. Open circuit potential determined in concentration cells, U, plotted as a function of temperature. Line labels refer to r for the test concentration. The reference concentration was r = 0.064. Error bars are smaller than the size of the data markers.

The thermodynamic factor, T_f, is given by:

$$T_f = 1 + \frac{dln\gamma_{+-}}{dlnm} = \frac{F}{2RT(1-t_+^0)}\frac{dU}{d\ln m}, \tag{3.5}$$

where γ_{+-} is the mean molal salt activity coefficient. Using t_+^0 values given in Figure 3.6 and $dU/d\ln(m)$ values determined from Figure 3.7, we obtain the dependence of T_f on concentration and temperature. Generally speaking, T_f increases with increasing salt concentration. A slight decrease of T_f is observed when salt concentration is increased from r = 0.064 to 0.08 at 30°C. This is mainly due to the nonmonotonic dependence of t_+^0 on temperature at r = 0.08. The complex dependence of t_+^0 on temperature arises mainly due to the complex dependence of v_0 on temperature at this salt concentration, as described above. At fixed temperatures, the thermodynamic factor, which reflects the non-ideality of our electrolyte, is a measure of the dependence of the salt activity coefficient on concentration. The increase in T_f with increasing salt concentration indicates that the non-ideality of the electrolyte is higher at higher concentrations. These non-idealities arise due to ion-ion and ion-solvent interactions. At r = 0.008, T_f is independent of temperature. This is the expected behavior or simple electrolytes, wherein the salt chemical potential, $\mu_{salt} = RTln(m\gamma_{+-}) + \mu_{salt}^0$, where μ_{salt}^0 is the chemical potential at a reference point.[5] At higher salt concentrations, more complex behavior is observed, indicating ion-ion and ion-solvent interactions are both temperature and concentration dependent.

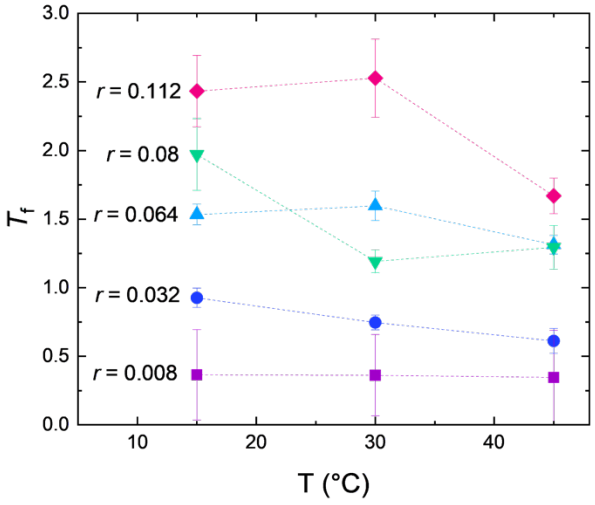

Figure 3.8. Thermodynamic factor, T_f, determined using transference numbers from eNMR and data from concentration cell experiments, plotted as a function of temperature for all salt concentrations.

The salt diffusion coefficient, D, is dependent on both frictional and thermodynamic effects, which results in a complex dependence on both salt concentration and temperature (Figure 3.5). One expects D to decrease with increasing viscosity, η, and therefore it is instructive to examine the product $D\eta$. This is analogous to the product $\kappa\eta$, plotted in Figure 3.3. The dependence of $D\eta$ on salt concentration and temperature is shown in Figure 3.9a. It is evident that the complex dependence of D on salt concentration and temperature is not just due to changes in viscosity. The product $D\eta$ is a stronger function of temperature in more concentrated electrolytes. The complexity in Figure 3.9a reflects the fact that D depends on both thermodynamics and frictional effects. One can define a Stefan-Maxwell diffusion coefficient, $\mathfrak{D}$, which quantifies diffusion based on a thermodynamic driving force,[5]

$$\mathfrak{D} = D\frac{c_0}{c_T T_f}, \tag{3.6}$$

where c_0 is the solvent concentration and c_T is the total concentration of the salt and solvent, $c_T = c_0 + c$. We use the measured values of D and T_f in equation 3.6 to determine $\mathfrak{D}$ as a function of concentration and temperature. The dependence of the product $\mathfrak{D}\eta$ on salt concentration and temperature is shown in Figure 3.9b. At the lowest concentration, r = 0.008, the differences between $D\eta$ and $\mathfrak{D}\eta$ are minor. The difference between $D\eta$ and $\mathfrak{D}\eta$ increases with increasing r. This implies that the corrections to D due to thermodynamic effects become more important as r increases. To a good approximation, the product $\mathfrak{D}\eta$ is equal to $(7\pm3)\times10^{-6}$ cm^2·mPa, irrespective of temperature and salt concentration. The product $\mathfrak{D}\eta$ is noteworthy as it is more-or-less independent of both temperature and salt concentration. Measurement of T_f enables the separation of these frictional and thermodynamic interactions.

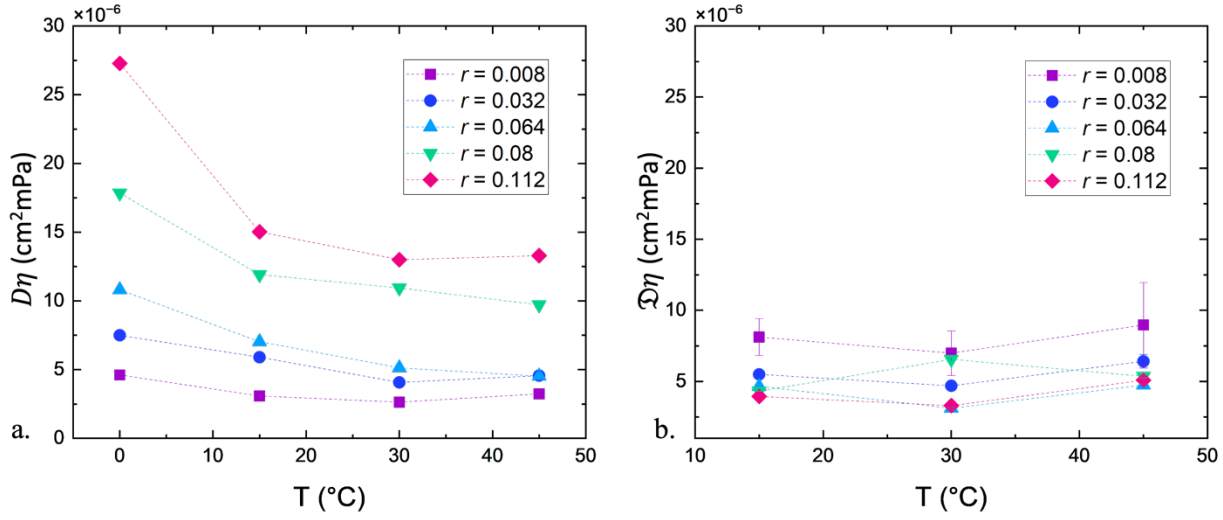

Figure 3.9. The product of diffusion coefficients and viscosity for a) the salt diffusion coefficient and b) Stefan-Maxwell diffusion coefficients, plotted as a function of both salt concentration and temperature. In some cases, error bars are smaller than the size of the data markers.

In concentrated solution theory, ρ_+ is given by $\rho_+ = 1/(1 + Ne)$,[63] where

$$Ne = a\frac{\kappa RT(t_-^0)^2}{F^2Dc}\left(1 + \frac{dln\gamma_{+-}}{dlnm}\right). \tag{3.7}$$

The parameter a is related to the stoichiometry of the salt via $\nu/(\nu_+z_+)^2$: a = 2 for a univalent electrolyte. The temperature dependence of ρ_+, shown in Figure 3.4a, reflects the temperature dependencies of κ, D, and t_+^0.

In the discussion above, we present complete characterization of LiTFSI/tetraglyme as a function of concentration and temperature. This enables predictions of concentration gradients that arise in the electrolyte due to the passage of current.[14,101,102] Large concentration gradients result in large concentration overpotentials which decrease the rate at which electrochemical reactions occur at the electrodes.[103–108] We calculate salt concentration and potential gradients as a function of applied current using concentrated solution theory in a symmetric lithium-LiTFSI/tetraglyme-lithium cell. The concentration profile is determined using equation 3.8,[14]

$$\int_{r(x=0)}^{r(x)} \kappa\left(\frac{dU}{dlnm}\right)\left[r\tau F\left(\frac{1}{\rho_+} - 1\right)\right]^{-1} dr = \frac{i_{ss}L}{Fz_-\nu_-}\left(\frac{x}{L}\right), \tag{3.8}$$

where i_{ss} is the steady-state applied current, L is the distance between electrodes, z_- is the anion charge number, and ν_- is the number of anions the salt dissolves into. x/L refers to the dimensionless position across the electrolyte. x/L = 0 is the positive electrode where salt accumulates. x/L = 1 is the negative electrode where salt is depleted. The potential of the positive electrode relative to that of the negative is given by Φ_{ss} in equation 3.9,[14]

$$\Phi_{ss}(x=0) = -Fz_{-}\nu_{-}\int_{r(x=L)}^{r(x=0)}\left(\frac{dU}{dlnm}\right)[rF\phi_c(1-\rho_+)]^{-1}dr. \tag{3.9}$$

In order to solve for $r\ (x=0)$ and $\Phi_{ss}\ (x=0)$, we need expressions that quantify the dependence of κ, $dU/dlnm$, and ρ_+ on temperature and concentration. These expressions were obtained by fitting the experimental data presented above and the fits are listed in Table S3.5. These fits are used to determine the concentration dependence of the integrands in equations 3.8 and 3.9. To facilitate calculations, the integrands were also fit to continuous functions that are given in Table S3.6 and S3.7.

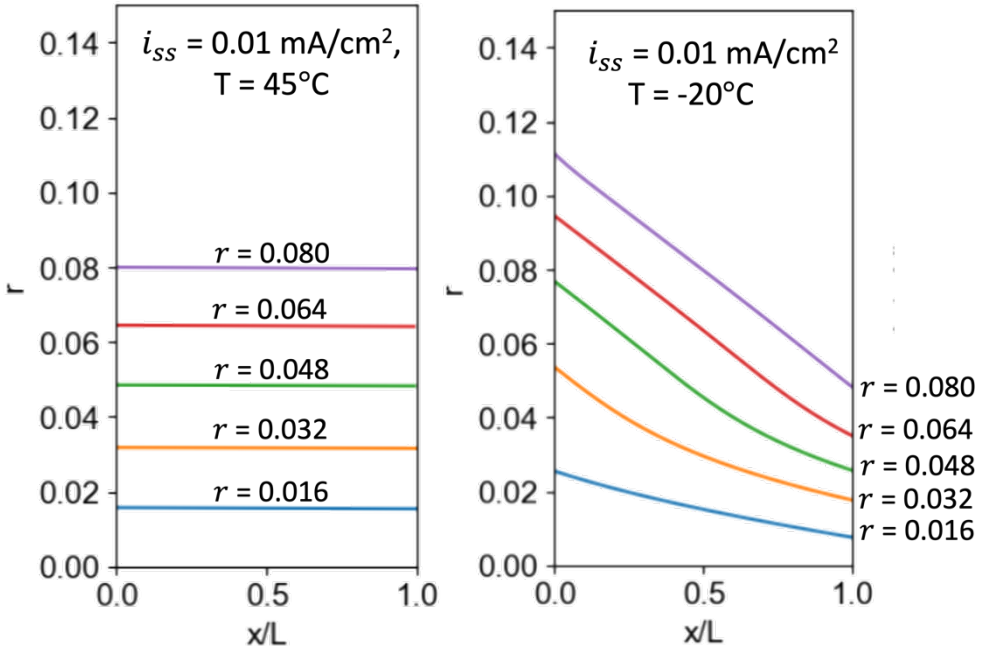

Figure 3.10. Results from modeled concentration gradients, based on measured electrochemical data. Predicted concentration gradients for multiple concentrations are shown for 45°C and -20°C for an applied steady-state current density of 0.01 mA/cm^2.

In Figure 3.10, we show results for a fixed applied steady-state current, i_{ss}, of 0.01 mA/cm^2. The average concentration of the electrolyte, r_{avg}, varied from 0.016 to 0.08. The results at 45°C are shown in Figure 3.10. At this temperature, the magnitudes of the salt concentration gradients are negligible. The results at -20°C are also shown in Figure 3.10. Here we see substantial salt concentration gradients and the magnitude increases with increasing salt concentration. In the limit of infinite dilution, wherein the electrolyte is thermodynamically ideal and transport parameters are independent of concentration, the salt concentration profile is linear.[5] It is thus not surprising that the profile at r_{avg} = 0.016 is approximately linear. Significantly, nonlinearity is seen when salt concentration is increased to r_{avg} = 0.032. Nonlinear contributions appear to decrease with increasing concentration and at r_{avg} = 0.08, the concentration profile is, to a good approximation, linear. The salt concentration profiles depend on three concentration dependent parameters, κ, $dU/dlnm$, and ρ_+, and these parameters can combine in nontrivial ways to give surprising results.

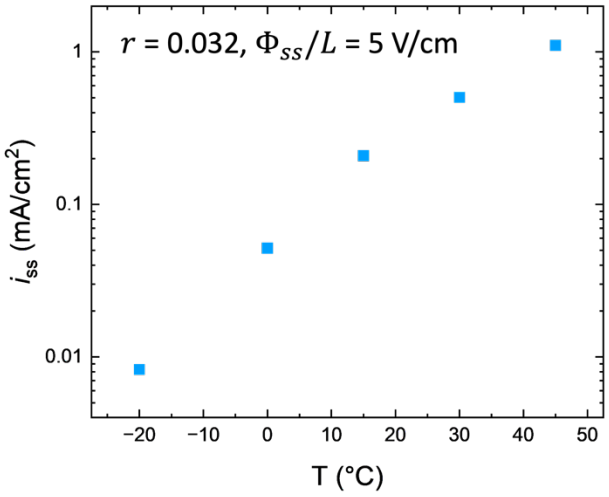

Figure 3.11. Results from modeled potential gradients, based on measured electrochemical data. For a given length normalized applied potential, here 5 V/cm, the resulting current at steady-state is shown for an example salt concentration, r = 0.032.

In Figure 3.11, we show results for a fixed applied length-normalized potential, Φ_{ss}/L, of 5 V/cm in an electrolyte with r_{avg} = 0.032. This polarization results in a steady-state current, i_{ss}, of 1.1 mA/cm^2 at 45°C. The current obtained drops precipitously with decreasing temperature and at -20°C, we obtain i_{ss} of 0.008 mA/cm^2. In other words, the current obtained decreases by a factor of 130 when temperature is changed from 45 to -20°C. We repeated these calculations for r_{avg} = 0.064 and 0.08. The factors by which current decreased over the same temperature range were 202 and 190, respectively. If the r_{avg} = 0.08 electrolyte was used in a rechargeable battery that was charged in one hour at 45°C, it would take 190 hours at -20°C.

3.5 Comparison to Literature

While LiTFSI/tetraglyme electrolytes have been studied previously,[24,33,47,89] we are not aware of prior studies that have characterized the LiTFSI/tetraglyme electrolyte over a wide temperature range. However, mixtures of $LiPF_6$ and carbonate solvents (e.g. ethylene carbonate, EC, ethyl methyl carbonate, EMC, and dimethyl carbonate, DMC) have been studied over a wide temperature range. We therefore compare our results with published data on these systems to examine which general trends hold true for liquid electrolytes. Across electrolyte systems, ions move slower at lower temperatures. This impacts ionic conductivity, which reflects field-induced motion of cations and anions, and the salt diffusion coefficient, which reflects the rate at which concentration gradients relax. Not surprisingly, a decrease in both conductivity (κ) and diffusion coefficients (D) with decreasing temperature has been found in all liquid electrolytes,[62,78,109] including LiTFSI/tetraglyme (Figures 3.1a and 3.5). However, D is affected by both frictional and thermodynamic effects, and we present data on Stefan-Maxwell diffusion coefficients, $\mathfrak{D}$, that is affected by frictional effects only (Figure 3.9). None of the previous experimental studies of temperature-dependent properties of liquid electrolytes have reported $\mathfrak{D}$.

There are conflicting reports on the effect of temperature on the cation transference number, t_+^0. Landesfeind and Gasteiger found t_+^0 to be a strong function of temperature in a 1 mol/L $LiPF_6$ in EC/EMC, decreasing from 0.35 at 25°C to -0.5 at -20°C.[37] Lundgren et al. also found that transference numbers decreased with decreasing temperature, but this depended on salt concentration. They found t_+^0 decreased from 0.27 at 40°C to 0.16 at 10°C for 0.5 mol/L $LiPF_6$ in EC/DEC, but it only decreased from 0.08 to 0.05 at 1.5 mol/L.[110] In contrast, simulations of Ringsby et al. suggest that t_+^0 is approximately 0.3 in 1 mol/L $LiPF_6$ in EC/EMC electrolytes between -20 and 30°C.[79] Temperature-independent transference numbers were also obtained using the Advanced Electrolyte Model, which predicted t_+^0 near 0.5 at both 60 and -30°C in the same electrolyte.[62,111] The reason for the discrepancy between theory and experiment in carbonate electrolytes remains unresolved. The results in carbonate electrolytes are very different from the t_+^0 data in tetraglyme (Figure 3.6). Much of the complexity seen in Figure 3.6 arises due to the field induced motion of solvent molecules (v_0, Figure S3.13).

Landesfeind and Gasteiger reported that the thermodynamic factor, T_f, is a weak function of temperature in EC/DMC and EC/EMC. They did, however, obtain a slight decrease in T_f with decreasing temperature. The data presented in this work for LiTFSI/tetraglyme electrolytes is also a weak function of temperature, although there is a slight increase in T_f with decreasing temperature (Figure 3.8).

Unlike κ and $\mathfrak{D}$, t_+^0 and T_f are affected by many factors that can change with temperature in unpredictable ways. For example, Ringsby et al. studied ion clustering in liquid electrolytes as a function of temperature using molecular dynamic simulations, and found that the concentration of free Li^+ ions was larger at -20°C compared to 30°C.[79] This was attributed to an increase in the solvent dielectric constant with decreasing temperature.[112] Since t_+^0 reflects the average field-induced-velocity of the cations (including free cations and clustered cations), the concentration of Li^+ ions will affect t_+^0. In spite of this, Ringsby et al. obtained a value of t_+^0 that was independent of temperature. Previous molecular dynamic studies have examined ion clustering and agglomeration at various salt concentrations for LiTFSI/tetraglyme electrolytes, which explains the complex dependence of t_+^0 on salt concentration.[22,58]

3.6 Conclusion

In this work, we combined electrochemical measurements with electrophoretic NMR to determine transport and thermodynamic properties of a liquid electrolyte, LiTFSI salt dissolved in tetraglyme. We have studied this electrolyte from -20°C to 45°C to determine how conductivity, diffusion coefficient, the cation transference number, and the thermodynamic factor change with temperature. Both conductivity and concentration-based salt diffusion coefficient decrease with decreasing temperature, but the magnitude of this decrease strongly depends on concentration. The product of viscosity and conductivity is nearly independent of temperature but a strong function of concentration. The product of viscosity and the Stefan-Maxwell diffusion coefficient, which is based on a thermodynamic driving force, is nearly independent of both concentration and temperature. The cation transference number with respect to the solvent velocity, t_+^0, reflects field-induced velocities of ions and solvent molecules. While the magnitude of velocities of the ions decreases monotonically with temperature, the solvent velocity exhibits a maximum at 30°C for

one salt concentration (r = 0.08). t_+^0 thus exhibits a complex dependence on concentration and temperature. In contrast, the thermodynamic factor is a weak function of temperature.

We have used concentrated solution theory and the transport and thermodynamic properties described in the preceding paragraph to predict concentration gradients that will form in a lithium-lithium symmetric cell under a constant applied potential as a function of temperature. The steady current obtained in these cells decrease as the magnitude of the concentration gradients increase. The steady current at -20°C is lower than that at 45°C by factors ranging from 130 to 202. The power available in batteries with LiTFSI/tetraglyme electrolytes would be drastically lower at -20°C relative to 45°C due, primarily, to the temperature dependence of transport properties.

3.7 Acknowledgments

This chapter was adapted from Hickson, D. T.; Im, J.; Halat, D. M.; Karvat, A.; Reimer, J. A.; Balsara, N. P. Low-Temperature Characterization of a Nonaqueous Liquid Electrolyte for Lithium Batteries. *J. Electrochem. Soc.* **2024**, *171* (3), 030514. https://doi.org/10.1149/1945-7111/ad2d91.

This work was primarily supported by the Vehicle Technologies Office of the U.S. Department of Energy's Office of Energy Efficiency and Renewable Energy under the guidance of the Advanced Battery Cell Research Program (eXtreme fast charge Cell Evaluation of Lithium-ion batteries, XCEL). Initial work was supported by the Assistant Secretary for Energy Efficiency and Renewable Energy, Vehicle Technologies Office, of the U.S. Department of Energy under Contract DE-AC02-05CH11231, under the Low Temperature Electrolyte program. We thank Dr Hasan Celik and UC Berkeley's NMR facility in the College of Chemistry (CoC-NMR) for spectroscopic assistance. The NMR instrument used in this work was supported by the National Science Foundation under grant no. 2018784. D.M.H. gratefully acknowledges support as a Pines Magnetic Resonance Center Postdoctoral Fellow; J.I. also acknowledges support from the Pines Magnetic Resonance Center. D.T.H and A.K. performed electrochemical experiments. J.I. performed electrophoretic NMR experiments. D.T.H. analyzed electrochemical results. J.I. and D.M.H. analyzed electrophoretic NMR experiments. D.T.H. and N.P.B interpreted results, prepared the manuscript, and conceptualized the research. N.P.B. and J.A.R. supervised the research.

3.8 Supplemental Information

3.8.1 Concentrations for LiTFSI/tetraglyme Electrolytes

Concentrations of the electrolytes used in this work are given in Table S3.1, showing the conversion between r, corresponding to the ratio of lithium ions to ether oxygens in tetraglyme (r = ([Li^+]/[O])) and molality, m, or moles of LiTFSI salt per kilogram of tetraglyme.

Table S3.1. Salt concentration equivalencies for LiTFSI/tetraglyme electrolytes

r ([Li^+]/[O])	m (mol/kg)
0.008	0.18
0.016	0.36

0.032	0.72
0.048	1.08
0.064	1.45
0.08	1.79
0.096	2.16
0.112	2.52

3.8.2 Density measurements of LiTFSI/tetraglyme electrolytes

Density was determined using an Anton Paar DMA 4101 density meter from 10 to 100°C for each electrolyte. Densities are reported in Table S3.2.

Table S3.2. Measured densities for LiTFSI/tetraglyme electrolytes, reported in g/cm^3.

r ([Li^+]/[O])	10°C	20°C	30°C	40°C	50°C	60°C	70°C	80°C	90°C	100°C
0.008	1.053	1.048	1.030	1.020	1.011	1.002	0.993	0.984	0.974	0.965
0.032	1.118	1.108	1.099	1.090	1.081	1.071	1.062	1.062	1.043	1.034
0.064	1.202	1.192	1.182	1.173	1.164	1.154	1.145	1.135	1.126	1.116
0.08	1.236	1.227	1.217	1.208	1.198	1.189	1.179	1.170	1.160	1.151
0.112	1.301	1.291	1.281	1.271	1.261	1.251	1.241	1.232	1.222	1.213

3.8.3 Molarity (M) of LiTFSI/tetraglyme electrolytes

Molarity was determined for each electrolyte concentration at each temperature using measured densities. Density changes predictably with temperature, so linear fits of density's dependence on temperature were fit to interpolate densities at 15 and 45°C and to extrapolate densities outside of the available temperature range to -20°C. Molarity is reported in Table S3.3.

Table S3.3. Molarity of LiTFSI/tetraglyme electrolytes, reported in mol/L.

r ([Li^+]/[O])	-20°C	0°C	15°C	30°C	45°C
0.008	0.184	0.181	0.178	0.176	0.174

0.032	0.683	0.672	0.664	0.656	0.647
0.064	1.253	1.233	1.219	1.204	1.190
0.08	1.500	1.478	1.461	1.444	1.427
0.112	1.943	1.915	1.893	1.872	1.851

3.8.4 Viscosity measurements of LiTFSI/tetraglyme electrolytes

Viscosities were determined using a Cannon Instrument Viscometer for each electrolyte from 0 to 100 °C. Viscosities are reported in Table S3.4.

Table S3.4. Measured viscosities for LiTFSI/tetraglyme electrolytes, reported in mPa·s.

r	0°C	5°C	10°C	20°C	30°C	40°C	50°C	60°C	70°C	80°C	90°C	100°C
0.008	9.66	8.02	6.77	5.02	3.89	3.24	2.65	2.24	1.92	1.66	1.43	1.32
0.032	18.5	15.0	12.4	8.80	6.58	5.02	3.98	3.15	2.61	2.61	1.88	1.72
0.064	50.4	39.5	31.1	20.2	13.7	9.88	7.38	5.70	4.52	4.52	3.13	2.73
0.08	82.3	60.9	46.3	28.6	19.2	13.4	9.79	7.35	5.80	5.80	3.89	3.37
0.112	199	140.	100.	56.2	35.1	24.3	16.3	11.9	8.96	8.96	5.67	4.76

3.8.5 Bulk resistance and interfacial resistance for lithium-lithium symmetric cells

Both the bulk and interfacial resistance, measured via ac impedance spectroscopy, are temperature dependent and concentration dependent. The dependence of both resistances has a nonmonotonic dependence on salt concentration and monotonically increases with decreasing temperature, as shown in Figure S3.12. The bulk resistance varies with the length between electrodes, and therefore is length normalized to the thinnest cell, with a separator thickness of 125 um. The interfacial resistance increases much more with decreasing temperature than the bulk resistance does, so that the ratio of the interfacial resistance to bulk resistance increases strongly with decreasing temperature. At 45°C, the interfacial resistance is ~2-3 times larger than the bulk resistance, but at -20°C, the interfacial resistance is ~20-100 times larger than the bulk resistance.

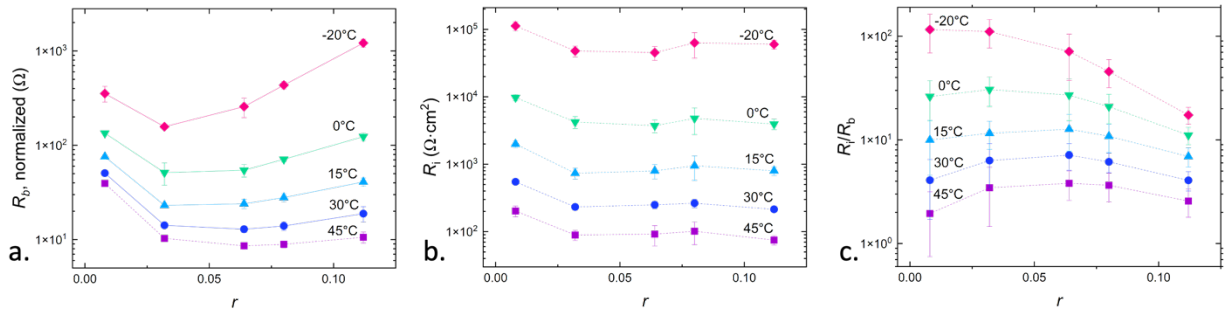

Figure S3.12. Resistances measured for lithium-lithium symmetric cells using ac impedance spectroscopy, shown as a function of salt concentration for each temperature. a) Bulk resistance of the electrolyte, corresponding to the conductivity of the electrolyte. b) The interfacial resistance of each lithium-lithium symmetric cell, normalized to the area of the electrodes. c) The average ratio of interfacial resistance to bulk resistance in lithium-lithium symmetric cells.

3.8.6 Cation, anion, and solvent velocities from eNMR

Species' velocities, measured using eNMR, are reported in Figure S3.13 for the cation, anion, and solvent as a function of salt concentration and temperature.

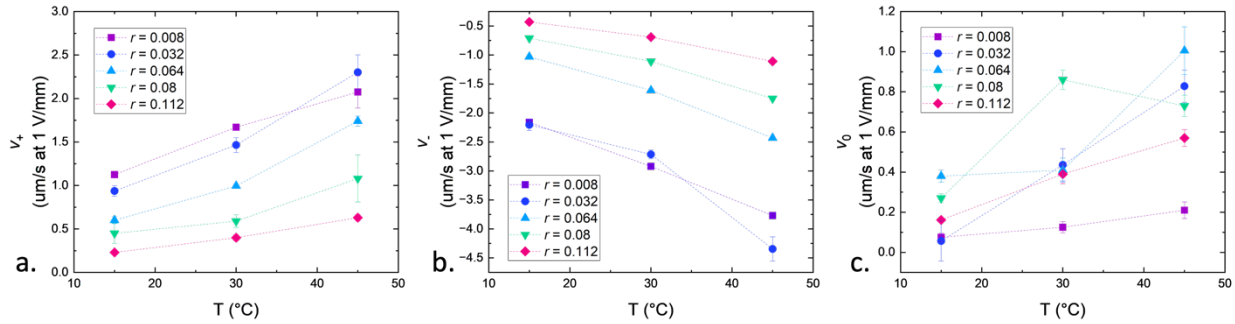

Figure S3.13. Velocities measured using eNMR. a) Cation velocity, b) anion velocity, and c) solvent velocity. All velocities are shown as a function of temperature for each salt concentration.

3.8.7 Conductivity comparison between eNMR and ac impedance spectroscopy.

To validate the eNMR measurements, conductivities determined from eNMR have been calculated according to S3.1. This is compared to conductivities measured using ac impedance spectroscopy, which was also recorded in Figure 3.1a. These two measurements for conductivity are compared in Figure S3.14.

$$\kappa = \frac{Fc(v_- - v_+)}{\nabla\phi} \tag{S3.1}$$

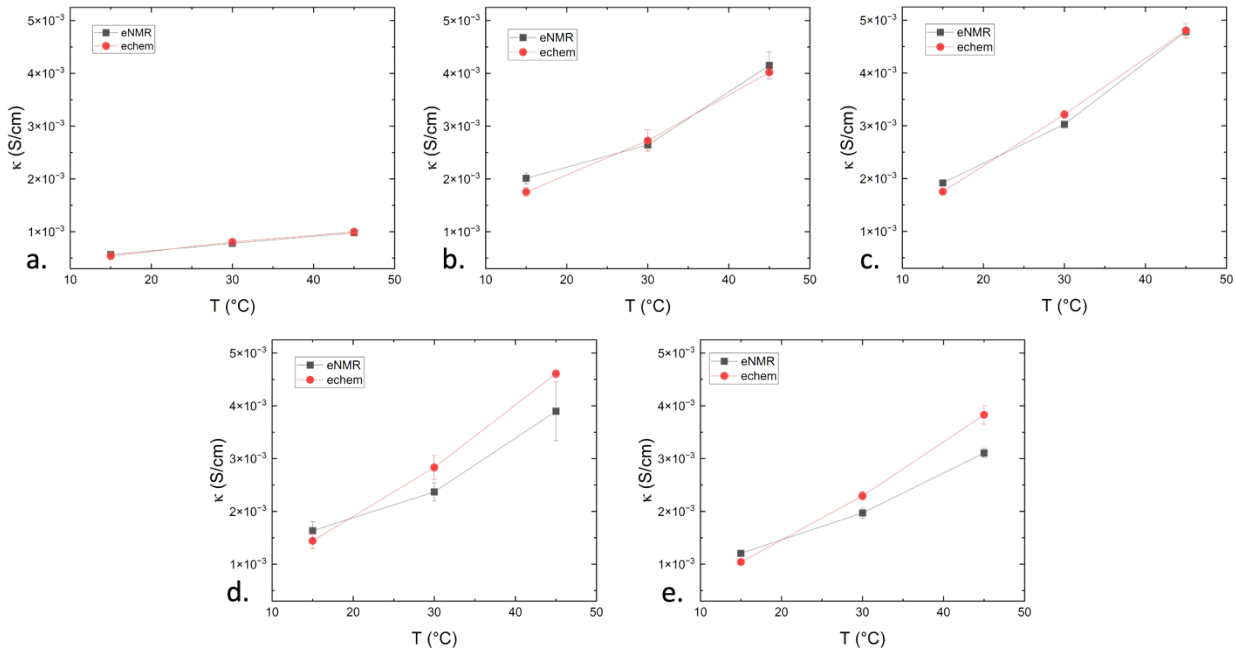

Figure S3.14. Conductivity comparison for each salt concentration, measured using both eNMR and ac impedance spectroscopy ('echem'). a) r = 0.008, b) r = 0.032, c) r = 0.064, d) r = 0.08, e) r = 0.112.

3.8.8 Cation transference numbers with respect to the lab reference frame, determined via eNMR velocities

Cation transference numbers with respect to the lab reference frame were determined using equation S3.2.

$$t_+^{lab} = \frac{v_+}{v_+ - v_-} \tag{S3.2}$$

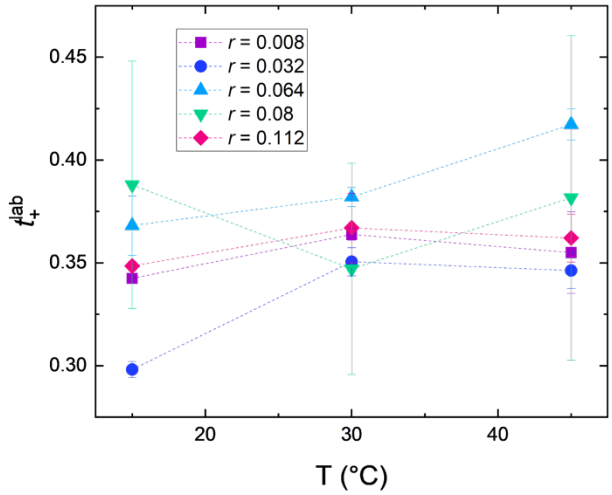

Figure S3.15. Cation transference numbers from eNMR with respect to the lab frame of reference, determined using equation S3.2.

3.8.9 Relationship between cation transference numbers and the current fraction.

If an electrolyte is ideal, the current fraction should accurately represent the transference number. Deviations from ideality cause a discrepancy between the measured current fraction and transference number. In Figure S3.16, t_+^0 is plotted against ρ_+. Values would follow the dotted line, $y = x$, if the electrolyte was ideal.

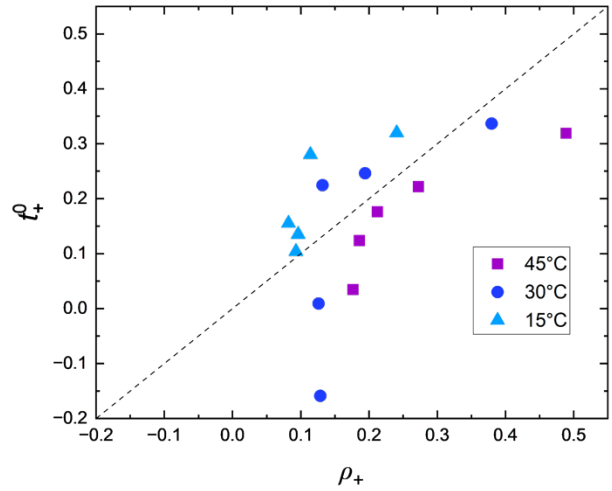

Figure S3.16. Cation transference numbers with respect to the solvent velocity, determined from eNMR, plotted against measured values of the current fraction at 15, 30 and 45°C.

3.8.10 Transport and Thermodynamic Properties as a function of Salt Concentration

The main text of this paper focuses on the impact of temperature on transport and thermodynamic properties for an exemplary liquid electrolyte. This electrolyte was also studied at various salt

concentrations, which has led to a complex and multidimensional data set. To help illustrate the dependence of various transport and thermodynamic properties on salt concentration, we have included graphs showing these properties as a function of r at fixed temperatures. The data plotted in Figures S3.17-S3.22 represents the same data as what has been shown in the main text.

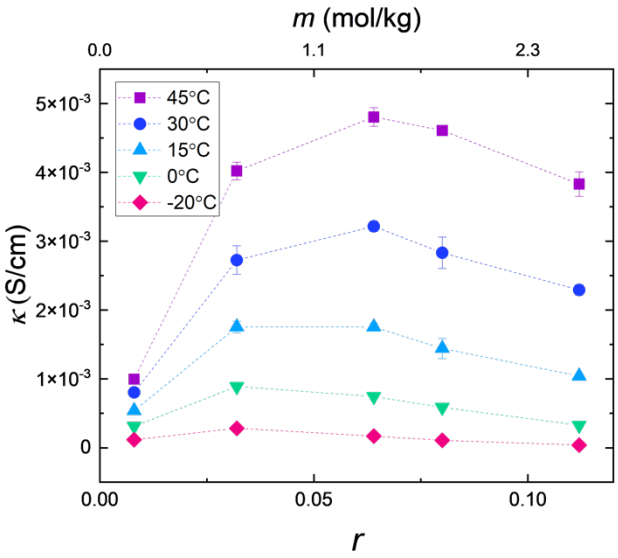

Figure S3.17. Ionic conductivity as a function of salt concentration at fixed temperatures. In most cases, error bars are smaller than the size of the data markers.

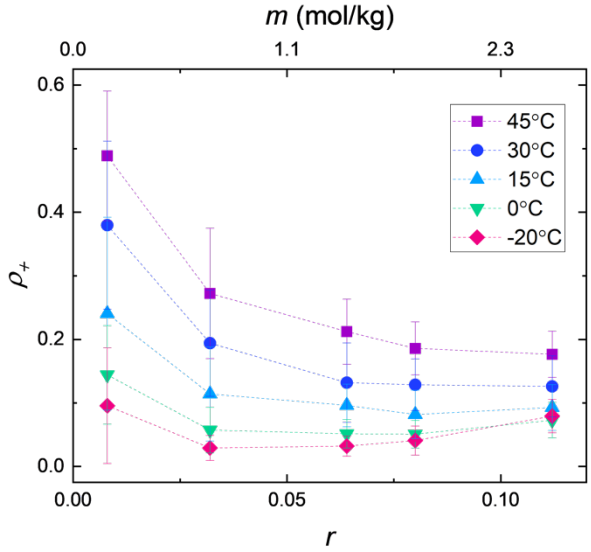

Figure S3.18. Current fraction, plotted as a function of salt concentration at fixed temperatures.

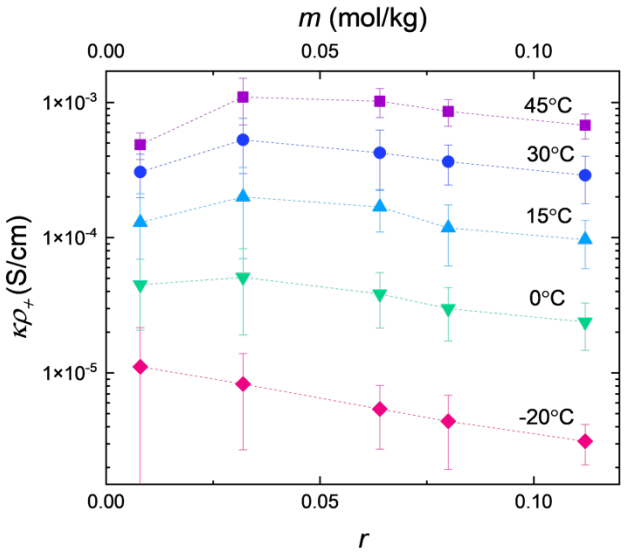

Figure S3.19. Effective conductivity, or the product of conductivity and current fraction, plotted as a function of salt concentration at fixed temperatures.

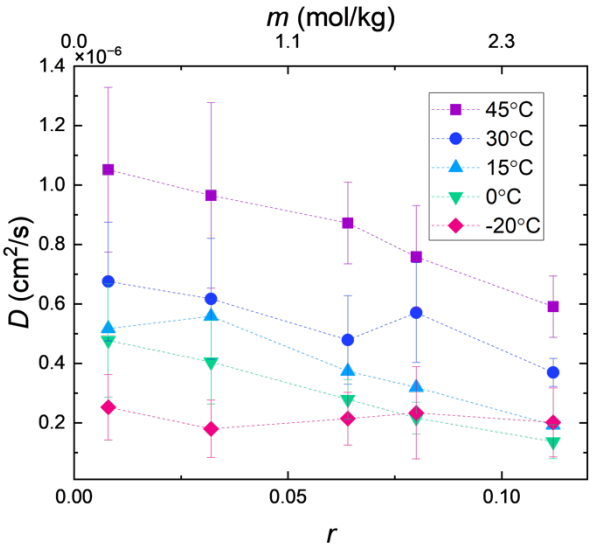

Figure S3.20. Diffusion coefficients measured via restricted diffusion, plotted as a function of salt concentration at fixed temperatures.

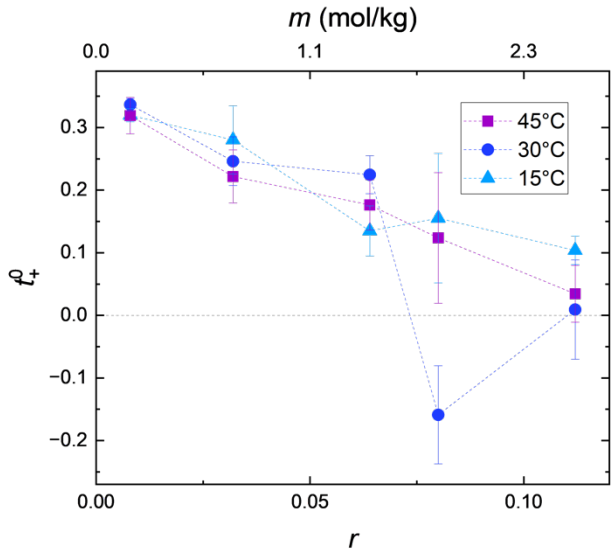

Figure S3.21. Cation transference numbers with respect to the solvent velocity, determined via eNMR, plotted as a function of salt concentration at fixed temperatures.

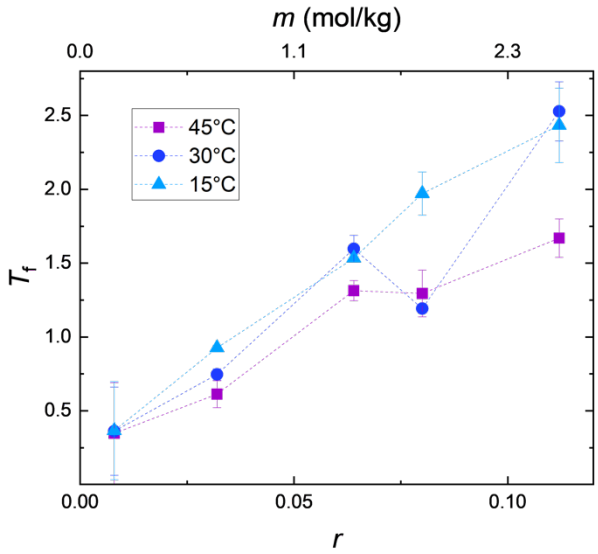

Figure S3.22. Thermodynamic factor, determined using transference numbers from eNMR, plotted as a function of salt concentration at fixed temperatures.

3.8.11 Fitting parameters for concentration gradient modeling.

Fitting parameters used for each transport and thermodynamic property are shown in Table S3.5. These parameters are distinct for each temperature and listed for 45, 30, 15, 0, and -20°C. Fitting parameters for the integrand in Equations 3.8 and 3.9 are also listed in Table S3.6 and Table S3.7, respectively, for each temperature.

Table S3.5. Fitting parameters for each temperature and thermodynamic property, given as a function of r.

$$\text{T} = 45°\text{C},\ P(r) = K_3 r^3 + K_2 r^2 + K_1 r + K_0$$

$P(r)$	K_3	K_2	K_1	K_0
κ	10.65	-2.834	0.2236	-6.144×10^{-4}
ρ_+	-575.3	149.2	-13.08	0.578
D	2.133×10^{-4}	-6.15×10^{-5}	1.337×10^{-7}	1.048×10^{-6}
$dU/dlnm$	-36.27	11.4	-1.656	1.191×10^{-2}

T =30°C, $P(r) = K_3r^3 + K_2r^2 + K_1r + K_0$

$P(r)$	K_3	K_2	K_1	K_0
κ	7.781	-2.026	0.1524	-2.887×10^{-4}
ρ_+	-659.8	163.8	-13.16	0.4724
D	-9.334×10^{-4}	1.656×10^{-4}	-1.033×10^{-5}	7.617×10^{-7}
$dU/dlnm$	-50.5	3.316	-0.7643	-6.72×10^{-3}

T = 15°C, $P(r) = K_3r^3 + K_2r^2 + K_1r + K_0$

$P(r)$	K_3	K_2	K_1	K_0
κ	6.893	-1.62	0.1061	-2.098×10^{-4}
ρ_+	-284.4	75.55	-6.47	0.2685
D	3.132×10^{-4}	-6.966×10^{-5}	8.507×10^{-7}	5.318×10^{-7}
$dU/dlnm$	-	-1.573	-0.7086	-8.673×10^{-3}

T = 0°C, $P(r) = K_3r^3 + K_2r^2 + K_1r + K_0$

$P(r)$	K_3	K_2	K_1	K_0
κ	3.634	-0.8401	5.187×10^{-2}	-5.116×10^{-5}
ρ_+	-288.4	73.58	-5.544	0.1752

D	3.104×10^{-4}	-5.145×10^{-5}	-1.283×10^{-6}	4.901×10^{-7}
$dU/dlnm$	-	-6.024	-0.3924	-1.57×10^{-2}

T = -20°C, $P(r) = K_4r^4 + K_3r^3 + K_2r^2 + K_1r + K_0$

$P(r)$	K_4	K_3	K_2	K_1	K_0
κ	-19.89	6.211	-0.6748	2.646×10^{-2}	-5.534×10^{-5}
ρ_+	-	-239.8	63.28	-4.407	0.1153
D	-	-8.332×10^{-4}	1.579×10^{-4}	-8.184×10^{-6}	3.08×10^{-7}
$dU/dlnm$	-	-	-6.917	-0.425	-1.537×10^{-2}

Table S3.6. Fitting parameters for the integrand term in Equation 3.8.

$P(r) = K_6r^6 + K_5r^5 + K_4r^4 + K_3r^3 + K_2r^2 + K_1r + K_0$

T (°C)	K_6	K_5	K_4	K_3	K_2	K_1	K_0
45°C	-0.1251	5.67×10^{-2}	-1.051×10^{-2}	1.015×10^{-3}	-5.338×10^{-5}	1.38×10^{-6}	-7.909×10^{-9}
30°C	4.739×10^{-2}	1.998×10^{-2}	-3.384×10^{-3}	2.874×10^{-4}	-1.218×10^{-5}	1.985×10^{-7}	1.85×10^{-9}
15°C	-1.41×10^{-2}	6.163×10^{-3}	-1.078×10^{-3}	9.564×10^{-5}	-4.402×10^{-6}	8.457×10^{-8}	5.579×10^{-10}
0°C	-1.59×10^{-3}	8.202×10^{-4}	-1.527×10^{-4}	1.256×10^{-5}	-3.854×10^{-7}	-3.977×10^{-9}	4.693×10^{-10}
-20°C	-2.2×10^{-3}	8.454×10^{-4}	-1.264×10^{-4}	8.969×10^{-6}	-2.769×10^{-7}	1.083×10^{-9}	9.793×10^{-11}

Table S3.7. Fitting parameters for the integrand term in Equation 3.9.

$P(r) = K_0 + K_1e^{-K_2r} + K_3e^{-K_4r}$

T (°C)	K_0	K_1	K_2	K_3	K_4
45°C	1.768×10^{-5}	-0.370	67.8	0.370	67.7
30°C	2.441×10^{-5}	1.615	37.55	-1.614	37.54

15°C	1.967×10^{-5}	0.755	95.33	-0.755	95.33
0°C	2.387×10^{-3}	1.566	51.48	-1.566	51.47
-20°C	2.747×10^{-5}	1.728	43.88	-1.728	43.88

3.9 Nomenclature

t_+^0	Cation transference number with respect to the solvent velocity
κ	Ionic conductivity (S cm^{-1})
D	Salt diffusion coefficient (cm^2 s^{-1})
T_f	Thermodynamic factor
ρ_+	Current fraction
r	Measure of ratio of lithium ions to oxygen atoms in solvent
ρ	Density
η	Viscosity
R_s	Series resistance (Ω)
τ	Tortuosity of separator
φ_c	Volume fraction of conducting phase in separator
l	Thickness of the separator (cm)
A	Area of electrodes (cm^2)
$R_{i,0}$	Initial interfacial resistance (Ω)
$R_{i,ss}$	Steady-state interfacial resistance (Ω)
ΔV	Applied voltage (V)
I_{ss}	Steady-state current (mA)
I_Ω	Initial current calculated via Ohm's law, $I_\Omega = \Delta V / R_T$ (mA)
U	Open circuit potential (mV)
k_0	Offset voltage (mV)
a	Fit parameter for restricted diffusion
b	Fit parameter for restricted diffusion
t	Time (s)
D_s	Salt diffusion coefficient through the separator (cm^2 s^{-1})
α	Minimum time cutoff for restricted diffusion
U	Open circuit potential, measured in concentration cells
Δ	Drift time for eNMR (s)
m	Molality (mol kg^{-1})
r_{max}	Salt concentration with maximum conductivity
κ_{max}	Value of conductivity at r_{max}
Λ	Molar conductivity
v_+	Cation velocity (μm cm^{-1})
v_-	Anion velocity (μm cm^{-1})
v_0	Solvent velocity (μm cm^{-1})
γ_{+-}	Mean molar activity coefficient
F	Faraday's constant (C mol^{-1})

R	Universal gas constant (8.314 J mol^{-1} K^{-1})
T	Temperature (°C)
$\mathfrak{D}$	Stefan-Maxwell diffusion coefficient (cm^2 s^{-1})
c	Concentration of the salt (mol cm^{-3})
c_0	Concentration of the solvent (mol cm^{-3})
c_T	Total concentration of the salt and solvent, $c_T = c_0 + c$ (mol cm^{-3})
t_-^0	Anion transference number with respect to the solvent velocity
i_{ss}	Steady-state applied current density, used in concentration gradient modeling (mA cm^{-2})
L	Distance between electrodes, used in concentration gradient modeling
z_-	Anion charge number
ν_-	Number of anions the salt dissolves into
x/L	Dimensionless position across the electrolyte, used in concentration gradient modeling
Φ_{ss}	Steady-state potential from concentration gradient modeling (V)
r_{avg}	Average concentration of the electrolyte, used in concentration gradient modeling

4 Toward Establishing Uniqueness of Experimentally Determined Transference Numbers

4.1 Abstract

The development of concentration gradients in response to polarization limits the rate at which batteries can be charged or discharged. For a fully characterized electrolyte, where the conductivity, salt diffusion coefficient, cation transference number, and the thermodynamic factor are known, concentration and potential gradients can be modeled based on Newman's concentrated solution theory. We have previously measured cation transference numbers using both electrochemical techniques and electrophoretic NMR. Electrochemical techniques require combining measurements from multiple experiments in order to determine the transference number, which can result in large error. Electrophoretic NMR, however, enables the precise determination of transference numbers. This leads to two methods for determining modeled concentration and potential gradients – one based on transference numbers determined form electrochemical methods and one based on transference numbers from electrophoretic NMR. The ability to uniquely determine the transference number is called into question. We compare the results from both types of modeling. Electrophoretic NMR predicts smaller concentration gradients compared to electrochemical methods, but expected potential gradients are remarkably similar between the two methods. Based on current – voltage relationships alone, it is not possible to distinguish between transference numbers obtained from electrochemical methods and electrophoretic NMR. Additional experiments – in the form of operando concentration profile measurements or polarization experiments in the vicinity of the limiting current – would be needed to distinguish between methods.

4.2 Introduction

Electrolytes used in lithium-ion batteries are composed of $LiPF_6$ salt dissolved in an organic solvent.[4,35] The solvent molecules preferentially interact with the lithium cation, resulting in bulky, solvated-lithium complexes.[79,113] In contrast, the anions are usually not complexed with the solvent. In a solution of uniform concentration, the current carried by even a bulky anion like PF_6 is thus often larger than that carried by the lithium ion.[62,108,114] The cation transference number, t_+^0, is defined as the fraction of current carried by the cation relative to the solvent velocity in a solution of uniform concentration.[5] In liquid electrolytes, t_+^0 is significantly less than unity. Efforts to increase t_+^0 have always resulted in a decrease in conductivity, κ.[7] Designing electrolytes is difficult because the transport of working ions depends on a multitude of parameters, and improving one of the parameters can result in worsening of another. Additional complications arise because even determining the magnitude (and sign) of these parameters unambiguously has proven to be challenging.

The passage of current results in the formation of salt concentration gradients,[105,108,115] which limit the rate at which batteries can be discharged or charged. Despite their importance, concentration gradients are difficult to quantify and must be measured in operando experiments using specialized techniques, such as x-ray transmission,[116] Raman microspectroscopy,[60] and magnetic resonance imaging (MRI) experiments.[117,118] The maximum current that can be passed through a given electrolyte is called the limiting current. The limiting current is obtained either if the salt concentration at the negative electrode[5] approaches zero or the salt concentration at the positive

electrode approaches the solubility limit.[102] Limiting current can be measured without using specialized instrumentation, as signatures of the limiting current are evident in standard time dependent voltage plots.[14,102,116] Limiting current is usually measured in lithium-lithium symmetric cells and has been reported for many polymer electrolyte systems.[57,101,107,119] For more reactive electrolytes, however, conducting experiments near or at the limiting current is difficult due to electrodeposition of mossy or dendritic lithium.[44,120,121] Such corruption of the interface can impact surface area, thickness of the electrolyte, salt concentration, and interfacial resistance. Measuring either concentration polarization or limiting current in liquid electrolytes is therefore not trivial.

In Newman's concentrated solution theory,[5] predicting ion transport in electrolytes requires knowledge of the thermodynamic factor, T_f, and three transport coefficients – t_+^0, κ, and salt diffusion coefficient, D. The standard approach for determining T_f, κ, D, and t_+^0 is based on four electrochemical experiments.[6,8,37,62] The combination of experiments needed to determine t_+^0 inevitably compounds experimental error and reduces precision in the final reports of t_+^0; discrepancies have been reported previously.[37,79] In an alternative approach, t_+^0 can be measured independently using electrophoretic NMR (eNMR),[58] a technique in which cation, anion, and solvent velocities are directly measured under applied electric and magnetic fields.[10,12,13,122] eNMR and concentrated solution theory can then be combined to determine T_f.

We have used both methods to characterize mixtures of lithium bis(trifluoromethanesulfonyl)imide (LiTFSI) salt dissolved in tetraethylene glycol dimethyl ether (tetraglyme) as a function of salt concentration and temperature.[89,123] The results of these two methods are summarized in Tables 4.1 and 4.2. Table 4.1 gives values of κ, D, the current fraction, ρ_+, and $dU/dlnm$ from concentration cell experiments, which are common to both methods. Table 4.2 gives T_f and t_+^0, which are dependent on the method. At a given salt concentration and temperature, the values reported in Table 4.2 differ greatly. For example, at 30°C and r = 0.032, $t_{+,eNMR}^0$ = 0.25$\pm$0.04 and $t_{+,echem}^0$ = -1.02$\pm$1.11. We use both sets of measured transport and thermodynamic parameters to model concentration and potential gradients that will form under an applied current using concentrated solution theory. The concentration gradients and the limiting current are approach dependent. Surprisingly, the voltage versus current characteristics are not. Because of the challenges in obtaining reliable polarization data at high applied currents, we compare the results of both models to data from small polarization experiments. The focus of this manuscript is to compare the results between these two models and discuss the challenge of unique determination of the transference number.

4.3 Experimental Methods

4.3.1 Electrolyte Preparation

Lithium bis(trifluoromethanesulfonyl)imide (LiTFSI) salt was obtained from Sigma-Aldrich and dried under active vacuum in a glovebox antechamber for three days at 100°C. Tetraethylene glycol dimethyl ether was obtained from Sigma-Aldrich and dried under active vacuum in a glovebox antechamber for three days at 60°C. Electrolytes were made by dissolving a known mass of salt in a known mass of solvent and stirring overnight at 25°C. Electrolytes were prepared in an argon glovebox with water and oxygen levels maintained below 1 ppm. The unit of concentration used in this work, r, relates the number of lithium ions in LiTFSI to the number of ether oxygens

in tetraglyme, r = ([Li$^+$]/[O]). The concentration of electrolytes used in this study are fully given in Table 4.1 in units of r, molality, m, and molarity, c.

4.3.2 Lithium-lithium Symmetric Cells and Polarization Experiments

Lithium-LiTFSI/tetraglyme-lithium symmetric cells were assembled in CR2032 coin cells (MTI Corp.) with five layers of Celgard 2500 separators soaked in electrolyte. The soaked separator stack (125 μm thick, 19 μm in diameter) was sandwiched between lithium chips (MTI Corp.). The stack was topped with a stainless steel spacer and a wave spring before crimping. Cells were assembled in triplicate for each concentration and temperature and cycled in an environmental chamber (JEIO Tech) to maintain a temperature setpoint, which was corroborated using a thermocouple.

Cells were preconditioned using alternating current densities of $\pm$0.02 mA/cm^2 using a Biologic VMP300 potentiostat. The sequence included a four hour positive polarization, a one hour rest, a four hour negative polarization, and a one hour rest. Preconditioning stabilizes the SEI between the tetraglyme electrolyte and lithium metal. A small constant voltage of ΔV = 10 mV was applied for one hour to the preconditioned cells until a steady-state current value, I_{ss}, was reached. Ac impedance spectroscopy was taken every 20 minutes to ensure the interfacial resistance, R_i, was stable. The interfacial resistance was used to subtract out the potential drop, Φ, across the interface and determine the potential drop within the bulk of the electrolyte in accordance with equation 4.1.

$$\Phi = \Phi_{measured} - R_i I_{ss} \tag{4.1}$$

Here, $\Phi_{measured}$ is the potential measured by the potentiostat during the constant voltage experiment.

4.3.3 Theory

Newman's concentrated solution theory has previously been used to derive the relationship between the steady-state current density, i_{ss}, and transport and thermodynamic properties of an electrolyte.[14] For a liquid electrolyte, which requires the presence of a porous separator to electrically insulate the electrodes, this relationship is given by equation 4.2,[102]

$$\int_{r(x=0)}^{r(x)} \frac{c(r)D_s(r)}{rt_-^0(r)}\,dr = \int_{r(x=0)}^{r(x)} J_1\,dr = \frac{i_{ss}L}{Fz_-\nu_-}\left(\frac{x}{L}\right), \tag{4.2}$$

where D_s is the salt diffusion coefficient measured by restricted diffusion in the electrolyte soaked separator,[54] t_-^0 is the anion transference number relative to the solvent velocity ($t_-^0 = 1 - t_+^0$), L is the thickness of the electrolyte, x/L is the relative position in the electrolyte, F is Faraday's constant, z_- is the charge number of the anion, and ν_- is the number of anions the salt dissociates into. D_s is related to the salt diffusion coefficient in the bulk of the electrolyte via the tortuosity, τ, of the separator via $D = \tau D_s$ (τ = 2.93 for Celgard 2500[89]). The integrand on the right side of equation 4.2 is defined as J_1. In this equation, our goal is to determine $r(x)$ for an average electrolyte concentration, r_{av}, current density, i, and thickness, L. An initial guess for $r(x = 0)$ is used to solve the integral iteratively until the numerical average across all positions of $r(x)$ matches r_{av}. The solved concentration gradient can then be used to solve for the steady-state potential, Φ_{ss}.

Φ_{ss}, the potential of the positive electrode relative to the negative electrode during steady-state polarization, can also be related to the measured transport and thermodynamic properties and is given in equation 4.3 for an electrolyte soaked separator.[102]

$$\Phi_{ss} = -Fz_{-}\nu_{-}\int_{r(x=L)}^{r(x=0)} J_2 dr = -Fz_{-}\nu_{-}\int_{r(x=L)}^{r(x=0)} \frac{c(r)D_s(r)}{r\rho_{+}(r)\kappa_s(r)t_{-}^{0}(r)}dr \tag{4.3}$$

Here, ρ_+ is the current fraction measured using the Bruce-Vincent approach[7,41–43] and κ_s is the conductivity measured in an electrolyte soaked separator. κ_s is related to the bulk conductivity of an electrolyte via $\kappa = \frac{\tau}{\varphi_c}\frac{l}{R_s A}$,[53] where φ_c is the volume fraction of the separator (φ_c = 0.55 for Celgard 2500[89]), l is the thickness of the electrolyte, R_s is the bulk resistance from ac impedance spectroscopy, and A is the area of the electrodes. The integrand on the right side of equation 4.3 is defined as J_2.

Generally, the cation transference number with respect to a solvent velocity is a calculated property that must be determined from multiple electrochemical experiments.[8,36–39] For a binary, univalent electrolyte, the relationship between cation transference number and other transport parameters is given by equation 4.4.[63]

$$t_{+}^{0} = 1 - t_{-}^{0} = 1 - \frac{FDc}{\kappa\frac{dU}{dlnm}}\left(\frac{1}{\rho_{+}} - 1\right) \tag{4.4}$$

Here, $\frac{dU}{dlnm}$ refers to the change in open circuit potential with respect to log of molality measured in a concentration cell experiment.[40] The relationship between the cation transference number and other transport and thermodynamic parameters can be used to replace t_+^0 in equations 4.2 and 4.3, which yields equations to predict concentration gradients (equation 4.5) and potential gradients (equation 4.6) based on parameters directly measured in electrochemical experiments.

$$\int_{r(x=0)}^{r(x)} \kappa(r)\left(\frac{dU}{dlnm}\right)(r)\left[r\tau F\left(\frac{1}{\rho_{+}(r)} - 1\right)\right]^{-1} dr = \frac{i_{ss}L}{Fz_{-}\nu_{-}}\left(\frac{x}{L}\right), \tag{4.5}$$

$$\Phi_{ss}(x=0) = -Fz_{-}\nu_{-}\int_{r(x=L)}^{r(x=0)}\left(\frac{dU}{dlnm}\right)(r)\left[rF\phi_c\left(1-\rho_{+}(r)\right)\right]^{-1}dr. \tag{4.6}$$

Equations 4.5 and 4.6 can be used to predict concentration and potential gradients based only on properties measured in electrochemical experiments. This method has been used in several previous works to predict measured potentials (Φ_{ss}) and limiting current (i_{limit}).[14,101,102,119] We will refer to this method as "electrochemical methods" or "echem" throughout this work because it depends on a transference number determined from electrochemical experiments.

Previous works have demonstrated that cation transference numbers can be directly measured via electrophoretic NMR (eNMR), a technique in which species' averaged velocities can be directly measured under applied electric and magnetic fields.[10,12,122,124] We have previously used eNMR to determine t_+^0 for LiTFSI/tetraglyme as a function of temperature and concentration.[58,89,123] The

combination of eNMR with electrochemical characterization robustly characterizes all transport and thermodynamic parameters within the electrolyte, including precise measurement of t_+^0. Due to the incorporation of eNMR, concentration and potential gradients can be predicted by directly plugging the cation transference number measured via eNMR, $t_{+,eNMR}^0$, into equations 4.2 and 4.3. For clarity, the modified forms of equations 4.2 and 4.3 are shown below in equations 4.7 and 4.8, respectively.

$$\int_{r(x=0)}^{r(x)} \frac{c(r)D(r)}{r\tau\left(1-t_{+,eNMR}^0(r)\right)}\,dr = \frac{i_{ss}L}{Fz_-\nu_-}\left(\frac{x}{L}\right), \tag{4.7}$$

$$\Phi_{ss}(x) = -Fz_-\nu_-\int_{r(x=L)}^{r(x=0)} \frac{c(r)D(r)}{r\phi_c\kappa(r)\rho_+(r)\left(1-t_{+,eNMR}^0(r)\right)}\,dr \tag{4.8}$$

Predicting concentration and potential gradients using transference numbers from eNMR is new to this work. We will refer to this method as "electrophoretic NMR" or "eNMR" throughout this work as it utilizes a transference number determined from eNMR.

Our main objective is to compare predictions of current-voltage relationships using echem and eNMR methods. The parameters needed to model these relationships are given in Tables 4.1 and 4.2. Figure 4.1 summarizes the parameters needed for each approach.

Electrochemical-Based Modeling	Electrophoretic NMR-Based Modeling
ρ_+ κ $\frac{dU}{dlnm}$	ρ_+ κ c D $t_{+,eNMR}^0$

Figure 4.1. Summary of transport and thermodynamic properties needed as inputs for predicting current-voltage relationships in each type of modeling.

4.4 Results and Discussion

Transport and thermodynamic properties have previously been determined for the LiTFSI/tetraglyme electrolyte as a function of salt concentration and temperature.[123] These properties are fully reported in Table 4.1 – including molality, m, molarity, c, conductivity, κ, diffusion coefficient, D, current fraction, ρ_+, and $dU/dlnm$ – and in Table 4.2 - including cation transference number, t_+^0, and the thermodynamic factor, T_f, determined from both echem and eNMR methods. Parts a-e of Table 4.1 and 4.2 correspond to data collected at 45°C, 30°C, 15°C, 0°C, and -20°C, respectively.

Table 4.1. Transport Properties Common to both Models for LiTFSI/tetraglyme at various temperatures.

a. T = 45°C

r	m (mol/kg)	c (mol/cm^3)	κ (S/cm)	D (cm^2/s)	ρ_+	$\frac{dU}{dlnm}$

0.008	0.18	0.174	[9.95±0.76]×10^{-4}	[1.05±0.28]×10^{-6}	0.49±0.10	[-1.29±1.28]×10^{-2}
0.032	0.72	0.647	[4.02±0.13]×10^{-3}	[9.66±3.13]×10^{-7}	0.28±0.10	[-2.62±0.36]×10^{-2}
0.064	1.45	1.190	[4.80±0.14]×10^{-3}	[8.73±1.37]×10^{-7}	0.21±0.05	[-5.93±0.11]×10^{-2}
0.08	1.79	1.427	[4.61±0.07]×10^{-3}	[7.58±1.73]×10^{-7}	0.19±0.04	[-6.22±0.19]×10^{-2}
0.112	2.52	1.851	[3.83±0.18]×10^{-3}	[5.91±1.03]×10^{-7}	0.18±0.04	[-8.84±0.55]×10^{-2}

b. T = 30°C

r	m (mol/kg)	c (mol/cm^3)	κ (S/cm)	D (cm^2/s)	ρ_+	$\frac{dU}{dlnm}$
0.008	0.18	0.176	[8.05±0.45]×10^{-4}	[6.76±2.00]×10^{-7}	0.38±0.13	[-1.25±1.03]×10^{-2}
0.032	0.72	0.655	[2.72±0.21]×10^{-3}	[6.17±2.03]×10^{-7}	0.19±0.08	[-2.94±0.52]×10^{-2}
0.064	1.45	1.204	[3.22±0.08]×10^{-3}	[4.79±1.49]×10^{-7}	0.13±0.06	[-6.47±0.18]×10^{-2}
0.08	1.79	1.444	[2.83±0.23]×10^{-3}	[5.71±1.68]×10^{-7}	0.13±0.04	[-7.22±0.10]×10^{-2}
0.112	2.52	1.872	[2.29±0.08]×10^{-3}	[3.70±0.47]×10^{-7}	0.13±0.05	[-1.31±0.10]×10^{-1}

c. T = 15°C

r	m (mol/kg)	c (mol/cm^3)	κ (S/cm)	D (cm^2/s)	ρ_+	$\frac{dU}{dlnm}$
0.008	0.18	0.179	[5.39±0.29]×10^{-4}	[5.18±1.41]×10^{-7}	0.24±0.15	[-1.23±1.12]×10^{-2}
0.032	0.72	0.664	[1.75±0.08]×10^{-3}	[5.59±1.45]×10^{-7}	0.11±0.07	[-3.31±0.02]×10^{-2}
0.064	1.45	1.219	[1.75±0.05]×10^{-3}	[3.74±0.38]×10^{-7}	0.10±0.03	[-6.59±0.11]×10^{-2}
0.08	1.79	1.461	[1.44±0.15]×10^{-3}	[3.19±0.33]×10^{-7}	0.08±0.04	[-8.27±0.43]×10^{-2}
0.112	2.52	1.894	[1.04±0.03]×10^{-3}	[1.93±0.21]×10^{-7}	0.09±0.04	[-1.08±0.11]×10^{-1}

d. T = 0°C

r	m (mol/kg)	c (mol/cm^3)	κ (S/cm)	D (cm^2/s)	ρ_+	$\frac{dU}{dlnm}$
0.008	0.18	0.181	[3.12±0.01]×10^{-4}	[4.77±1.91]×10^{-7}	0.14±0.08	[-5.56±1.16]×10^{-3}
0.032	0.72	0.672	[8.89±0.03]×10^{-4}	[4.05±1.41]×10^{-7}	0.06±0.04	[-3.47±0.05]×10^{-2}
0.064	1.45	1.233	[7.45±0.03]×10^{-4}	[2.79±0.67]×10^{-7}	0.05±0.02	[-6.75±0.80]×10^{-2}
0.08	1.79	1.478	[5.87±0.01]×10^{-4}	[2.17±0.53]×10^{-7}	0.05±0.02	[-8.81±0.48]×10^{-2}
0.112	2.52	1.915	[3.27±0.01]×10^{-4}	[1.37±0.57]×10^{-7}	0.07±0.03	[-1.34±0.17]×10^{-1}

e. T = -20°C

r	m (mol/kg)	c (mol/cm^3)	κ (S/cm)	D (cm^2/s)	ρ_+	$\frac{dU}{dlnm}$
0.008	0.18	0.184	[1.16±0.01]×10^{-4}	[2.53±1.10]×10^{-7}	0.10±0.09	[-1.10±1.07]×10^{-2}
0.032	0.72	0.683	[2.83±0.07]×10^{-4}	[1.80±0.96]×10^{-7}	0.03±0.02	[-3.61±0.04]×10^{-2}
0.064	1.45	1.253	[1.68±0.07]×10^{-4}	[2.14±0.89]×10^{-7}	0.03±0.02	[-8.00±0.63]×10^{-2}
0.08	1.79	1.501	[1.08±0.02]×10^{-4}	[2.34±1.55]×10^{-7}	0.04±0.02	[-9.65±0.70]×10^{-2}
0.112	2.52	1.944	[3.94±0.06]×10^{-5}	[2.02±1.16]×10^{-7}	0.08±0.03	[-1.48±0.19]×10^{-1}

Table 4.2 Transport Properties Unique to each Model for LiTFSI/tetraglyme at various temperatures.

a. T = 45°C

r	$t^0_{+,echem}$	$t^0_{+,eNMR}$	$T_{f,echem}$	$T_{f,eNMR}$
0.008	-0.43±1.50	0.32±0.03	0.16±0.17	0.35±0.34
0.032	-0.53±0.79	0.22±0.04	0.31±0.16	0.61±0.09
0.064	-0.31±0.38	0.18±0.04	0.83±0.24	1.31±0.07
0.08	-0.60±0.51	0.12±0.10	0.71±0.23	1.29±0.16
0.112	-0.46±0.41	0.03±0.05	1.11±0.31	1.67±0.13

b. T = 30°C

r	$t^0_{+,echem}$	$t^0_{+,eNMR}$	$T_{f,echem}$	$T_{f,eNMR}$
0.008	-0.86±1.75	0.34±0.01	0.13±0.12	0.36±0.30
0.032	-1.02±1.11	0.25±0.04	0.28±0.15	0.75±0.05
0.064	-0.76±1.00	0.22±0.03	0.70±0.40	1.60±0.11
0.08	-1.64±1.16	-0.16±0.08	0.52±0.23	1.19±0.08
0.112	-0.54±0.63	0.01±0.08	1.62±0.67	2.53±0.28

c. T = 15°C

r	$t^0_{+,echem}$	$t^0_{+,eNMR}$	$T_{f,echem}$	$T_{f,eNMR}$
0.008	-3.24±4.81	0.32±0.01	0.06±0.06	0.36±0.33
0.032	-3.79±3.35	0.28±0.05	0.14±0.10	0.93±0.07
0.064	-2.58±1.30	0.13±0.04	0.37±0.14	1.53±0.08
0.08	-3.23±2.08	0.16±0.10	0.39±0.19	1.97±0.26
0.112	-2.06±1.27	0.10±0.02	0.71±0.30	2.43±0.26

d. T = 0°C

r	$t^0_{+,echem}$	$t^0_{+,eNMR}$	$T_{f,echem}$	$T_{f,eNMR}$
0.008	-27.6±62.7	-	0.004±0.009	-
0.032	-13.0±10.0	-	0.05±0.04	-
0.064	-11.2±6.24	-	0.12±0.06	-
0.08	-10.1±5.49	-	0.17±0.08	-
0.112	-6.36±4.29	-	0.39±0.23	-

e. T = -20°C

r	$t^0_{+,echem}$	$t^0_{+,eNMR}$	$T_{f,echem}$	$T_{f,eNMR}$
0.008	-32.4±47.8	-	0.008±0.011	-
0.032	-37.5±33.1	-	0.02±0.02	-
0.064	-56.9±38.6	-	0..03±0.02	-
0.08	-75.6±66.7	-	0.03±0.03	-
0.112	-74.2±50.8	-	0.04±0.03	-

The concentration profile in an electrolyte given some steady applied current, i_{ss}, and thickness can be determined using equations 4.5 and 4.7. Function J_1 based on electrochemical methods is given by:

$$J_{1,echem} = \frac{c(r)D_s(r)}{rt^0_-(r)} = \kappa(r)\left(\frac{dU}{dlnm}\right)(r)\left[r\tau F\left(\frac{1}{\rho_+(r)} - 1\right)\right]^{-1} \tag{4.9}$$

Function J_1 given by electrophoretic NMR is given by:

$$J_{1,eNMR} = \frac{c(r)D_s(r)}{rt^0_-(r)} = \frac{c(r)D(r)}{r\tau\left(1 - t^0_{+,eNMR}(r)\right)} \tag{4.10}$$

$J_{1,echem}$ and $J_{1,eNMR}$ were calculated using equations 4.9 and 4.10 and are plotted as a function of r at 30°C in Figure 4.2. Both functions were fit to continuous polynomial functions and the fit parameters are given in Table S4.3 (Supporting Information) for each method and temperature. The curves in Figure 4.2 show these fits. The transport parameters used as inputs to these expressions were also fit to continuous functions before being combined in the integrand. The fits for each parameter at each temperature are listed in Table S4.4 (Supporting Information). These integrating functions are relevant for the measured concentration range, $0.008 < r < 0.112$. $J_{1,eNMR}$ is an order of magnitude larger than $J_{1,echem}$. Since τ, c, and D are the same in both methods, the main difference between the J_1 functions arises due to differences in the

concentration-dependent transference numbers. Over the concentration range of interest, $t^0_{+,eNMR}$ ranges between 0.34 and 0.16 while $t^0_{+,echem}$ ranges between -0.54 and -1.64. The lack of uniqueness of transference numbers measured by the two different methods is obvious.

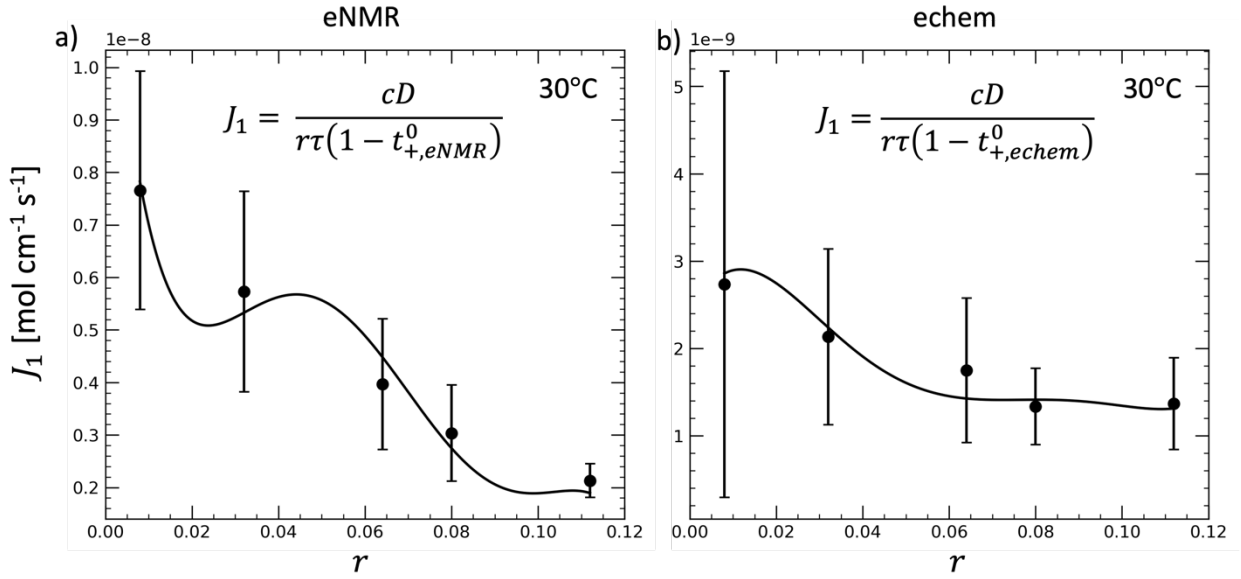

Figure 4.2. Fit of the integrand term, J_1, with respect to salt concentration (r) for a) eNMR based fitting and b) echem only based fitting for an exemplary temperature, T = 30°C. Markers show finite values determined from measured transport parameters and the line shows the least-squares polynomial fit given by equation 4.9. Parameters used to fit across all temperatures are fully listed in Table S4.3.

For a given current density, i_{ss}, J_1 can be used to compute the salt concentration gradient in an electrochemical cell using equations 4.5 and 4.7 for echem and eNMR methods, respectively. Typical results are shown in Figure 4.3, where concentration is plotted as a function of position for the same length-normalized current density, $i_{ss}L$, of 2.5 × 10^{-3} mA/cm. The predicted concentration profiles across three electrolyte concentrations at selected temperatures are shown for both types of modeling. Not surprisingly, both methods predict that concentration gradients increase in magnitude with decreasing temperature. At 45°C, the difference between echem and eNMR is relatively unimportant. In contrast, significant differences are evident at 15°C. In other words, the difference between the echem and eNMR transference numbers only becomes important when the magnitude of the concentration gradients is large.

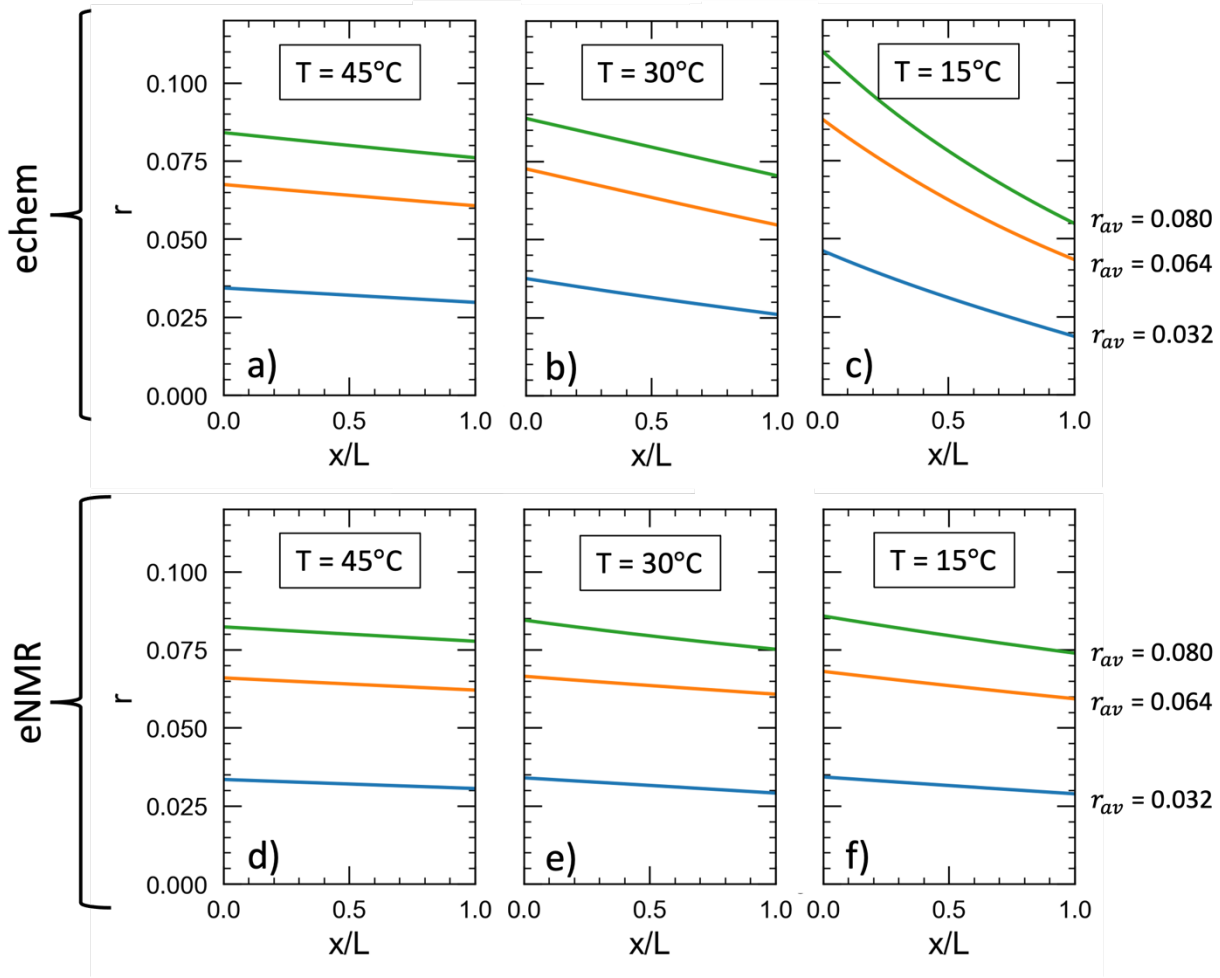

Figure 4.3. Predicted concentration profiles of LiTFSI/tetraglyme for an applied steady-state current density $i_{ss}L$ = 2.5 × 10^{-3} mA/cm for (a-c) electrochemical based modeling (equation 4.5) at (a) 45°C, (b) 30°C, and (c) 15°C and electrophoretic NMR based modeling (equation 4.7) for (d) 45°C, (e) 30°C, and (f) 15°C.

To quantify concentration gradients, we determine Δr, the difference between the maximum salt concentration, at x/L = 0, and the minimum salt concentration, at x/L = 1. Δr is shown in Figure 4.4a as a function of temperature for the same $i_{ss}L$ of 2.5 × 10^{-3} mA/cm. At the highest temperature, 45°C, electrochemical methods predict Δr slightly larger than eNMR. This difference becomes larger at lower temperatures – at 15°C, echem predicts Δr approximately five times greater than eNMR. In Figure 4.4b, we show Δr as a function of $i_{ss}L$ at 30°C. As the applied current is increased, Δr predicted by echem and eNMR methods diverge. Predicting concentration gradients in the limit of large currents requires unambiguous determination of the transference number.

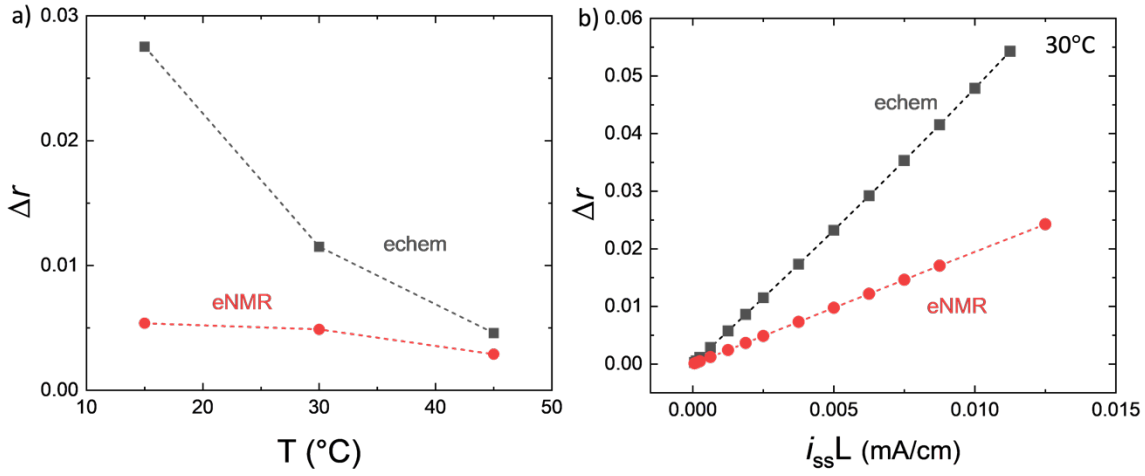

Figure 4.4. Magnitude of modeled salt concentration gradient, measured as the difference between r at x/L = 0 and x/L = 1. This is shown for both echem and eNMR based modeling (a) as a function of temperature and (b) as a function of $i_{ss}L$ for an exemplary salt concentration of r_{av} = 0.032 at 30°C.

One important metric of an electrolyte's overall performance is the limiting current, i_{limit} – the current at which salt concentration at x/L = 1 approaches 0. The limiting current can be predicted from the modeling by applying increasing $i_{ss}L$ values and determining r at x/L = 1. In Figure 4.5, we plot the applied $i_{ss}L$ versus this concentration for both methods. r at x/L = 1 decreases as the applied current increases. We can only predict concentration gradients over a finite concentration range because we have only measured transport and thermodynamic parameters between $0.008< r <0.112$. The limiting current is obtained by extrapolating the predictions as shown in Figure 4.5.

Given the vast difference in predictions of Δr, electrochemical methods and eNMR predict different limiting currents. Length-normalized predicted limiting currents, $i_{limit}L$, based on the two methods, are shown in Figure 4.6 as a function of temperature. Across the temperature range, eNMR predicts $i_{limit}L$ about 2.2-5.3 times greater than electrochemical methods. Determining the limiting current in liquid electrolytes is challenging due to the reactivity of lithium metal against liquid electrolytes.[44,50,50,121] Passing high currents through our electrolyte results in significant changes to the interfacial resistance, indicating corruption of the lithium-electrolyte interface. As a result of these experimental challenges, the limiting current hasn't yet been experimentally determined in LiTFSI/tetraglyme.

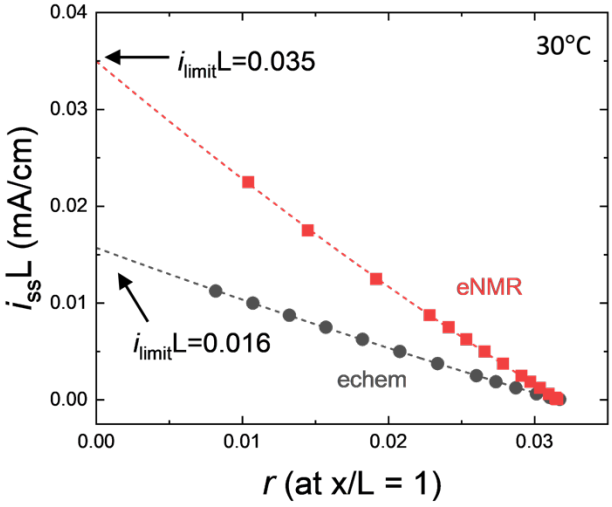

Figure 4.5. Predictions of concentration at the cathode (x/L = 1) for varying $i_{ss}L$ values for an electrolyte with an average salt concentration of r = 0.032. Modeling done using eNMR inputs and echem inputs are both shown to demonstrate the agreement in the model at low values of $i_{ss}L$ and the divergence near the limiting current. The dashed curves are the least-squares polynomial fit for each data set and is used to extrapolate the limiting current.

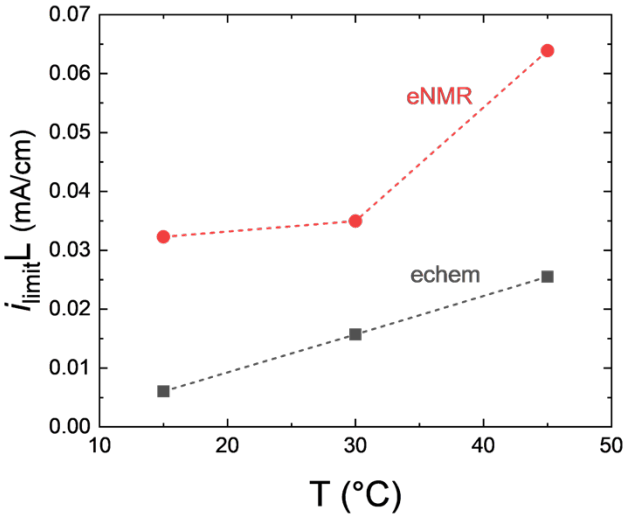

Figure 4.6. Limiting current predictions for echem and eNMR based modeling, shown as a function of temperature for a salt concentration of r = 0.032.

Despite the challenges with measurements in liquid electrolytes at high applied currents, it's possible to make comparisons between theory and experiment at small, applied potentials. We can predict potential gradients in an electrolyte at a given steady current, i_{ss}, and thickness via equations 4.6 and 4.8. Function J_2 based on electrochemical methods is given by:

$$J_{2,echem} = \frac{c(r)D_s(r)}{r\rho_+(r)\kappa_s(r)t_-^0(r)} = \left(\frac{dU}{dlnm}\right)(r)\left[rF\phi_c\left(1-\rho_+(r)\right)\right]^{-1} \tag{4.11}$$

Function J_2 given by electrophoretic NMR is given by:

$$J_{2,eNMR} = \frac{c(r)D_s(r)}{r\rho_+(r)\kappa_s(r)t_-^0(r)} = \frac{c(r)D(r)}{r\phi_c\kappa(r)\rho_+(r)\left(1-t_{+,eNMR}^0(r)\right)} \tag{4.12}$$

$J_{2,echem}$ and $J_{2,eNMR}$ were calculated using equations 4.11 and 4.12 and are plotted as a function of r at 30°C in Figure 4.7. Both functions were fit to continuous polynomial functions and the fit parameters are given in Table S4.5 (Supporting Information) for each method and temperature. The curves in Figure 7 show these fits. Similar to J_1, $J_{2,eNMR}$ is an order of magnitude larger than $J_{2,echem}$ due to differences in the concentration-dependent transference numbers used for each method of modeling.

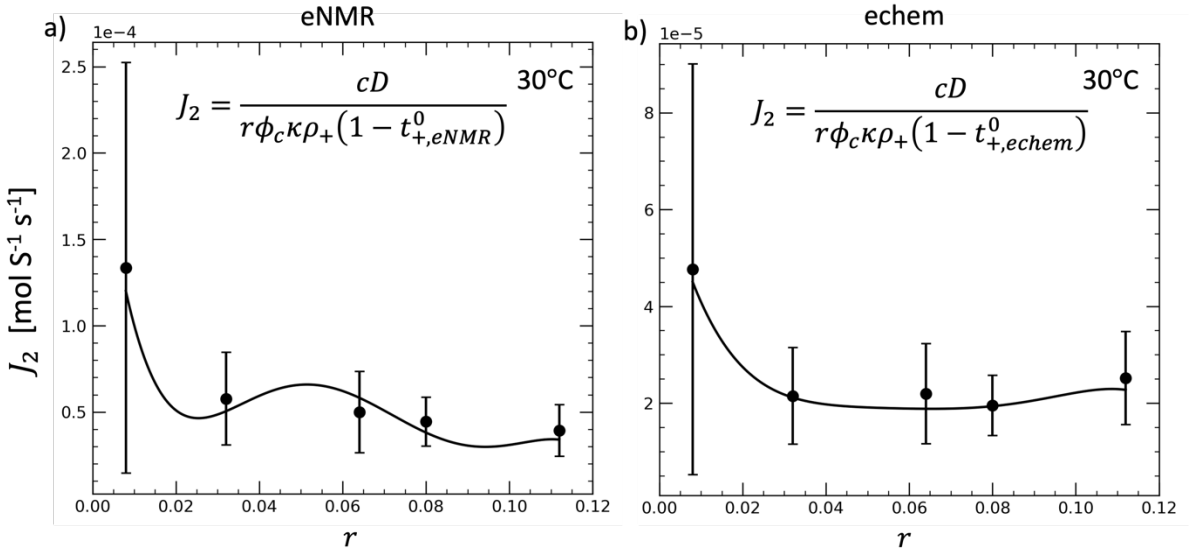

Figure 4.7. Fit of the integrand term, J_2, with respect to salt concentration (r) for an exemplary temperature, T = 30°C. Markers show finite values determined from measured transport parameters and the line shows the least-squares polynomial fit given by equation 4.10. Parameters used to fit across all temperatures are fully listed in Table S3.

J_2 can be used to compute the potential profiles for a given i_{ss} using equations 4.6 and 4.8 for electrochemical methods and eNMR, respectively. Typical results are shown in Figure 4.8, where potential is plotted as a function of position for the same length-normalized current density, $i_{ss}L$, of 2.5 × 10^{-3} mA/cm. The predicted potential profiles across three electrolyte concentrations at selected temperatures are shown for both methods of modeling. As seen with predicted concentration gradients (Figure 4.3), potential gradients increase with decreasing temperature – approximately 15 mV for the three salt concentrations at 45°C but up to 100 mV at 15°C. However, there is not a significant difference between the potential gradients predicted by electrochemical methods and electrophoretic NMR across the temperature range.

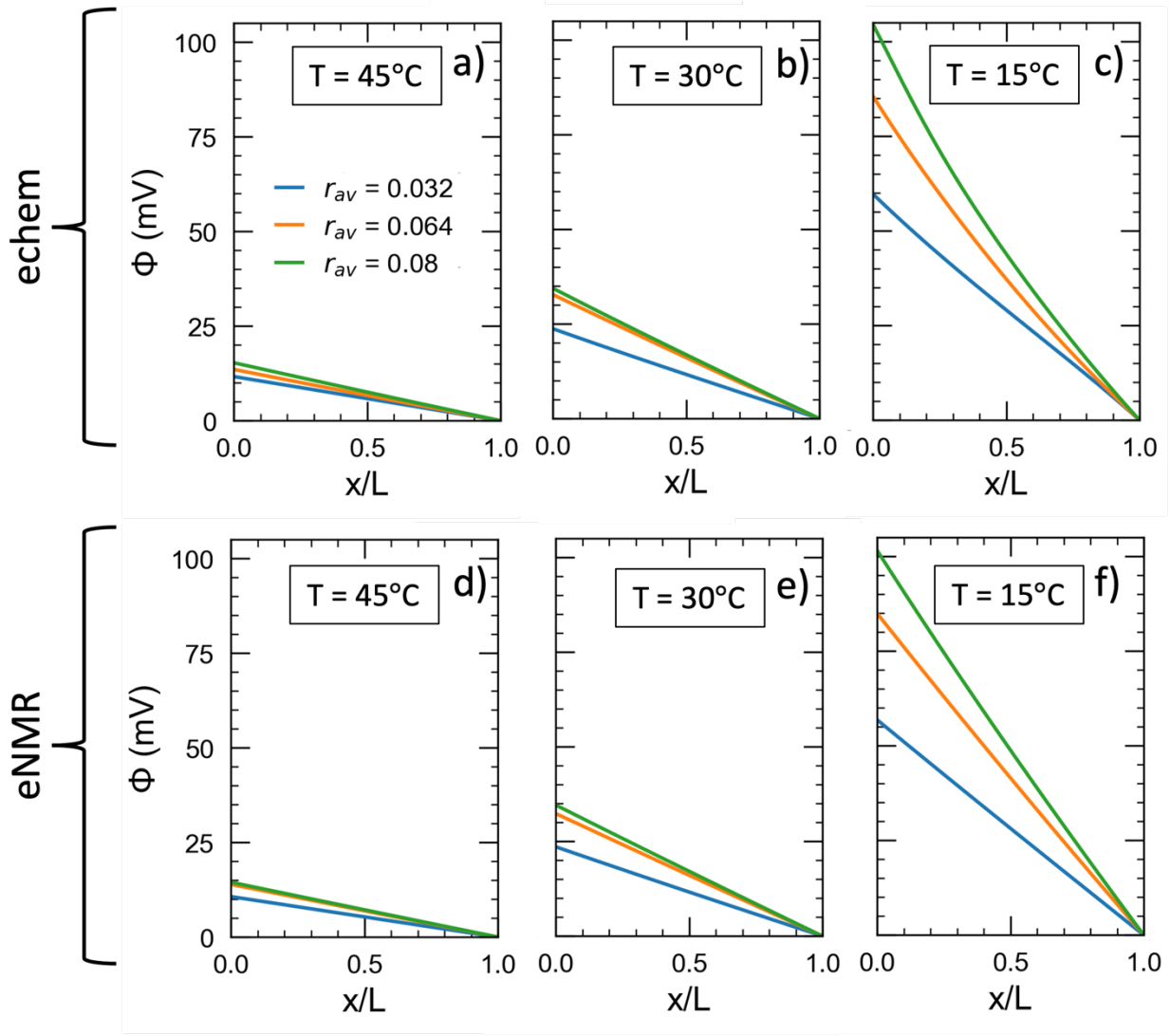

Figure 4.8. Predicted potential profiles of LiTFSI/tetraglyme for an applied steady-state current density $i_{ss}L = 2.5 \times 10^{-3}$ mA/cm for (a-c) electrochemical based modeling (equation 4.6) at (a) 45°C, (b) 30°C, and (c) 15°C and electrophoretic NMR based modeling (equation 4.8) for (d) 45°C, (e) 30°C, and (f) 15°C.

To further quantify the similarity in predicted potential, we show length-normalized potential, Φ_{ss}/L, for both echem and eNMR methods in Figure 4.9 for $r = 0.032$. In Figure 4.9a, we show the effect of T on Φ_{ss}/L for the applied current density, $i_{ss}L = 2.5 \times 10^{-3}$ mA/cm . In Figure 4.9b, we show the effects of $i_{ss}L$ at a fixed temperature of 30°C. Figure 4.4a and 4.4b show Δr as a function of T and $i_{ss}L$ for the same systems shown in Figure 4.9a and 4.9b. The agreement between the two methods in Figure 4.9 is surprising given the large difference in predictions of Δr, shown in Figure 4.4. Φ_{ss}/L is plotted as a function of $i_{ss}L$ for two additional salt concentrations in Figure S4.13 (Supplemental Information), and they show equally good agreement between the two methods of modeling.

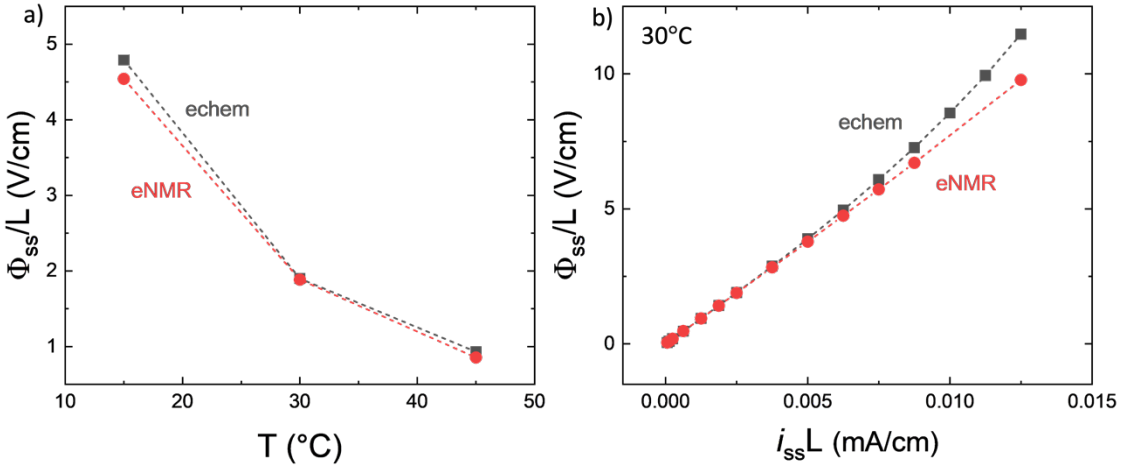

Figure 4.9. Magnitude of modeled potential gradient, shown for both echem and eNMR based modeling (a) as a function of temperature for an exemplary salt concentration of r = 0.032 and (b) as a function of $i_{ss}L$ for T = 30°C.

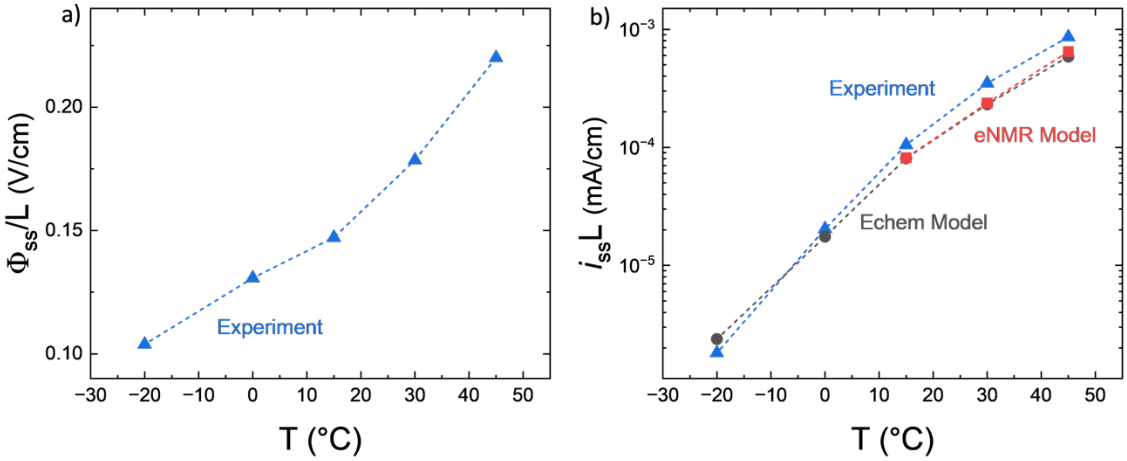

Figure 4.10. Comparison between experimental and predicted steady-state currents using electrochemical based modeling for an exemplary salt concentration, r = 0.032. The corresponding experimentally measured potential, Φ/L, which is used as input to the modeling to determine $i_{ss}L$, is also shown on the secondary y-axis, for clarity.

In Figure 4.10, we show the results of experiments conducted at a fixed applied potential gradient, $\Phi_{measured}/L$ = 0.8 V/cm. The potential gradient across the electrolyte, Φ_{ss}/L, varies with temperature because of changes in the interfacial impedance (see equation 4.1 for the definition of Φ_{ss}). In Figure 4.10a, we plot Φ_{ss}/L as a function of temperature. The experimentally measured steady current, $i_{ss}L$, is plotted as a function of temperature in Figure 4.10b. Also shown in Figure 4.10b are predictions of $i_{ss}L$ based on eNMR and echem methods. The predictions are obtained by assuming a value for $i_{ss}L$, obtaining Φ_{ss} using equations 4.6 and 4.8, and iteratively solving for $i_{ss}L$ until Φ_{ss}/L agrees with the experimental value. We find quantitative agreement between echem modeling, eNMR modeling, and experiment. The reason for the agreement between echem and eNMR modeling in predicted Φ_{ss}/L or $i_{ss}L$ is clarified in Figure 4.11. Here we show the same

J_2 functions shown earlier in Figure 4.7. The shaded bands in Figure 4.11 correspond to the magnitude of the concentration gradient from eNMR and echem modeling for an applied current density of $i_{ss}L$ = 2.5 × 10^{-3} mA/cm for r_{av} = 0.032 . The calculated current depends on the area of the shaded regions in Figure 4.11. The differences in both J_2 and Δr obtained using the different methods is such that the areas of the shaded regions are almost identical. Despite the difference in modeled concentration gradients, both methods of modeling show remarkably similar predictions for current – voltage relationships. These predictions agree well with experimental polarizations, as shown in Figure 4.10b.

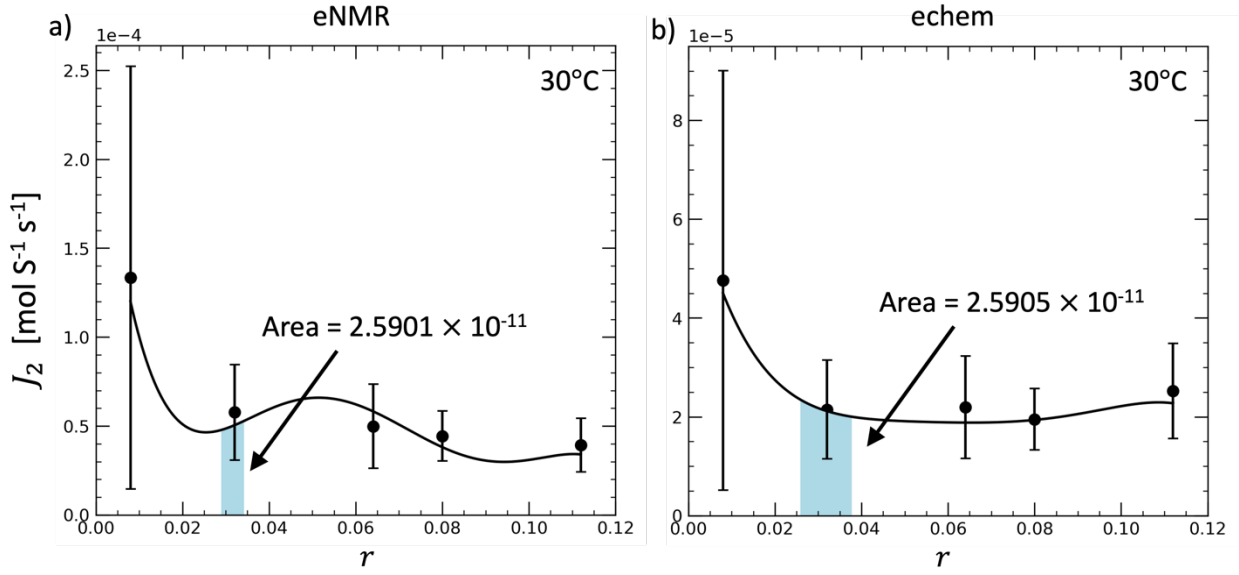

Figure 4.11. Fit of the integrand term, J_2, with respect to salt concentration (r) for an exemplary temperature, T = 30°C, replotted from Figure 4.7. Additionally shown in the figure is the shaded integral that spans the magnitude of the concentration gradient for an applied current of $i_{ss}L$ = 2.5 × 10^{-3} mA/cm for r_{av} = 0.032. The difference in the magnitude of J_2 between eNMR and echem methods is compensated by the difference in magnitude of the concentration gradient. This results in an integral that is nearly the same value between the two methods.

4.5 Conclusion

In concentrated solution theory, current versus voltage characteristics of an electrolyte depend on three transport coefficients, κ, D, and t_+^0, and a thermodynamic factor, T_f. Our objective is to determine these parameters uniquely in LiTFSI/tetraglyme mixtures as a function of salt concentration and temperature. We previously determined t_+^0 using two approaches and obtained very different values. For example, at r = 0.032 at 30°C, t_+^0 is -1.02±1.11 based on the standard electrochemical approach. Electrophoretic NMR enables determination of t_+^0 directly without having to solve for T_f simultaneously. Under the same conditions, t_+^0 determined using eNMR is 0.25 ±0.04. We see the same discrepancy in t_+^0 between eNMR and echem across the entire salt concentration and temperature range that we've studied. Which of these two values is correct is an interesting open question. If we were to restrict our attention to voltage – current relationships, it is impossible to determine if the correct value of t_+^0 is -1.02 or 0.25, as shown in Figure 4.11. Both values (with different values of T_f due to the interrelationship between t_+^0 and T_f, see equation 4.4)

give the identical values for the current obtained under an applied potential at a variety of temperatures.

In the standard approach for determining these parameters, based on ac impedance spectroscopy, restricted diffusion, current fraction (or current interrupt), and concentration cell experiments, the expressions used to determine t_+^0 and T_f are nonlinear and coupled. Thus, t_+^0 and T_f must be obtained by solving two nonlinear equations simultaneously. The fact that nonlinear equations can have multiple roots is well recognized. It should thus not be surprising if the solution to the two nonlinear equations relating t_+^0 and T_f to experimentally measured parameters exhibit multiple roots. In the eNMR approach, t_+^0 is determined from an independent equation and is uncoupled to the determination of T_f. Due to the simplicity of the eNMR approach, the most likely value of t_+^0 for our electrolyte is 0.25.

To determine the value of t_+^0 uniquely, additional information about the magnitude of concentration gradients, or Δr, is needed. One approach is to measure Δr directly in operando experiments, such as Raman microspectroscopy or x-ray transmission. A different approach is to conduct polarization experiments in the vicinity of the limiting current, which indirectly probe the magnitude of salt concentration gradients. Although concentration gradients alone can't provide all relevant information to fully characterize electrolytes, the independent measurement of Δr in addition to full characterization would make it possible to distinguish between eNMR and echem based transference numbers. In the absence of such data, it is possible to rationalize current – voltage relationships using transference numbers as different as -1.02 and 0.25.

4.6 Acknowledgments

This work was supported by the Vehicle Technologies Office of the U.S. Department of Energy's Office of Energy Efficiency and Renewable Energy under the guidance of the Advanced Battery Cell Research Program (eXtreme fast charge Cell Evaluation of Lithium-ion batteries, XCEL). Mark Wang is gratefully acknowledged for helpful discussions on implementation of modeling in Python and general programming advice.

4.7 Supporting Information

4.7.1 Fitting Parameters for Concentration and Potential Gradient Modeling

Here, we show a complete list of fitting parameters used to solve for concentration and potential gradient modeling. In Table S4.3, we show fitting parameters for the continuous least-squares polynomials for J_1. These fits are used to solve for concentration profiles in the electrolytes for a) electrochemical-based modeling and b) electrophoretic NMR-based modeling. J_1 and J_2 are fit using continuous fits for all transport and thermodynamic properties. Fitting parameters for the continuous least-squares polynomials for each parameter are given in Table S4.4. Parts (a-e) correspond to temperatures between 45 and -20°C. In Table S4.5, we show fitting parameters for the continuous least-squares polynomials for J_2. These fits are used to solve for potential profiles in the electrolytes for a) electrochemical-based modeling and b) electrophoretic NMR-based modeling.

Table S4.3 Fitting Parameters for Integrating Term, J_1, for Concentration Profile Modeling.

a. Electrochemical Model

$$J_1 = k_0 + k_1 r + k_2 r^2 + k_3 r^3 + k_4 r^4 + k_5 r^5$$

T(°C)	k_0	k_1	k_2	k_3	k_4	k_5
45°C	-6.61×10^{-9}	1.15×10^{-6}	-3.86×10^{-5}	5.85×10^{-4}	-4.21×10^{-3}	1.17×10^{-2}
30°C	2.34×10^{-9}	1.10×10^{-7}	-6.58×10^{-6}	1.25×10^{-4}	-1.00×10^{-3}	2.92×10^{-3}
15°C	7.05×10^{-10}	5.81×10^{-8}	-2.74×10^{-6}	4.72×10^{-5}	-3.68×10^{-4}	1.09×10^{-3}
0°C	5.36×10^{-10}	-1.46×10^{-8}	1.75×10^{-7}	-7.16×10^{-7}	-	-
-20°C	1.33×10^{-10}	-4.88×10^{-9}	6.98×10^{-8}	-3.58×10^{-7}	3.60×10^{-7}	-

b. Electrophoretic NMR Model

$$J_1 = k_0 + k_1 r + k_2 r^2 + k_3 r^3 + k_4 r^4 + k_5 r^5$$

T(°C)	k_0	k_1	k_2	k_3	k_4	k_5
45°C	1.25×10^{-8}	-1.37×10^{-7}	1.02×10^{-6}	-4.61×10^{-6}	-	-
30°C	1.33×10^{-8}	-9.75×10^{-7}	4.10×10^{-5}	-7.47×10^{-4}	5.98×10^{-3}	-1.74×10^{-2}
15°C	6.47×10^{-9}	-4.45×10^{-8}	-3.68×10^{-7}	3.15×10^{-6}	-	-

Table S4.4 Fitting parameters for each temperature and thermodynamic property, given as a function of r.

a. T = 45°C

$$P(r) = k_0 + k_1 r + k_2 r^2 + k_3 r^3$$

$P(r)$	k_0	k_1	k_2	k_3
κ (S/cm)	-6.14×10^{-4}	0.224	-2.84	10.65
ρ_+	0.578	-13.08	149.2	-575.3
D (cm^2/s)	1.05×10^{-6}	1.34×10^{-7}	-6.15×10^{-5}	2.13×10^{-4}
$dU/dlnm$	1.19×10^{-2}	-1.66	11.4	-36.27
$t^0_{+,eNMR}$	0.370	-7.13	98.04	-545.9
c (mol/cm^3)	1.02×10^{-5}	0.021	-0.043	-

b. T = 30°C

$$P(r) = k_0 + k_1 r + k_2 r^2 + k_3 r^3 + k_4 r^4$$

$P(r)$	k_0	k_1	k_2	k_3	k_4

κ (S/cm)	-2.89×10^{-4}	0.152	-2.03	7.78	-
ρ_+	0.472	-13.2	163.8	-659.8	-
D (cm^2/s)	7.62×10^{-7}	-1.03×10^{-5}	1.66×10^{-4}	-9.33×10^{-4}	-
$dU/dlnm$	-6.72×10^{-3}	-0.764	3.32	-50.5	-
$t^0_{+,eNMR}$	0.771	-76.3	3103	-4.50×10^{-4}	2.04×10^{-5}
c (mol/cm^3)	1.02×10^{-5}	0.0214	-0.043×10^{-2}		

c. T = 15°C

$$P(r) = k_0 + k_1 r + k_2 r^2 + k_3 r^3$$

$P(r)$	k_0	k_1	k_2	k_3
κ (S/cm)	-2.10×10^{-4}	0.106	-1.62	6.89
ρ_+	0.270	-6.47	75.55	-284.4
D (cm^2/s)	5.32×10^{-7}	8.51×10^{-7}	-6.97×10^{-5}	3.13×10^{-4}
$dU/dlnm$	-8.67×10^{-3}	-0.709	-1.57	-
$t^0_{+,eNMR}$	0.317	1.14	-102.5	673.0
c (mol/cm^3)	1.06×10^{-5}	2.17×10^{-2}	-4.34×10^{-2}	-

d. T = 0°C

$$P(r) = k_0 + k_1 r + k_2 r^2 + k_3 r^3 + k_4 r^4$$

$P(r)$	k_0	k_1	k_2	k_3
κ (S/cm)	-5.12×10^{-5}	5.19×10^{-2}	-0.840	3.63
ρ_+	0.175	-5.54	73.6	-288.4
D (cm^2/s)	4.90×10^{-7}	-1.28×10^{-6}	-5.15×10^{-5}	3.10×10^{-4}
$dU/dlnm$	-1.57×10^{-2}	-0.392	-6.02	-

e. T = -20°C

$$P(r) = k_0 + k_1 r + k_2 r^2 + k_3 r^3 + k_4 r^4$$

$P(r)$	k_0	k_1	k_2	k_3	k_4
κ (S/cm)	-5.53×10^{-5}	2.65×10^{-2}	-0.675	6.21	-19.89
ρ_+	0.115	-4.41	63.28	-239.8	-
D (cm^2/s)	3.09×10^{-7}	-8.18×10^{-6}	1.58×10^{-4}	-8.33×10^{-4}	-
$dU/dlnm$	-1.54×10^{-2}	-0.425	-6.92	-	-

Table S4.5 Fitting Parameters for Integrating Term, J_2, for Potential Profile Modeling.

a. Electrochemical Model

$$J_2 = k_0 + k_1 r + k_2 r^2 + k_3 r^3 + k_4 r^4 + k_5 r^5$$

T(°C)	k_0	k_1	k_2	k_3	k_4	k_5
45°C	-1.90×10^{-5}	4.67×10^{-3}	-0.173	2.86	-22.2	65.4
30°C	6.83×10^{-5}	-3.71×10^{-3}	0.113	-1.72	12.92	-37.53
15°C	6.05×10^{-5}	-3.12×10^{-7}	9.73×10^{-2}	-1.504	11.31	-32.8
0°C	5.34×10^{-5}	-8.14×10^{-4}	7.98×10^{-3}	-2.65×10^{-2}	-	-
-20°C	7.23×10^{-5}	-4.33×10^{-3}	0.140	-2.18	16.44	-47.77

b. Electrophoretic NMR Model

$$J_2 = k_0 + k_1 r + k_2 r^2 + k_3 r^3 + k_4 r^4 + k_5 r^5$$

T(°C)	k_0	k_1	k_2	k_3	k_4	k_5
45°C	1.98×10^{-4}	-0.014	0.493	-7.97	60.92	-177.9
30°C	2.50×10^{-5}	-2.23×10^{-3}	0.874	-15.0	115.4	-328
15°C	4.02×10^{-4}	-2.67×10^{-2}	0.925	-15.18	117.3	-345.5

4.7.2 Potential Versus Current Relationships

We plot relationships between current and voltage as shown in Figure 4.9b for two additional salt concentrations at 30°C. The similarity in Φ_{ss}/L predicted from both echem and eNMR modeling is true across the salt concentration and temperature range.

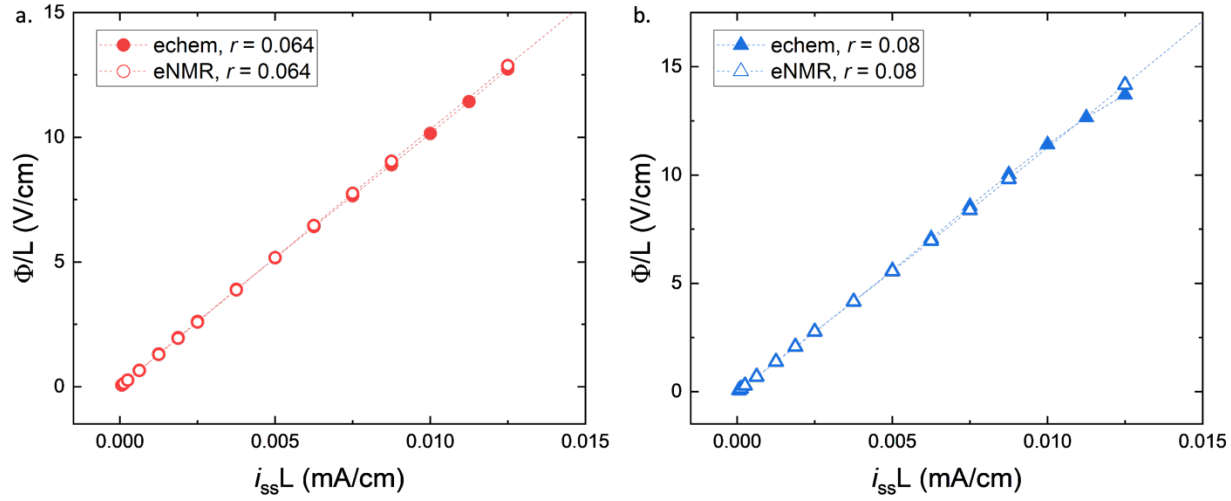

Figure S4.12. Magnitude of modeled potential gradient, shown for both echem and eNMR based modeling as a function of $i_{ss}L$ for T = 30°C for (a) r = 0.064 and b) r = 0.08.

4.8 Nomenclature

t_+^0	Cation transference number with respect to the solvent velocity
κ	Ionic conductivity (S cm^{-1})
T_f	Thermodynamic factor
D	Salt diffusion coefficient (cm^2 s^{-1})
ρ_+	Current fraction
$dU/dlnm$	Change in open circuit potential with respect to log of molality measured in a concentration cell experiment
r	Measure of ratio of lithium ions to oxygen atoms in solvent
m	Molality (mol kg^{-1})
c	Concentration of the salt (mol cm^{-3})
ΔV	Applied voltage (V)
I_{ss}	Steady-state current (mA)
R_i	Interfacial resistance (Ω)
Φ	Potential drop (V)
I_{ss}	Steady-state current (mA)
i_{ss}	Steady-state applied current density, used in concentration gradient modeling (mA cm^{-2})
D_s	Salt diffusion coefficient through the separator (cm^2 s^{-1})
t_-^0	Anion transference number with respect to the solvent velocity
L	Distance between electrodes, used in concentration gradient modeling
x/L	Dimensionless position across the electrolyte, used in concentration gradient modeling
F	Faraday's constant (C mol^{-1})
z_-	Anion charge number
ν_-	Number of anions the salt dissolves into

τ	Tortuosity of separator
r_{av}	Average concentration of the electrolyte, used in concentration gradient modeling
Φ_{ss}	Potential of the positive electrode relative to the negative electrode during steady-state polarization (V)
κ_s	Conductivity measured in an electrolyte soaked separator
φ_c	Volume fraction of conducting phase in separator
l	Thickness of the separator (cm)
R_s	Series resistance (Ω)
A	Area of electrodes (cm^2)
i_{limit}	Limiting Current (mA/cm^2)
Δr	Difference between the maximum salt concentration, at $x/L = 0$, and the minimum salt concentration, at $x/L = 1$

5 Impact of Chain Length on Ion Transport in Oligoether-Based Electrolytes Containing Lithium Salt

5.1 Abstract

Glyme-based electrolytes have been studied for various battery technologies due to their stability and nonflammability compared to conventional carbonate electrolytes used in lithium-ion batteries. Glyme solvents span from monoglyme to the most well characterized polymer electrolyte, poly(ethylene oxide). These solvents all have the same chemical structure of $CH_3O[CH_2CH_2O]_nCH_3$, but the n number of repeat units, as well as salt concentration, can drastically impact transport properties. Increasing chain length of the solvent increases solvent viscosity and impacts the mechanism of ion conduction. In this work, we study three glyme-based liquid electrolytes with varying chain lengths – tetraglyme, pentaglyme, and octaglyme – as a function of salt concentration. We fully characterize these electrolytes in terms of measured transport and thermodynamic properties – including ionic conductivity, salt diffusion coefficient, cation transference number, and the thermodynamic factor. Chain length has a very strong impact on properties describing total ion movement, including conductivity, salt diffusion coefficient, and species' velocities. These changes are not fully explained by the increase in neat solvent viscosity. Transference numbers determined using electrophoretic NMR show the same nonmonotonic dependence on salt concentration across all three electrolytes. Each solvent has a characteristic minimum that is well explained by the expected solvation motifs from molecular dynamic simulations.

5.2 Introduction

Oligoether glyme-based solvents have been widely studied for their potential as liquid electrolytes in various battery technologies due to their stability and nonflammability compared to conventional carbonate electrolytes.[15] Depending on the size of the solvent molecule, salt concentration, and temperature, the mechanism of solvation and ion-ion interactions can vary greatly.[16–18] All glymes strongly solvate lithium cations due to electronegative oxygens on the solvent backbone. The mechanism of ion transport in various glyme solvents has been the focus of many modeling studies.[19–23] The longest glyme solvent, poly(ethylene oxide), or PEO, conducts ions via an ion-hopping mechanism due to the interconnectivity of polymer chains.[20,21,23] Liquid glyme solvents tend to conduct ions via a vehicular mechanism.[19] Due to the differences in mechanism of ion conduction, the residence time of solvation also varies greatly with chain length. Because of this, chain length will drastically impact transport properties and the overall utility of a given electrolyte.

In Newman's concentrated solution theory, ion transport is fully described by three transport parameters – ionic conductivity, κ, salt diffusion coefficient, D, transference number, t_+^0 – and a thermodynamic factor, T_f.[5] To study the impact of chain length on transport properties, we study three electrolyte systems containing oligoether glyme solvents. We are specifically interested in studying higher molecular weight glymes, as they are not well characterized in the literature compared to low molecular weight liquids or PEO. Some comparative studies on smaller glymes, such as monoglyme, diglyme, triglyme, and tetraglyme, already exist.[16,17,24] A glyme-based solvent has the molecular structure of $CH_3O[CH_2CH_2O]_nCH_3$. The first solvent studied in this work is tetraethylene glycol dimethyl ether, or tetraglyme (molecular weight, MW = 222.28

g/mol), which has four CH_2CH_2O repeat units. Tetraglyme has previously been widely studied as a function of both salt concentration and temperature.[27,29,47,125,126] The second solvent is pentaethylene glycol dimethyl ether, or pentaglyme (MW = 266.33 g/mol), which contains five repeat units. The third solvent is octaethylene glycol dimethyl ether, or octaglyme (MW = 398.47 g/mol), which has 8 repeat units. In all of these systems, there is an additional oxygen outside of the repeat group which also participates in lithium solvation according to molecular dynamic simulations.[22,58]

In this work, we have characterized tetraglyme, pentaglyme, and octaglyme electrolytes containing lithium bis(trifluoromethanesulfonyl)imide (LiTFSI) salt as a function of salt concentration. We use a methodology that combines electrochemical measurements,[6,8,37,62] including ac impedance spectroscopy, restricted diffusion, polarization experiments, and concentration cells, with electrophoretic NMR (eNMR).[58] eNMR is a technique that enables the precise determination of the cation transference number, independent of other electrochemical experiments, by directly measuring electric-field-induced cation, anion, and solvent velocities.[10,12,13,122,124] Combining electrochemical techniques with eNMR significantly reduces uncertainty in both t_+^0 and T_f.[89] Using this methodology, we are able to discern the changes to transport as chain length increases from four to eight. The impact of chain length on bulk transport properties is discussed, along with insights into the relationship between cation solvation and the cation transference number.

5.3 Experimental

5.3.1 Electrolyte Preparation

All electrolytes were prepared using lithium bis(trifluoromethanesulfonyl)imide (LiTFSI) salt. LiTFSI (Sigma-Aldrich) was dried in a glovebox antechamber for three days under active vacuum at 100°C. Tetraethylene glycol dimethyl ether (tetraglyme) was purchased from Sigma-Aldrich and dried under active vacuum at 60°C for three days. Pentaethylene glycol dimethyl ether (pentaglyme) and octaethylene glycol dimethyl ether (octaglyme) were synthesized by methylation synthesis from glycol precursors, pentaethylene glycol and octaethylene glycol, using sodium hydride and methyl iodide. Additional details can be found in the Supplemental Information. Glycol solvents were obtained from Sigma-Aldrich and used as received. The purified and isolated pentaglyme and octaglyme was dried in a glovebox antechamber at 60°C under active vacuum for three days.

All electrolytes were prepared in an argon glovebox with oxygen and water levels less than 1 ppm. Electrolytes were made by dissolving a known mass of salt in a given mass of solvent and stirring overnight. Tetraglyme electrolytes were stirred at room temperature and pentaglyme and octaglyme electrolytes were stirred at 50°C. The primary unit of salt concentration used in this study, r, describes the ratio of lithium cations in LiTFSI to ether oxygens in the solvent, r = ([Li^+]/[O]). r is a useful unit of concentration for ether or glyme-based electrolytes as oxygens in the solvent strongly interact with the cation and the nature of cation solvation can influence transport properties. The concentrations of all electrolytes used within this study are given in Table S5.1, along with their concentrations in molality, m (mol/kg).

5.3.2 Viscosity

Viscosity (η) for each solvent was measured using an electromagnetically spinning viscometer (Kyoto Electronics). Viscosity for each solvent at 30°C is shown in Figure 5.1. We report viscosity for tetraglyme and pentaglyme between 0 and 100°C and for octaglyme between 30 and 60°C in Table S5.2.

5.3.3 Conductivity

Conductivity was measured in blocking electrode symmetric cells assembled in CR2032 coin cell parts (MTI Corp.). Five layers of Celgard 2500 separators were soaked in a given electrolyte and sandwiched between two stainless steel blocking electrodes (MTI Corp.), 500 mm thick and 15.5 mm in diameter. The pentaglyme and octaglyme electrolytes were heated before assembly to lower viscosity and improve wetting of the separators. Three cells were made for each salt concentration and solvent type. Cells were cycled in an environmental chamber at 30°C, and the temperature was confirmed using a thermocouple. A Biologic VMP300 potentiostat was used to perform ac impedance spectroscopy over a frequency range of 1 MHz to 100 mHz with a sinus amplitude of 5 mV. R_s, the series resistance value, was obtained from the impedance spectra and relates to the conductivity of the electrolyte according to equation 5.1.[53]

$$\kappa = \frac{\tau}{\varphi_c}\frac{l}{R_s A}, \tag{5.1}$$

Here, τ corrects for the tortuosity of the separator, φ_c corrects for the volume fraction of the conducting phase, l is the thickness of the electrolyte soaked separator, and A is the surface area of the stainless steel electrodes. The tortuosity of the separator is 2.93 and the volume fraction is equivalent to the porosity, 0.55.[89]

5.3.4 Current Fraction and Restricted Diffusion

Current fraction[7] and diffusion coefficient were measured in lithium-LiTFSI/tetraglyme-lithium symmetric cells assembled in CR2032 coin cell parts (MTI Corp.) For tetraglyme-based electrolytes, five, ten, or fifteen layers of electrolyte soaked Celgard 2500 separators were used. Only five separator cells were assembled for pentaglyme and octaglyme-based electrolytes. Like with conductivity cells, pentaglyme and octaglyme electrolytes were heated to improve wetting of the Celgard. Soaked separators were sandwiched between lithium chips (MTI Corp), 600 mm thick and 14 mm in diameter. Cells were made in triplicate for each salt concentration, solvent type, and thickness, when relevant. An environmental chamber (JEIO Tech) was used to cycle the cells and maintain a temperature setpoint of 30°C. The temperature was confirmed using a thermocouple.

To stabilize the interface between the lithium metal electrodes and electrolyte, cells were preconditioned using alternating current densities of $\pm$0.02 mA/cm^2 applied for four hours. A one hour rest occurred between polarizations. Preconditioning cycles continued until the interfacial resistance, R_i, was stable. The current fraction, ρ_+, was measured in accordance with the Bruce-Vincent method.[41–43] Cells were polarized at ΔV = 10 mV, -10 mV, 20 mV, and -20 mV for one hour to ensure the measured current fraction was independent of the magnitude and sign of the applied potential. The current fraction can be calculated using equation 5.2.

$$\rho_+ = \frac{I_{ss}}{I_\Omega}\left(\frac{\Delta V - I_\Omega R_{i,0}}{\Delta V - I_{ss}R_{i,ss}}\right). \quad (5.2)$$

Here, I_{ss}, is the steady-state current measured during polarization. I_Ω, the initial current at the first instance of polarization, is determined using Ohm's law, assuming concentration gradients have not yet formed. $R_{i,0}$ and $R_{i,ss}$ are the initial and steady-state interfacial resistances in the cell, respectively, taken from impedance measurements before, during, and after polarization.

After polarization, the applied potential was removed and the open circuit potential, U, was measured. Cells assembled with five Celgards were allowed to relax for one hour and the first 15 minutes of relaxation were used to determine the diffusion coefficient using the method of restricted diffusion.[54] U was fit to an exponential function, $U(t) = k_0 + ae^{-bt}$, where k_0 is an offset voltage and a and b are fitting parameters. The exponential fit coefficient, b, is related to the diffusion coefficient through the separator, D_s by $D_s = (l^2 b)/\pi^2$. A minimum time cutoff, α, is used such that $\alpha = (D_s\, t)/l^2 > 0.03$.[55] The salt diffusion coefficient, D, is related to D_s by the tortuosity of the separator, $D = \tau D_s$.

5.3.5 Concentration Cells

Pouch-based concentration cells[40] were assembled following the work done by Landesfeind et al.[37] A 1 cm wide, 10 cm long, and 25 μm thick Celgard 2500 separator was placed in a pouch cell (5 cm wide, 13 cm long) and wet with electrolyte. The long separator prevents mixing of the electrolyte during the measurement period. One side of the separator was wet with a reference electrolyte, which varied across the different solvents. The other side was wet with a test electrolyte. ~8 μL of electrolyte were used to wet each side. Any excess electrolyte was removed using a Kimwipe, as excess electrolyte could cause convection and accelerate mixing or interfere with sealing. The separator was placed on top of lithium foil electrodes (MTI Corp.), which were connected to nickel tabs. The assembled pouch cell was then sealed under argon. Pouch cells were placed in a metal press in an environmental chamber (JEIO Tech) to maintain temperature during the measurement. The open circuit potential for each concentration cell, U, was taken as the average value over 10 minutes after the potential stabilized. At least two pouch cells were made for each salt concentration and solvent type.

5.3.6 Electrophoretic NMR

Electrophoretic NMR (eNMR) methods of experimentation have been described in several other works.[92–94] eNMR data for tetraglyme using this procedure has been previously reported.[123] Pentaglyme and octaglyme-based electrolyte samples were prepared by filling a dried eNMR cell with electrolyte in an argon glovebox, with oxygen and water levels maintained below 1 ppm. Details of experimental procedures, instrumentation, and calibration have been previously reported.[58,90] ^{7}Li, ^{19}F, and ^{1}H NMR measurements were used to determine cation, anion, and solvent velocities, respectively. Tetraglyme experiments were previously conducted at 45, 30, and 15°C, ± 1°C. Pentaglyme experiments were conducted at 30°C. Octaglyme experiments were conducted at 60°C.

5.4 Results and Discussion

In Figure 5.1, we plot viscosity, η, of various glyme solvents, including tetraglyme (TG), pentaglyme (PG), and octaglyme (OG) as a function of chain length at 30°C. One chain is defined as one [OCH_2CH_2] repeat unit, n: in TG, n = 4, in PG, n = 5, and in OG, n = 8. All of these solvents have an additional oxygen that is not contained within one of the repeat units, but molecular dynamic (MD) simulations on tetraglyme indicate all oxygens participate in solvation of the cation.[22,58] In this figure, we also show viscosity data for smaller glyme solvents, including diglyme and triglyme, taken from Carvalho et al.[127] As noted by these authors and confirmed with our data, the viscosity of glyme solvents depends exponentially on chain length. We see a steep increase in measured viscosity with increased chain length so that the viscosity of OG is over double that of PG, which is over double the viscosity of TG at 30°C. Solvent viscosity has a significant impact on many transport properties, especially the conductivity. From the solvent viscosity alone, it is evident that adding even one repeat unit in liquid electrolytes will likely impact ion transport.

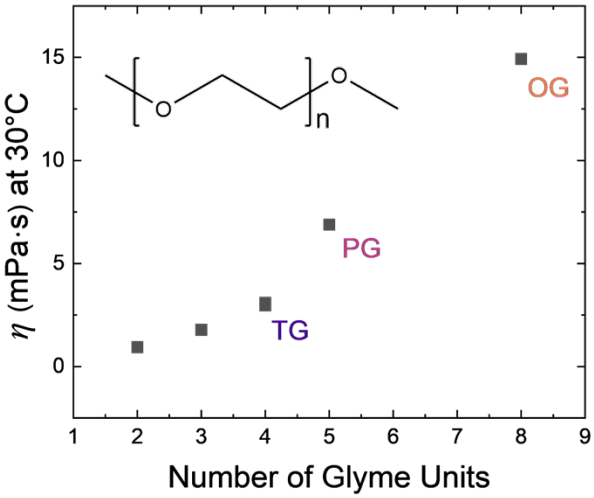

Figure 5.1. Viscosity of various glyme-based solvents, where the number of glyme units corresponds to the n number of repeat units in the molecule. Tetraglyme (TG), for example, has four repeat units. Data for diglyme (n = 2) and triglyme (n = 3) is taken from Carvalho et al.[127]

In Figure 5.2a, we report the measured ionic conductivities, κ, for each type of electrolyte – TG, PG, and OG – as a function of salt concentration, r. Conductivity depends strongly on both salt concentration and chain length of the solvent. κ has a nonmonotonic dependence on r, but this is most pronounced in tetraglyme and less pronounced in octaglyme. κ increases at low concentrations due to an increase in the number of charge carriers, peaks, and then decreases at high concentrations due to frictional effects. κ has an even stronger dependence on chain length compared to salt concentration. Pentaglyme is about half as conductive as tetraglyme for the same salt concentration. Adding one single repeat unit drastically lowers the measured conductivity. This trend continues with octaglyme, which is about one-third as conductive as tetraglyme. Given how strongly viscosity changes with increasing chain length, we plot conductivity multiplied by viscosity of the neat solvent, $\kappa\eta_0$, as a function of salt concentration for TG, PG, and OG in Figure

5.2b. Interestingly, the solvent viscosity overcorrects for the changes in conductivity. $\kappa\eta_0$ is highest for octaglyme, then pentaglyme, then tetraglyme. If viscosity alone explained the reduction in conductivity with increasing chain length, we would expect $\kappa\eta_0$ to be independent of chain length.

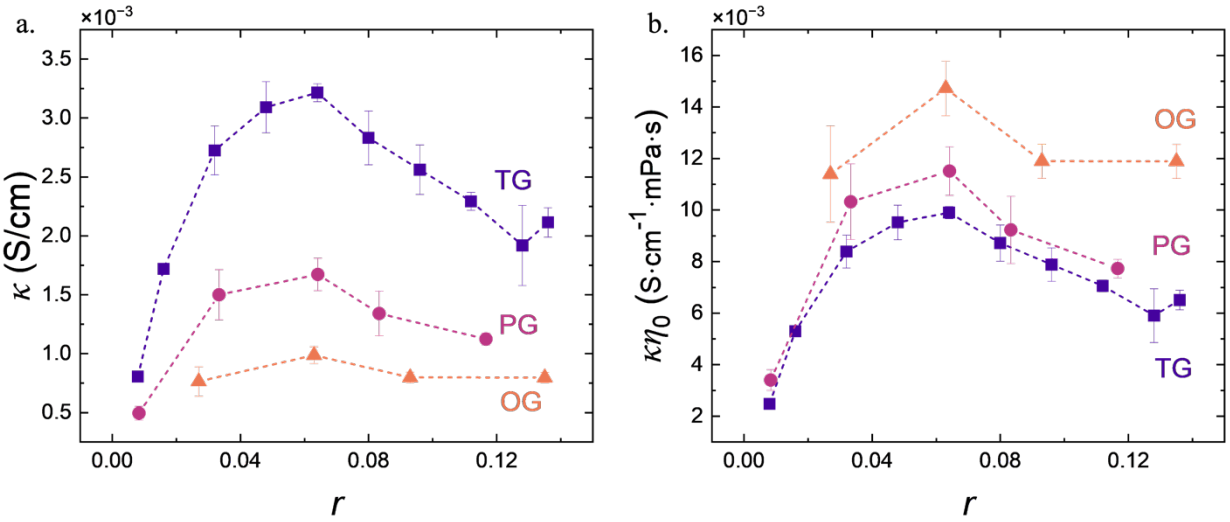

Figure 5.2. a) Conductivity for tetraglyme (TG), pentaglyme (PG), and octaglyme (OG), shown as a function of salt concentration, r, at 30°C. b) Conductivity multiplied by the viscosity of the neat solvent, $\kappa\eta_0$, shown as a function of r for TG, PG, and OG.

In Figure 5.3, we plot current fraction, ρ_+, as a function of salt concentration for TG, PG, and OG. The current fraction decreases slightly with increasing r for tetraglyme and octaglyme. This is also generally true for pentaglyme, but there is some nonmonotonic dependence on salt concentration between r = 0.033 and 0.083. ρ_+ does not have a strong dependence on chain length. Although the current fraction measured for octaglyme is lower than tetraglyme across all salt concentrations, pentaglyme is higher than in tetraglyme at some salt concentrations and lower than in octaglyme at other concentrations. The large error associated with ρ_+ also makes it difficult to discern trends, especially considering ρ_+ is small, less than 0.20 for most of the salt concentration range across all three solvents.

In Figure 5.4a, we plot the salt diffusion coefficient, D, as a function of r for TG, PG, and OG. D is highest for tetraglyme and then decreases with increasing chain length. D also decreases with increasing salt concentration, but less substantially. In Figure 5.4b, we plot $D\eta_0$, the salt diffusion coefficient multiplied by the neat solvent viscosity. This is analogous to the $\kappa\eta_0$, plotted in Figure 5.2b. Diffusion of ions is strongly impacted by solvent viscosity, but it is also affected by thermodynamics. We see a similar result in Figure 5.4b as in Figure 5.2b. $D\eta_0$ is highest for the largest solvent molecule, octaglyme, and decreases with decreasing chain length. Again, accounting for the effect of solvent viscosity on salt diffusion coefficient overcorrects for increasing chain length. This indicates there may be additional effects impacting ion transport, which may include changes to thermodynamics or changes to the mechanism of ion conduction and diffusion with increasing chain length. Additional information about the effect of salt concentration on viscosity could elucidate this trend.

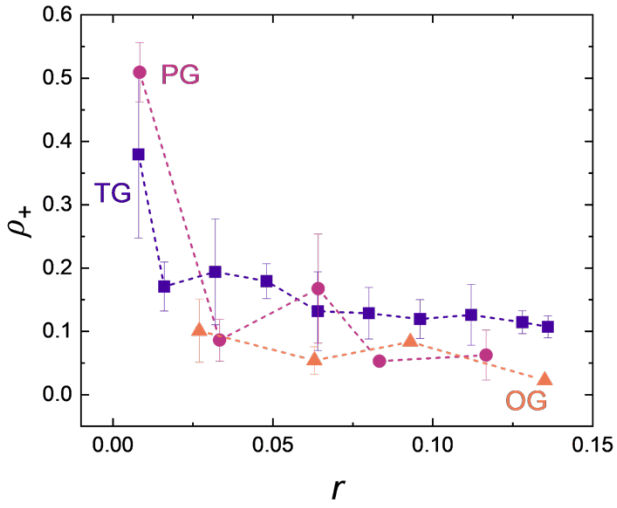

Figure 5.3. Current fraction, ρ_+, measured in a Bruce-Vincent experiment and shown as a function of salt concentration, r, for TG, PG, and OG.

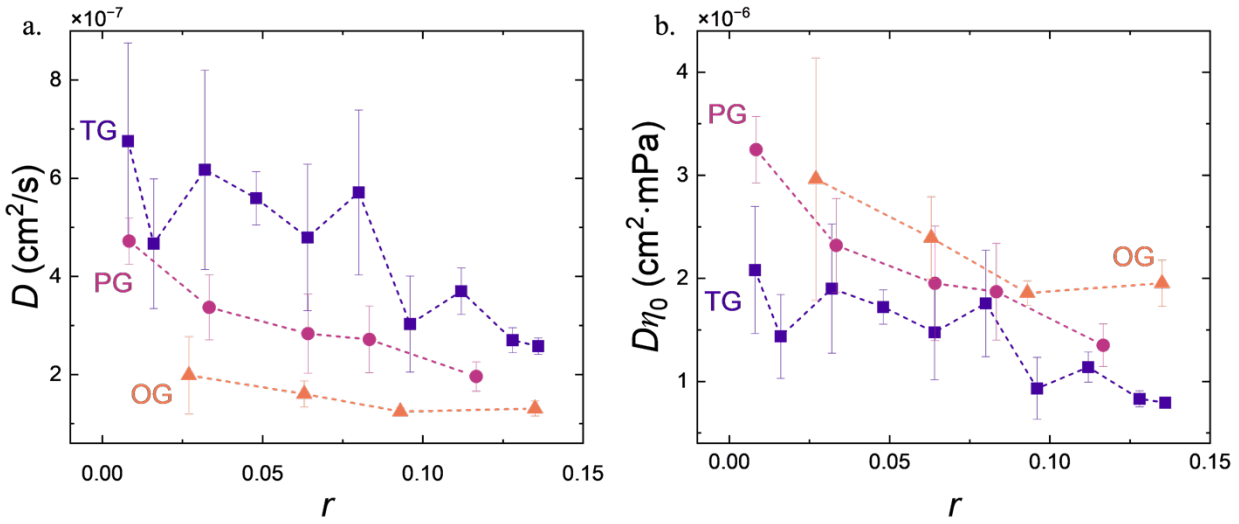

Figure 5.4. Diffusion coefficient, D, measured via restricted diffusion and a) plotted as a function of salt concentration, r, for TG, PG, and OG. b) D multiplied by the neat solvent viscosity, η_0, and shown as a function of r for TG, PG, and OG.

We report results from the final electrochemical experiment, concentration cells, in Figure 5.5. Figure 5.5a plots the open circuit potential, U, as a function of $\ln(m)$. The measured open circuit potential is very similar across electrolytes of all three solvents. U is nearly identical for tetraglyme and pentaglyme. U measured for octaglyme is very similar at low concentrations but deviates slightly at high concentrations. The relative similarity across the three solvents is not surprising given the similarity in U measured in PEO,[6,128] which has the same chemical structure as the glyme solvents but a much higher number of repeat units. We also plot $dU/dlnm$ in Figure 5.5b. $dU/dlnm$ is calculated using a finite difference method as previously described.[89] $dU/dlnm$ does

not seem to depend strongly on chain length. There are only slight deviations between octaglyme and tetraglyme or pentaglyme at high concentrations.

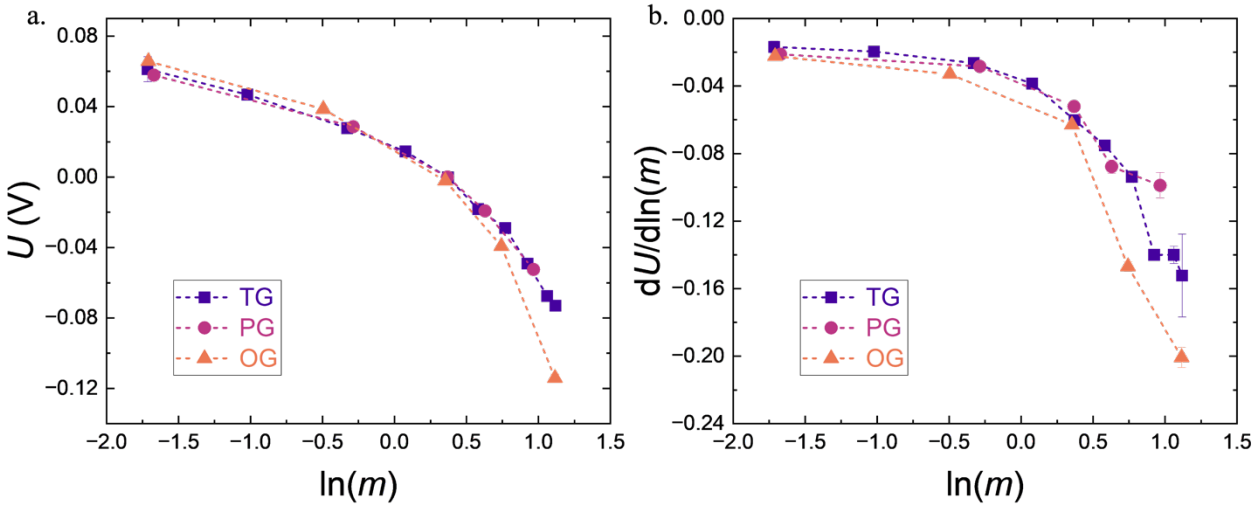

Figure 5.5. Concentration cell data for TG, PG, and OG, including a) measured open circuit potential, U, versus $ln(m)$ and b) the slope, $dU/dln(m)$, as a function of $ln(m)$, determined from a finite difference method.

So far, we have reported electrochemical properties that are averaged over all species in an electrolyte, including the cation, anion, solvent. This includes any ion-ion or ion-solvent interactions. Through eNMR, we can study the effect of chain length on the cation, anion, and solvent velocities. These contributions can't be fully separated as all species may interact with each other. In Figure 5.6, we plot velocities in the laboratory frame of reference measured via eNMR for two of the solvents, TG and OG, as a function of salt concentration. Velocities are defined as positive for species moving in the direction of the negative electrode. Octaglyme velocities were measured at 60°C and tetraglyme velocities were measured at 15, 30, and 45°C as previously reported. We plot all three temperatures for TG in Figure 5.6 to give an indication of trends with temperature. In Figure 5.6a, we plot the cation velocity, v_+. Velocities depends on temperature and we see an increase in v_+ with increasing temperature. In Figure 5.6b, we plot the anion velocity, v_-. v_- similarly increases in magnitude with increasing temperature. Like κ and D, which measure ion movement in response to migration or diffusion, ions move slower at lower temperatures due to increasing viscosity. In the absence of a direct comparison between octaglyme and tetraglyme velocities measured at the same temperature, we can generally see the cation and the anion of LiTFSI move much faster in tetraglyme compared to octaglyme. v_+ and v_- measured in octaglyme at 60°C are comparable in magnitude to v_+ and v_- measured in tetraglyme at 15°C.

In Figure 5.6c, we plot the solvent velocity, v_0. The solvent has a nonzero velocity because of electroosmotic drag by the cation and is therefore influenced strongly by the solvation structure. The solvation structure of the cation may be influenced by the type of solvent, salt concentration, and temperature. The solvent velocity in tetraglyme increases with increasing temperature, but at $r = 0.08$, v_0 is higher at 30°C than at 45°C. This indicates there are changes to solvation influencing how the solvent is dragged occurring at this salt concentration over this temperature range. v_0 for octaglyme also seems to be slower than in tetraglyme. Across both solvents, v_0 has a

nonmonotonic dependence on r and peaks somewhere in the intermediate concentration range. This is dissimilar from v_+ and v_-, which both decrease with increasing r due to frictional effects.

In Figure 5.6d, we plot the ratio of the solvent velocity to the cation velocity, v_0/v_+. We draw a line at $v_0/v_+ = 1$. Above the line, the solvent travels faster than the cation. Although the solvent needs to be dragged by the cation to have a positive velocity, the solvent can appear to travel faster than the cation because eNMR measures species' velocities averaged over all speciation states. These states can includes positively charged clusters, negatively charged clusters, and neutral clusters.[6,22,66,129] One example way in which the solvent can appear to be traveling faster than the cation is if the majority of cations exist in negatively charged clusters (thus migrating in the "wrong" direction) but the majority of solvent molecules exist in positively charged clusters traveling in the "right" direction. Only at three points in Figure 5.6d is the solvent velocity faster than the cation: for TG at $r = 0.08$ and at $r = 0.24$ at 30°C and OG at $r = 0.093$ at 60°C. Pentaglyme, although not included in Figure 5.6 for clarity, also has a solvent velocity faster than the cation at $r = 0.16$.

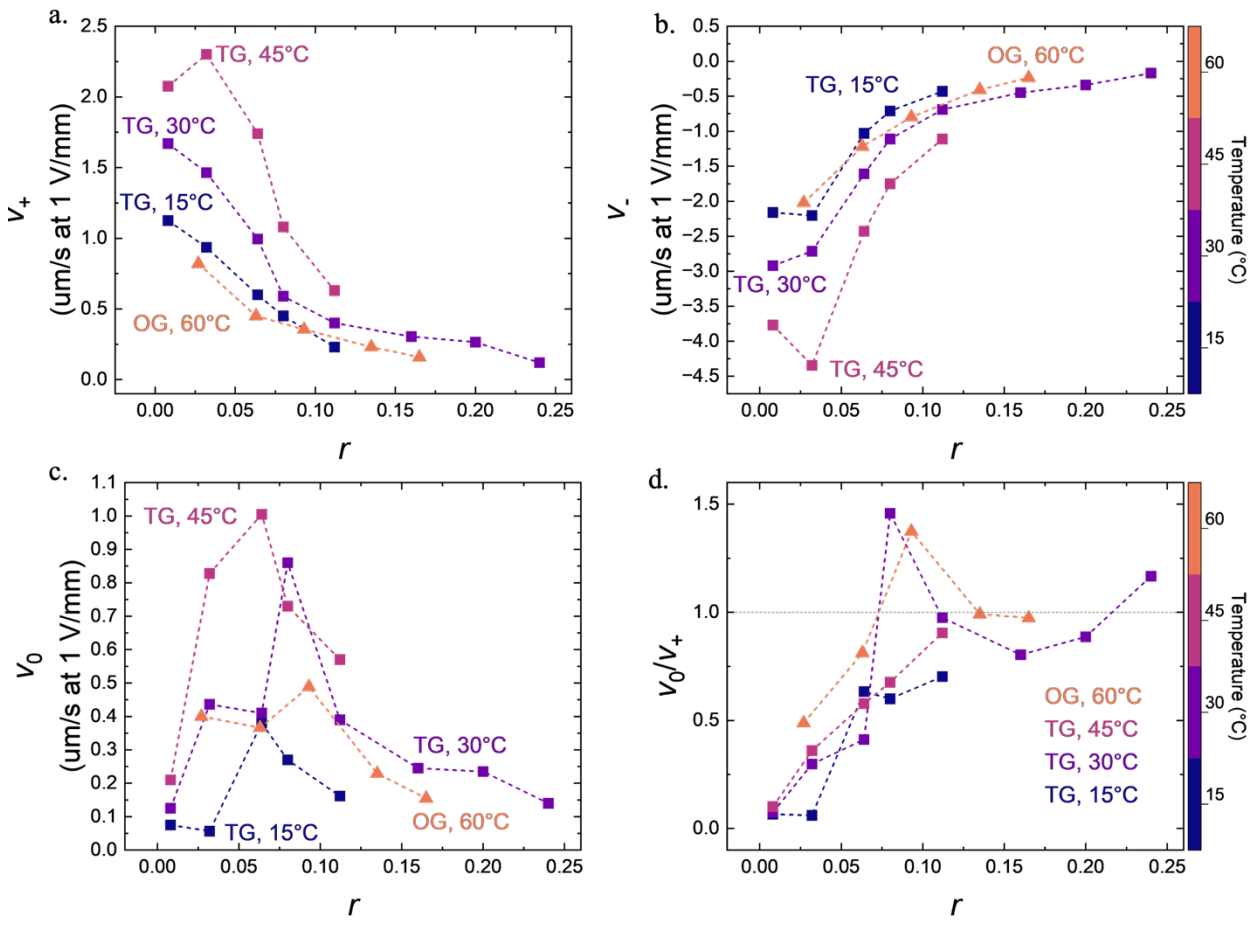

Figure 5.6. A comparison between species' velocities measured via eNMR for TG at 45, 30, and 15°C and OG at 60°C for a) cation, v_+, b) anion, v_-, c) solvent, v_0, and d) the ratio v_0/v_+. TG data was previously published by Hickson et al.[123]

Looking only at the TG data, we can see that v_0/v_+ does not have a clear dependence on temperature. v_0/v_+ is approximately the same across all temperatures except for at $r = 0.08$, where v_0/v_+ peaks at ~1.5. For this same salt concentration at 15 and 45°C, v_0/v_+ is less than 1. This change likely reflects changes in speciation states with changing temperature. Various reasons have been cited for the reason temperature impacts ion association; for example, temperature impacts the thermal energy associated with ion motion. The solvent dielectric constant, impacting how well ions dissociates, is also temperature dependent.[79,85] We also use the tetraglyme velocities at 15, 30, and 45°C to extrapolate expected velocities at 60°C. These approximations for the velocity are shown in Figure S5.13. and are plotted with OG velocities at 60°C. Qualitatively, the same conclusions can be drawn for the extrapolated data. Cation, anion, and solvent velocities are all expected to be faster in TG at 60°C compared to OG. However, the ratio of v_0/v_+ is approximately equal to TG or higher for OG at all salt concentrations.

The cation transference number with respect to the solvent velocity, t_+^0, can be determined directly from velocities measured via eNMR using equation 5.3:

$$t_+^0 = \frac{v_+ - v_0}{v_+ - v_-}. \tag{5.3}$$

In Figure 5.7, we plot t_+^0 as a function of salt concentration for TG, PG, and OG. The data for TG and PG was taken at 30°C and OG at 60°C. All three types of electrolytes show the same characteristic dependence on salt concentration. In the low concentration regime, t_+^0 decreases with increasing salt concentration. A minimum is reached, and then t_+^0 increases with increasing salt concentration. In tetraglyme, we see a secondary decrease past $r = 0.16$. This "V shaped" trend in the transference number seems to be characteristic to glyme solvents and also occurs for the polymer equivalent, PEO.[9,36,128] However, in all of the systems, the minimum occurs at different salt concentrations.

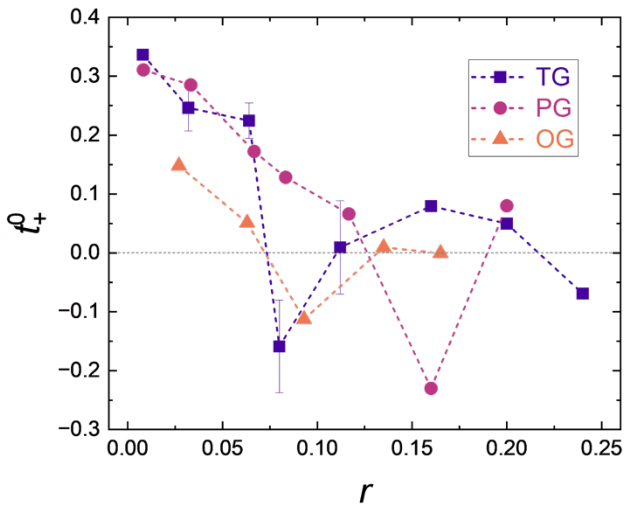

Figure 5.7. Cation transference number referenced to the solvent velocity, t_+^0, determined from eNMR and plotted as a function of salt concentration, r, for TG, PG, and OG. t_+^0 has been determined at 30°C for TG and PG and 60°C for OG.

We can generally define a critical salt concentration, r_c, which relates the number of lithium ions in LiTFSI to the number of oxygens that are involved in solvation based on the solvation motif. For example, MD simulations have indicated anywhere between four to seven oxygens are involved in the solvation of Li^+ in PEO.[20] Recent simulations indicate six oxygens are most common.[23] r_c then would be near 1 [Li^+]/ 6 [O], or r_c = 0.17. A minimum in t_+^0 near this salt concentration has been found experimentally in several works.[9,36,128] In tetraglyme, MD simulations found that a two-chain motif solvates Li^+ at low salt concentrations.[22,58] r_c would then be 1 [Li^+]/ 10 [O] or 0.10, which agrees well with the minimum seen at r = 0.08. We note this minimum is only seen at 30°C. MD simulations have not yet been conducted as a function of temperature for this system to understand changes in solvation with temperature. Preliminary octaglyme simulations indicate a 1-chain motif dominates at low salt concentrations, making r_c = 1 [Li^+]/ 9 [O], or 0.11, slightly higher than the minimum for TG. We qualitatively see this pattern in Figure 5.7. MD simulations by Borodin and Smith predicted one pentaglyme chain could solvate a lithium cation.[19,21] If 1-chain solvation is the primary solvation motif, then r_c = 1 [Li^+]/ 6 [O], or 0.17. This agrees very well with minimum seen for PG in Figure 5.7 at r = 0.16. The critical salt concentration occurs in each of the solvents with increasing salt concentration for TG, OG, and then PG. The number of oxygens involved in solvation is thus a good predictor for where the minimum in t_+^0 will occur, and in the absence of MD simulations, gives an indication of the method of solvation for each solvent.

Finally, the thermodynamic factor, T_f, can be determined using data from eNMR and concentration cells in accordance with equation 5.4.

$$T_f = 1 + \frac{dln\gamma_{+-}}{dlnm} = \frac{F}{2RT(1-t_+^0)}\frac{dU}{d\ln m} \tag{5.4}$$

γ_{+-} is the mean molal salt activity coefficient. In Figure 5.8, we plot T_f as a function of r for TG, PG, and OG. T_f here is determined using $dU/d\ln(m)$ from a finite difference method. The method of fitting somewhat impacts the magnitude of T_f, although it doesn't impact the qualitative trends. For completeness, we plot $dU/d\ln(m)$ determined from an exponential fit in Figure S5.14 and T_f calculated from that fit in Figure S5.15. T_f determined for pentaglyme and tetraglyme are very similar. For octaglyme, T_f is slightly higher in the high concentration range. For all three types of electrolytes, T_f should be equivalent to 1 in the dilute limit when the electrolyte is thermodynamically ideal. T_f then decreases to near 0.5 for all three electrolytes, and then increases with increasing salt concentration. As expected given ion-ion and ion-solvent interactions, the thermodynamic factor indicates all three solvents are nonideal.

Given the similarity in T_f shown in Figure 5.8, changing solvent chain length does not seem to have a strong thermodynamic effect. As discussed previously in Figures 5.2d and 5.4d, there are changes to the bulk transport properties, κ and D, with increasing chain length that are not easily explained by changes in the neat solvent viscosity. D is influenced by both viscosity and thermodynamics. However, the similarity in measured thermodynamic factor also seems to indicate that thermodynamics don't explain trends in κ or D with increasing chain length. Given the nonmonotonic trends in the solvent velocity and the transference number, it is likely that there are substantial differences in how lithium is solvated and transported in these three electrolyte

systems. Changes to the mechanism of ion conduction could explain why the $\kappa\eta_0$ and $D\eta_0$ increase with increasing chain length. Additional information about the influence of salt concentration on viscosity and additional MD simulations could elucidate trends in transport mechanisms with increasing chain length for these glyme-based electrolytes.

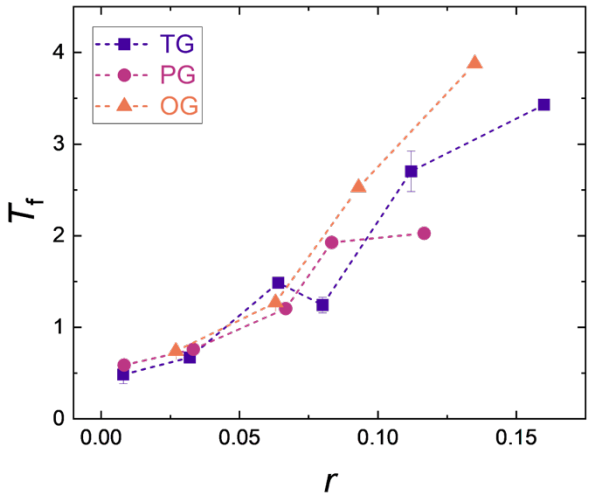

Figure 5.8. Thermodynamic factor, T_f, plotted as a function of salt concentration, r, for TG, PG, and OG. T_f was calculated using $dU/dln(m)$ determined from a finite difference method. Data used to calculate T_f for TG and PG was measured at 30°C and data used to calculate T_f for OG was measured at 60°C.

5.5 Conclusions

In this work, we have fully characterized three glyme-based liquid electrolytes with various solvent chain lengths. Chain length strongly impacts conductivity and salt diffusion coefficient, properties which reflect the total movement of ions via migration or diffusion. Increases in the solvent viscosity with increasing chain length do not fully explain reductions in conductivity and diffusion. Species' velocities measured via eNMR also decrease with increasing chain length. However, cation transference numbers determined using eNMR are similar in magnitude across all three glymes and all solvents have a characteristic "V shaped" dependence on salt concentration. We define a simple critical salt concentration, r_c, which is the inverse of the number of oxygens involved in the solvation of lithium cations. Based on solvation motifs predicted from molecular dynamic simulations, the critical salt concentration agrees well with experimental minimums in the transference number. Below this salt concentration, more solvent is available than salt. Above this salt concentration, more salt is available than solvent. The critical salt concentration reflects a transition in how the cation is solvated, and above this concentration, there is likely an increase in anion involvement in solvation. The differences in minimums in t_+^0 between the three solvents reflect three methods of cation solvation and ion movement.

5.6 Acknowledgements

This work was primarily supported by the Vehicle Technologies Office of the U.S. Department of Energy's Office of Energy Efficiency and Renewable Energy under the guidance of the Advanced

Battery Cell Research Program (eXtreme fast charge Cell Evaluation of Lithium-ion batteries, XCEL). We thank Dr Hasan Celik and UC Berkeley's NMR facility in the College of Chemistry (CoC-NMR) for spectroscopic assistance. The NMR instrument used in this work was supported by the National Science Foundation under grant no. 2018784.

Saheli Chakraborty is gratefully acknowledged for her necessary instruction and training of material synthesis. Rounak Jana is gratefully acknowledged for support and advising during synthesis. Quynh Nhi Dao made invaluable contributions to the electrochemical experimental work, both for data collection and analysis. Julia Im measured all reported electrophoretic NMR data with the support and mentorship of David M. Halat. D.M.H. and J.I. gratefully acknowledge support from the Pines Magnetic Resonance Center.

5.7 Supporting Information

5.7.1 Synthesis of Pentaglyme

Pentaethylene glycol was obtained from Sigma-Aldrich and used as received. 5g of pentaethylene glycol were added to a 100 mL round bottom flash and dissolved in 25 mL of anhydrous tetrahydrofuran (THF). The round bottom flash was brought into an argon glovebox, where 2.0 grams of sodium hydride were slowly added to the pentaethylene glycol/THF mixture while stirring. The reaction was stirred for 2 hours. After, the round bottom flash was capped with a rubber stopper and removed from the glovebox. 9.0 grams (~4 mL) of methyl iodide were then added, slowly while stirring. The reaction was left stirring overnight at room temperature. The reaction scheme is shown in Figure S5.9.

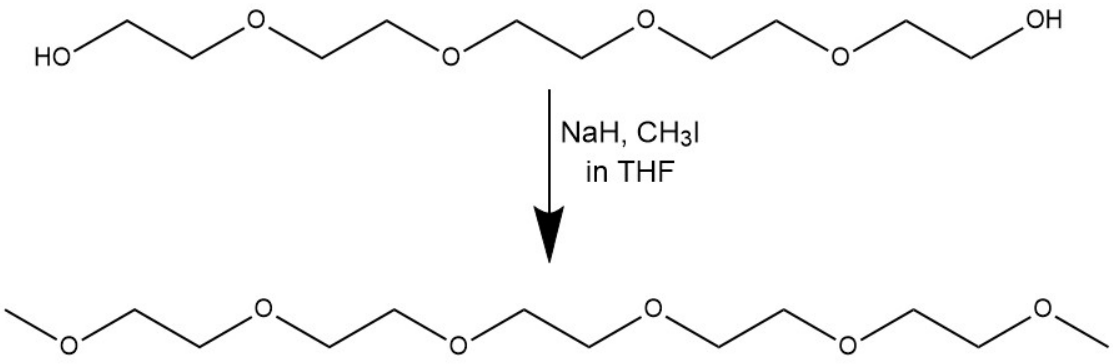

Figure S5.9. Reaction scheme for synthesis of pentaethylene glycol dimethyl ether (pentaglyme) from pentaethylene glycol using sodium hydride and methyl iodide.

5.7.2 Purification of Pentaglyme

10 mL of DI water was added to the round bottom flask. The THF was evaporated and an additional 10 mL of DI water was added to the residue. The pentaethylene glycol dimethyl ether (pentaglyme) was extracted using chloroform three times. The chloroform mixture was then dried using sodium sulfate salt and then the chloroform was evaporated. The product was dried in the fume hood overnight. The product was redissolved in chloroform and passed through aluminum oxide to

remove the orange color. The chloroform was then removed and the product was left to dry in the fume hood overnight. The compound was confirmed using ^{1}H NMR. (Figure S5.10). The octaglyme was then fully dried under active vacuum in a glovebox antechamber at 60°C for three days.

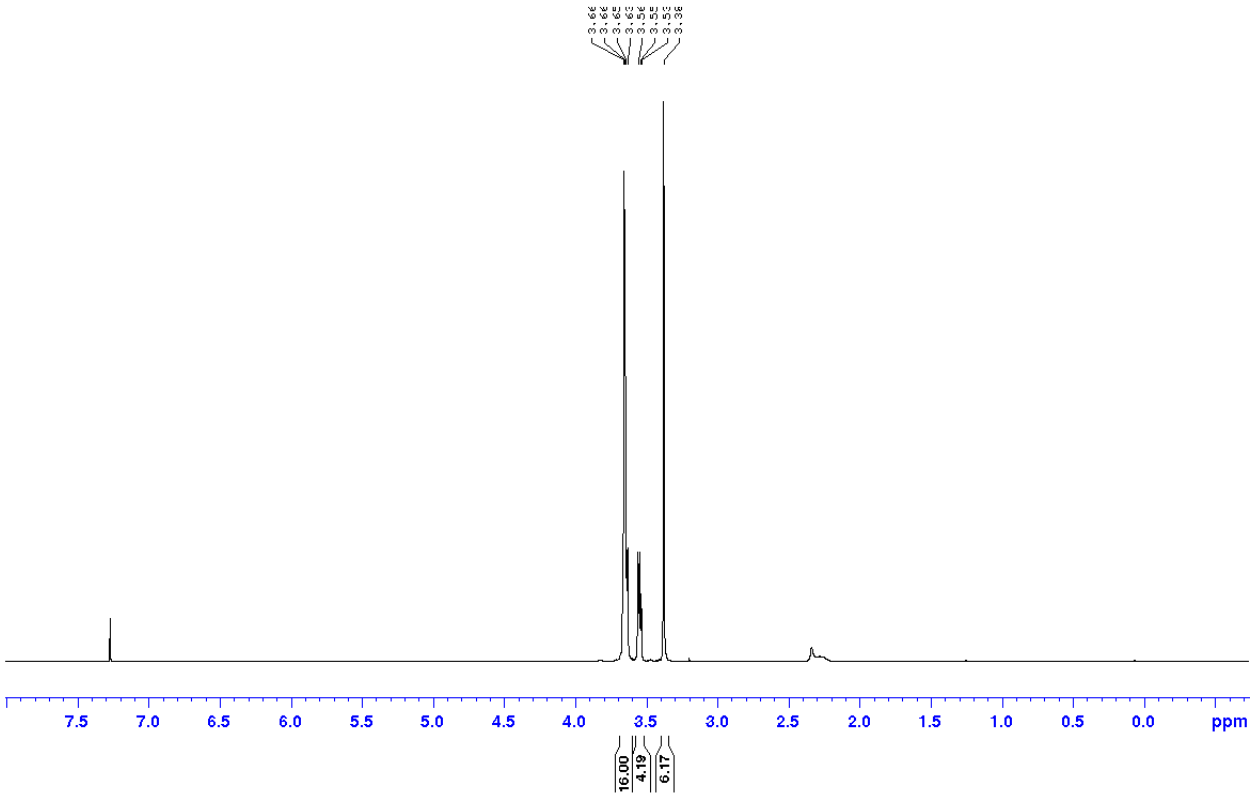

Figure S5.10. ^{1}H NMR spectra for synthesized pentaethylene glycol dimethyl ether. There are three main peaks in the spectra corresponding to the three chemical environments for protons in the pentaglyme molecule. Going left to right, the first peak corresponds to the 16 central backbone hydrogens, the second peak corresponds to the 4 backbone hydrogens closest to the ends of the chain, and the third peak corresponds to the 6 methyl hydrogens at the end of the molecule. This third peak needs to integrate to near 6 to indicate all of the terminal -H atoms have been replaced with $-CH_3$ groups.

5.7.3 Synthesis of Octaglyme

Octaethylene glycol was obtained from Sigma-Aldrich and used as received. 5g of octaethylene glycol were added to a 200 mL round bottom flash and dissolved in 50 mL of anhydrous tetrahydrofuran (THF). The round bottom flash was brought into an argon glovebox, where 1.3 grams of sodium hydride were slowly added to the octaethylene glycol/THF mixture while stirring. The reaction was stirred for 2 hours. After, the round bottom flash was capped with a rubber stopper and removed from the glovebox. 5.7 grams of methyl iodide (~2.5 mL) were then added, slowly while stirring. The reaction was left stirring overnight at room temperature. The reaction scheme is shown in Figure S5.11.

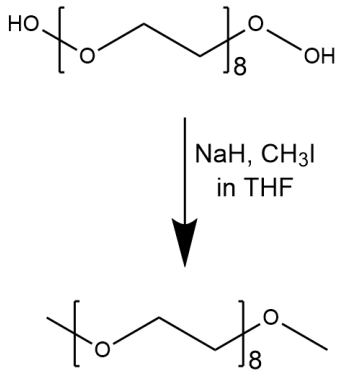

Figure S5.11. Reaction scheme for synthesis of octaethylene glycol dimethyl ether (octaglyme) from octaethylene glycol using sodium hydride and methyl iodide.

5.7.4 Purification of Octaglyme

10 mL of DI water was added to the round bottom flask. The THF was evaporated and an additional 10 mL of DI was added to the residue. The octaethylene glycol dimethyl ether (octaglyme) was extracted using chloroform three times. The chloroform mixture was then dried using sodium sulfate salt and then the chloroform was evaporated. The product was dried in the fume hood overnight. The product was redissolved in chloroform and passed through aluminum oxide to remove the orange color. The chloroform was then removed and the product was left to dry in the fume hood overnight. The compound was confirmed using ^{1}H NMR. (Figure S5.12). The octaglyme was then fully dried under active vacuum in a glovebox antechamber at 60°C for three days.

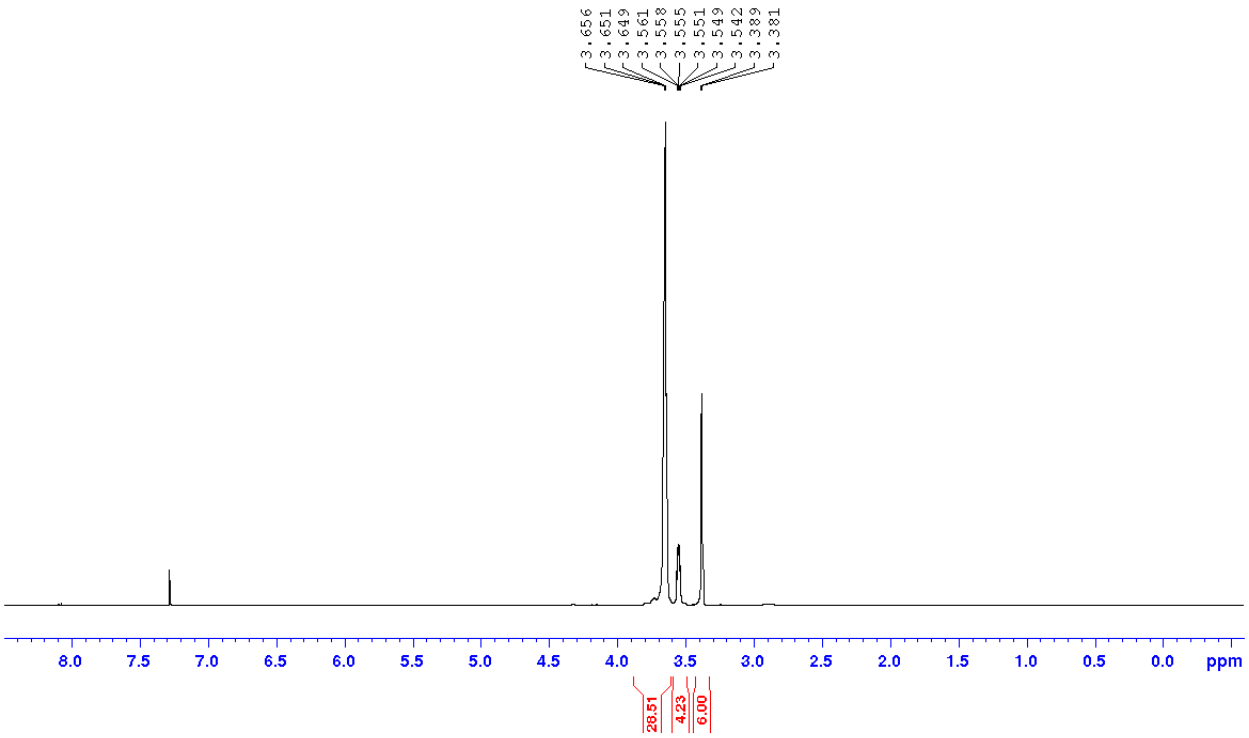

Figure S5.12. ^{1}H NMR spectra for synthesized octaethylene glycol dimethyl ether. There are three main peaks in the spectra corresponding to the three chemical environments for protons in the octaglyme molecule. Going left to right, the first peak corresponds to the 28 central backbone hydrogens, the second peak corresponds to the 4 backbone hydrogens closest to the ends of the chain, and the third peak corresponds to the 6 methyl hydrogens at the end of the molecule. This third peak needs to integrate to near 6 to indicate all of the terminal -H atoms have been replaced with -CH_3 groups.

5.7.5 Concentrations of LiTFSI/tetraglyme, LiTFSI/pentaglyme, and LiTFSI/octaglyme

Table S5.1. Salt concentrations tetraglyme, pentaglyme, and octaglyme electrolytes in units of r and molality, m.

Tetraglyme (TG)		Pentaglyme (PG)		Octaglyme (OG)	
r ([Li^+/O])	m (mol/kg)	r ([Li^+/O])	m (mol/kg)	r ([Li^+/O])	m (mol/kg)
0.008	0.18	0.0083	0.188	0.027	0.610
0.016	0.36	0.0333	0.751	0.063	1.424
0.032	0.72	0.0667	1.446	0.093	2.102
0.048	1.08	0.0833	1.877	0.135	3.052
0.064	1.45	0.1167	2.628	0.165	3.730
0.08	1.79	0.16	3.605		
0.096	2.16	0.20	4.506		
0.112	2.52				
0.128	2.89				

0.136	3.06
0.16	3.60
0.20	4.54
0.24	5.40

5.7.6 Viscosity for Neat Solvents as a Function of Temperature

Table S5.2**.** Viscosity for neat tetraglyme, pentaglyme, and octaglyme as a function of temperature.

Tetraglyme (TG)		Pentaglyme (PG)		Octaglyme (OG)	
T (°C)	η (mPa · s)	T (°C)	η (mPa · s)	T (°C)	η (mPa · s)
0	7.19±0.04	0	20.04±0.07	30	14.92±0.10
5	6.01±0.04	10	16.17±0.08	45	9.174±0.04
10	5.19±0.04	20	13.28±0.06	60	6.18±0.06
20	3.95±0.04	30	9.36±0.03		
30	3.08±0.00	40	6.88±0.00		
40	2.48±0.00	50	4.19±0.01		
50	2.05±0.00	60	3.31±0.01		
60	1.71±0.01	70	2.77±0.00		
70	1.46±0.01	80	2.38±0.02		
80	1.29±0.01	90	2.10±0.02		
90	1.15±0.01	100	1.88±0.01		
100	1.10±0.01				

5.7.7 Comparison of Octaglyme Velocities with Extrapolated Tetraglyme Velocities at 60°C

In this portion of the SI, we plot species' velocities measured using eNMR plotted as a function of salt concentration, r, for octaglyme (OG) and tetraglyme (TG) at 60°C for the a) cation, v_+, b) anion, v_-, c) solvent, v_0, and d) the ratio between v_0 and v_+. TG data is estimated by extrapolating previously published velocity data at 15, 30, and 45°C.

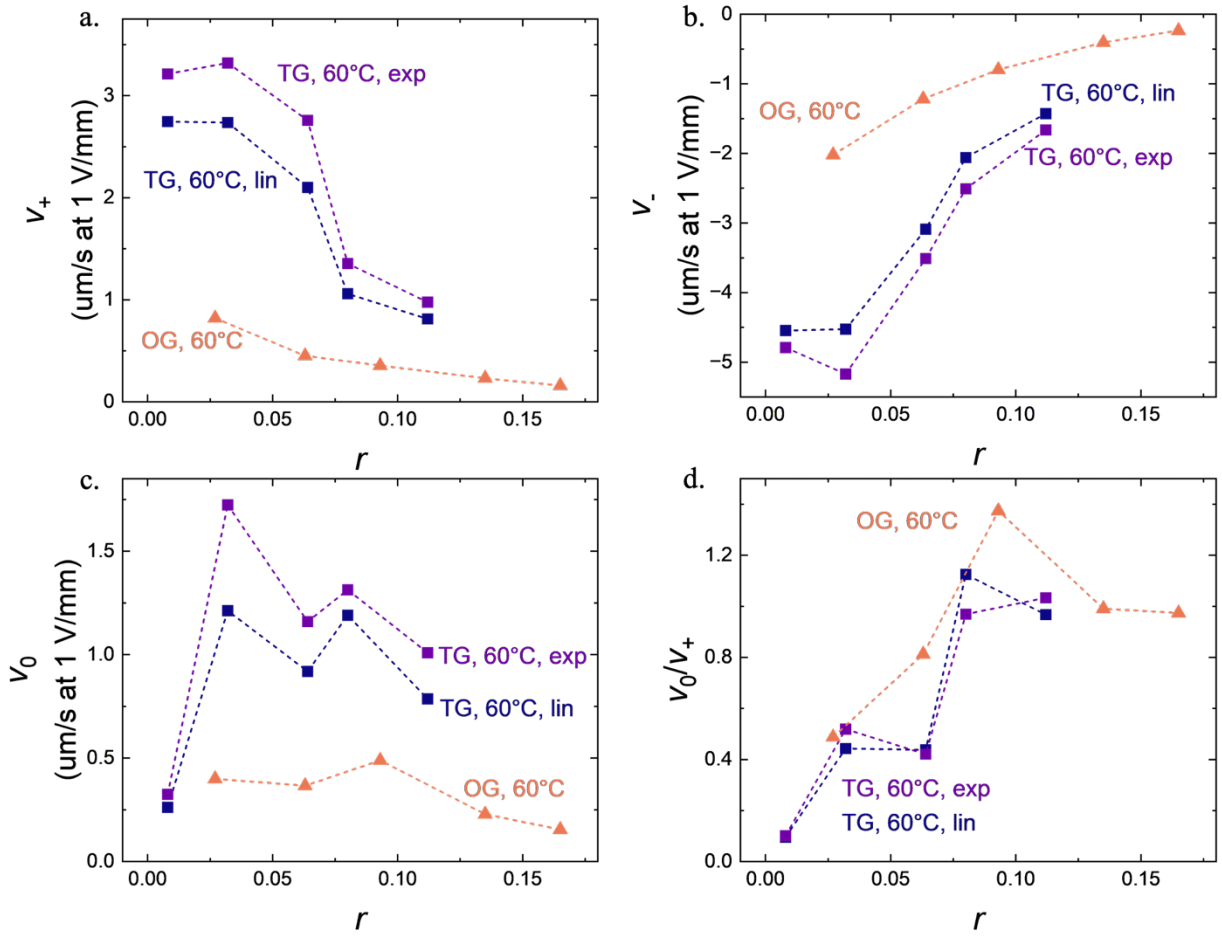

Figure S5.13. Species' velocities measured using eNMR plotted as a function of salt concentration, r, for octaglyme (OG) and tetraglyme (TG) at 60°C for a) cation, v_+, b) anion, v_-, c) solvent, v_0, and d) the ratio between v_0 and v_+. TG data is estimated by extrapolating previously published velocity data at 15, 30, and 45°C.

5.7.8 $\mathrm{d}U/\mathrm{d}ln\mathrm{m}$ Determined Using an Exponential Function and the Thermodynamic Factor

Fitting of concentration cell data can somewhat impact the quantitative values of $\mathrm{d}U/\mathrm{d}ln\mathrm{m}$ and the thermodynamic factor, T_f. For completeness, we show an additional method to fit the concentration cell data using an exponential function, $U = a - be^{c+d(lnm)}$. The values for $\mathrm{dU/d}ln\mathrm{m}$ are shown in Figure S5.14 and the values of T_f determined using this method are given in Figure S5.15. The values of T_f are higher using this method but qualitatively similar to trends in T_f found using a finite difference method for $\mathrm{dU/d}ln\mathrm{m}$.

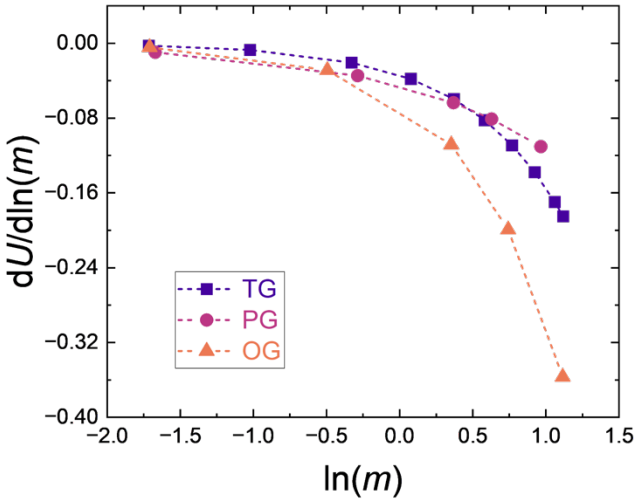

Figure S5.14. The derivative, $dU/dlnm$, plotted as a function of $ln(m)$, determined using an exponential fit, $U = a - be^{c+d(lnm)}$.

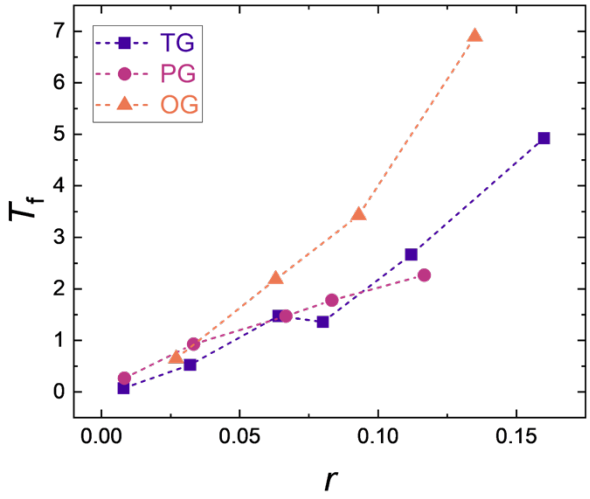

Figure S5.15. Thermodynamic factor, T_f, plotted as a function of salt concentration, r, for TG, PG, and OG. T_f was calculated using $dU/dlnm$ determined from an exponential. Data used to calculate T_f for TG and PG was measured at 30°C and data used to calculate T_f for OG was measured at 60°C.

5.8 Nomenclature

n	Number of repeat units
κ	Ionic conductivity (S cm^{-1})
D	Salt diffusion coefficient (cm^2 s^{-1})
t_+^0	Cation transference number with respect to the solvent velocity
T_f	Thermodynamic factor
r	Measure of ratio of lithium ions to oxygen atoms in solvent, ([Li$^+$]/[O]

m	Molality (mol kg^{-1})
η	Viscosity
R_s	Series resistance (Ω)
τ	Tortuosity of separator
φ_c	Volume fraction of conducting phase in separator
l	Thickness of the separator (cm)
A	Area of electrodes (cm^2)
ρ_+	Current fraction
ΔV	Applied voltage (V)
I_{ss}	Steady-state current (mA)
I_Ω	Initial current calculated via Ohm's law, $I_\Omega = \Delta V / R_T$ (mA)
$R_{i,0}$	Initial interfacial resistance (Ω)
$R_{i,ss}$	Steady-state interfacial resistance (Ω)
U	Open circuit potential (mV)
k_0	Offset voltage (mV)
a	Fit parameter for restricted diffusion
b	Fit parameter for restricted diffusion
t	Time (s)
D_s	Salt diffusion coefficient through the separator ($cm^2\ s^{-1}$)
α	Minimum time cutoff for restricted diffusion
v_+	Cation velocity (μm cm^{-1})
v_-	Anion velocity (μm cm^{-1})
v_0	Solvent velocity (μm cm^{-1})
r_c	Critical salt concentration
γ_{+-}	Mean molar activity coefficient
F	Faraday's constant (C mol^{-1})
R	Universal gas constant (8.314 J $mol^{-1}\ K^{-1}$)
T	Temperature

6 Ion Transport Characterization in a Highly Concentrated, Glyme-Based Electrolyte

6.1 Abstract

Highly concentrated electrolytes may offer many advantages over conventional electrolytes with salt concentrations near 1M, which are designed to optimize ionic conductivity. Concentrated electrolytes are fully described by two additional transport properties – salt diffusion coefficient and cation transference number with respect to the solvent velocity – and a thermodynamic factor. Highly concentrated electrolytes conduct ions using distinct mechanisms from conventional electrolytes. Glyme-based electrolytes, due to the strong solvation of cations via ether oxygens and their high viscosity, seem to have very concentration dependent transport properties. In this work, we have fully characterized a simple binary electrolyte containing LiTFSI salt dissolved over a wide salt concentration range, $0.008 < r < 0.24$. We use a combination of electrochemical methods with electrophoretic NMR, which enables precise determination of the cation transference number and thermodynamic property. Conductivity and salt diffusion are low at high salt concentration and the transference number is near or below zero. The measured transport properties are used to predict steady-state concentration and potential gradients that will form in response to passed current. We find that increasing salt concentration has a very strong and deleterious impact on the magnitude of concentration and potential gradients. Less efficient ion transport at high salt concentrations remains one of the large drawbacks of these highly concentrated systems.

6.2 Introduction

The reactivity of all conventional liquid electrolytes against lithium metal has prevented the adoption of liquid-based lithium metal batteries.[130,131] Even in the context of graphite-based lithium-ion batteries, the reactivity of the electrolyte poses a challenge in extreme use cases, such as fast charging or low temperature cycling. There has been much interest in studying highly concentrated electrolytes (HCEs) as a stable and effective electrolyte alternative.[132–136] All practical battery electrolytes are concentrated solutions as they have a variety of ion-ion and ion-solvent interactions, therefore not fulfilling requirements of a dilute solution.[5] In the literature, HCEs generally refer to electrolytes with salt concentrations well above the standard ~1M. Studies involving HCEs with salt concentrations up to 5M have demonstrated improved stability, cyclability, and Coulombic efficiency compared to low concentration electrolytes.[137–140] This improved stability has been attributed to many factors, including the enhanced electrochemical stability window, the reduction in free solvent molecules, and increased charge carrier density.[132,138] Due to the high availability of salt and reductions in parasitic reactions with the solvent, these electrolytes are less reactive against lithium metal.[135,138,141] Reactivity at the electrodes is also suspected to occur due to salt depletion, which may be prevented in highly concentrated systems.[117,120]

Concentrated electrolytes are fully described in Newman's concentrated solution theory[5] by a thermodynamic factor, T_f, and three transport properties – ionic conductivity, κ, salt diffusion coefficient, D, and the cation transference number, t_+^0. Although there is much interest on how highly concentrated electrolytes might improve cycling performance and potentially enable lithium metal batteries, there has not been much work done to study the transport properties of liquid electrolytes at high concentrations.[142] Due to the abundance of salt and high viscosity of

these electrolytes, ion transport is expected to occur via entirely different mechanisms compared to low concentrations.[143] We are interested in understanding how the transport and thermodynamics of liquid electrolytes is impacted at high concentrations. Glyme-based electrolytes are an interesting candidate to evaluate the impact of concentration on transport properties, as a significant body of work exists evaluating the solvation structure of glymes containing lithium salts.[15,25–29] Research has specifically focused on distinguishing between electrolytes that function as concentrated solutions or as solvate ionic liquids (SILs).[18,30–34] This classification is entirely salt concentration dependent.

In this work, we have characterized a simple glyme-based liquid electrolyte, lithium bis(trifluoromethanesulfonyl)imide (LiTFSI) salt dissolved in tetraethylene glycol dimethyl ether (tetraglyme) at 30°C. Previous work has reported transport and thermodynamic properties up to $m = 2.52$ mol/kg.[89] This work reports transport and thermodynamic properties above this concentration up to 5.34 mol/kg. We use a combination of electrochemical measurements and electrophoretic NMR (eNMR) to fully characterize this electrolyte, in accordance with previously published results.[89,123] eNMR allows precise determination of the cation transference number by directly measuring electric-field-induced cation, anion, and solvent velocities.[10,12,58,122,144] All measured transport properties substantially decrease at high salt concentrations. We use measured transport and thermodynamic properties to predict concentration and potential gradients based on concentrated solution theory. Highly concentrated electrolytes are predicted to have much worse concentration polarization, which may impact their efficacy in battery applications.

6.3 Experimental

6.3.1 Electrolyte Preparation

Lithium bis(trifluoromethanesulfonyl)imide (LiTFSI) salt was obtained from Sigma-Aldrich and dried in a glovebox antechamber under active vacuum for three days at 100°C. Tetraethylene glycol dimethyl ether (tetraglyme) was obtained from Sigma-Aldrich and dried in a glovebox antechamber under active vacuum for three days at 60°C. To make electrolytes, a given mass of LiTFSI salt was dissolved in a given volume of tetraglyme and stirred overnight at 25°C. Electrolytes were prepared in an argon glovebox, with oxygen and water levels kept below 1 ppm. The concentrations of electrolytes prepared ranged between $0.008 < r < 0.24$, where r describes the ratio of lithium ions in LiTFSI to ether oxygens in tetraglyme, r = ([Li^+]/[O]). The equivalent values of salt concentration in terms of molality (moles of LiTFSI per kilogram of tetraglyme), m, are provided in Table 6.1.

6.3.2 Conductivity

Conductivity was measured using a conductivity probe (Mettler Toledo InLab-751) with platinum blocking electrodes. Temperature was measured using the probe and maintained at 30°C ± 1°C for the duration of the measurement. Prior to measurement, the conductivity probe was calibrated using a 1413 μS/cm potassium chloride conductivity standard.

6.3.3 Current Fraction and Restricted Diffusion

Lithium-LiTFSI/tetraglyme-lithium symmetric cells were assembled in coin cells. Five or ten Celgard 2500 separators were soaked in electrolyte and stacked in between lithium chips (MTI Corp., 14 mm in diameter and 600 μm thick). The cell stack was topped with a stainless steel shim

and a wave spring before crimping in 2032 coin cells. Cells were made in triplicate for each salt concentration and thickness. Polarization experiments were conducted in an environmental chamber (JEIO Tech) to maintain a temperature setpoint of 30°C. This temperature was corroborated by a thermocouple.

Cells were preconditioned to establish a stabilize the interface. Preconditioning involved a four hour positive polarization of 0.02 mA/cm^2, a one hour rest, a four hour negative polarization of 0.02 mA/cm^2, followed by another one hour rest. Six conditioning cycles were applied, or until the interfacial resistance was stabilized. After preconditioning, the current fraction was measured in accordance with the Bruce-Vincent method.[41–43] The cell was polarized at ΔV = 10 mV, -10 mV, 20 mV, and -20 mV, ensuring measurements were independent of the applied potential. The steady-state current, I_{ss}, was measured for one hour and impedance measurements were taken every 20 minutes, including before and after polarization. The current fraction was determined in accordance with equation 6.1. [41–43]

$$\rho_+ = \frac{I_{ss}}{I_\Omega}\left(\frac{\Delta V - I_\Omega R_{i,0}}{\Delta V - I_{ss}R_{i,ss}}\right). \tag{6.1}$$

$R_{i,0}$ is the initial interfacial resistance before polarization and $R_{i,ss}$ is the interfacial resistance measured after I_{ss}, the steady-state current, has been reached. I_Ω is the initial current in the cell, calculated assuming Ohm's law is valid at the first instance of polarization. I_Ω was determined by dividing the applied potential, ΔV, by the total resistance in the cells, found by summing the initial bulk and interfacial resistances in the cell.

The diffusion coefficient was measured in a restricted diffusion experiment.[54] After polarization to determine the current fraction, cells were allowed to relax for one hour while the open circuit potential, U, was measured every 0.5 seconds. This relaxation describes the relaxation of the concentration gradient in the cell. U was fit to an exponential, $U(t) = k_0 + ae^{-bt}$. k_0 is an offset voltage and a and b are fit parameters. The exponent fitting parameter, b, is related to the diffusion coefficient through the separator, D_s, via $D_s = \frac{l^2 b}{\pi^2}$. U is fit to a relaxation time window depending on the thickness of the cells. All cells are fit to an initial time cutoff of $\alpha = \frac{D_s t}{l^2} > 0.03$ to ensure the fit is independent of the shape of the concentration gradient formed during polarization.[55] For the five Celgard cells (125 μm thick), D_s was obtained by fitting the first 15 minutes of relaxation. For the 10 Celgard cells, D_s was obtained by fitting the first 60 minutes of relaxation. The data was analyzed for different time periods of relaxation because increasing the thickness by a factor of two results in a fourfold increase in characteristic decay time. Fitting cells with different thicknesses to the same decay time resulted in discrepancies in D_s. This was especially true for the least concentrated salt concentrations, which decay faster than more concentrated electrolytes. The salt diffusion coefficient, D, was calculated by correcting for the tortuosity of the separator, τ, via $D = \tau D_s$. The tortuosity of Celgard 2500 is 2.93, as has been previously reported.

6.3.4 Concentration Cells

Concentration cell experiments[40,89] were conducted in custom made glass U-cells (Adams and Chittenden, Berkeley, CA). containing a porous glass frit with an average pore size of 1.0-1.6 μm.

The porous glass frit separates the two chambers and prevents rapid mixing. One side of the U-cell was filled with a reference electrolyte (r = 0.064) and the other side was filled with a test concentration. Equal volumes of electrolyte were added to each side of the concentration cell to equilibrate the heights between the two chambers and minimize pressure differences. The open circuit potential, U, was measured using lithium electrodes submerged into each side of the of the U-cell for one hour. The positive electrode was connected to the reference electrolyte so that a positive potential was measured when $m_r > m$. At least two measurements were taken for each test concentration. Concentration cells were maintained at a temperature of 30°C ± 1°C during the experiment.

6.3.5 Electrophoretic NMR

Description of electrophoretic NMR (eNMR) experiments has been reported elsewhere.[92–94] Details and methods of instrumentation, experimentation, calibration, and interpretation of data used in this work has been previously reported.[90,123] Samples were prepared in an argon glovebox by filling a dried eNMR cell with a given electrolyte. Cation, anion, and solvent velocities were measured using ^{7}Li, ^{19}F, and ^{1}H NMR experiments, respectively. Experiments were conducted at 30°C ± 1°C.

6.4 Results and Discussion

Table 6.1. Salt concentrations for tetraglyme electrolytes in units of r and molality, m.

r ([Li$^+$/O])	m (mol/kg)	r ([Li$^+$/O])	m (mol/kg)
0.008	0.18	0.128	2.89
0.016	0.36	0.136	3.06
0.032	0.72	0.16	3.60
0.048	1.08	0.168	3.78
0.064	1.45	0.184	4.14
0.08	1.79	0.20	4.54
0.096	2.16	0.208	4.67
0.112	2.52	0.24	5.40

In Figure 6.1, we plot conductivity, κ, as a function of salt concentration, r. Grey data has been previously published and blue data is new to this work. κ shows a nonmonotonic dependence on r. Below r = 0.064, conductivity increases due to an increase in charge carriers. Above r = 0.064, conductivity decreases due to frictional effects. This continues throughout the high concentration range, and at the highest salt concentration, r = 0.24, the conductivity is less than at the lowest salt concentration. The high amount of charge carriers competes with the high viscosity of concentrated electrolytes. This trend highlights one of the issues with high concentration electrolytes. Generally, high conductivity is necessary for battery electrolytes for pushing high currents and minimizing concentration gradients and concentration overpotentials. Such low

conductivity at high concentrations may impact adoptability of high concentration electrolytes. This may be a significant concern for certain applications, such as low temperature use, due to the combination of high viscosity from low temperatures and high salt concentrations.

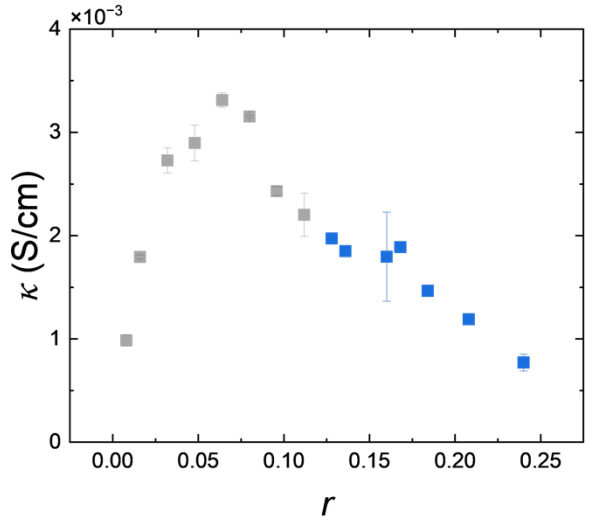

Figure 6.1. Ionic conductivity, κ, of LiTFSI/tetraglyme as a function of salt concentration, r, measured using a conductivity probe.

The relationship between viscosity and conductivity is well understood and a known problem for highly concentrated electrolytes.[77,95,96,145] However, other transport properties are not as well reported in the literature, especially at high salt concentrations. In Figure 6.2, we plot the current fraction, ρ_+, as a function of salt concentration. Grey data has been previously published and blue data is new to this work. ρ_+ is highest at the lowest salt concentration and decreases slightly with increasing salt concentration. In the high concentration range (above $r = 0.128$), ρ_+ is small and always less than 0.12. For this electrolyte, ρ_+ is small, equal to or less than 0.20 above $r = 0.016$. In Figure 6.2b, we plot the effective conductivity, $\kappa\rho_+$. This product is proportional to the current that would be obtained in the limit of a small, applied dc potential for this electrolyte.[7] $\kappa\rho_+$ has a nonmonotonic dependence on salt concentration, but above $r = 0.032$, $\kappa\rho_+$ continuously decreases. The effective conductivity at the highest salt concentrations is much lower than the peak $\kappa\rho_+$ value by about a factor of 16. Reductions in both conductivity and current fraction with increasing salt concentration compound and indicate in the limit of small potentials, electrolyte performance is expected to be worse at high concentrations.

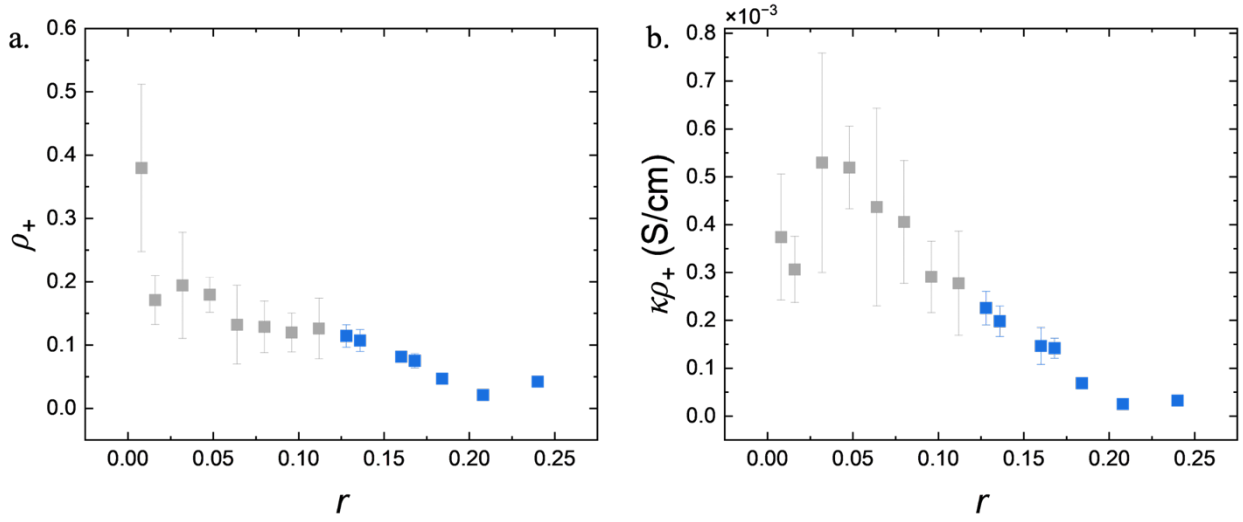

Figure 6.2. a) Current fraction, ρ_+ for LiTFSI/tetraglyme as a function of salt concentration, r, obtained using Bruce-Vincent polarization experiments. b) The effective conductivity, $\kappa\rho_+$, shown as a function of r.

In Figure 6.3, we plot salt diffusion coefficient, D, measured via restricted diffusion as a function of salt concentration. Grey data has been previously published and blue data is new to this work. We note error in the lower concentration range is higher than in the higher concentration range. This may be because it is more difficult to capture the faster relaxation of concentration gradients at these low salt concentrations, leading to more spread in the data. Salt diffusion coefficient decreases as salt concentration increases. Like with conductivity, increasing frictional effects slow diffusion of ions within the electrolyte at higher concentrations.

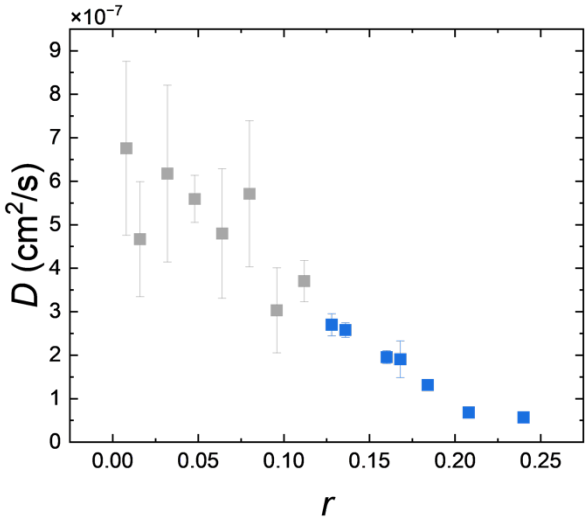

Figure 6.3. Diffusion coefficient, D, of LiTFSI/tetraglyme as a function of salt concentration, r, obtained from restricted diffusion experiments.

The open circuit voltage, U, measured in concentration cells is plotted as a function of ln(m). The reference electrolyte used here is r = 0.064. U monotonically decreases with increasing ln(m). In the high concentration regime, U decreases more sharply compared to the low concentration range.

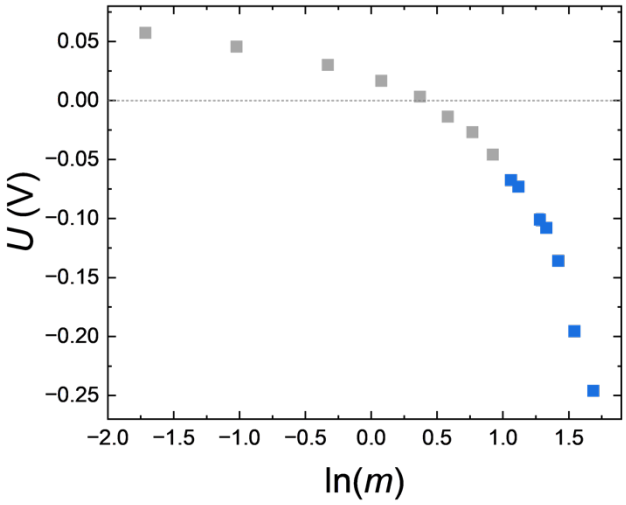

Figure 6.4. Open circuit potential, U, measured in concentration cell experiments, as a function of salt concentration, r.

We use electrophoretic NMR to directly determine the cation transference number instead of traditional electrochemical methods.[6,37,53] eNMR directly measures species' velocities under an applied electric field and these results are shown in Figure 6.5. In Figure 6.5a, we plot species velocities determined from eNMR. Previously published data ($0.008 < r < 0.112$) is shown with faded markers. The cation, v_+, and anion, v_-, velocities continuously decrease with increasing salt concentration. This magnitude of this decrease is highest at the lowest salt concentrations. Species velocities, similar to conductivity and diffusion coefficient, are affected by frictional effects of increasing solution viscosity. The solvent velocity, v_0, however, has a nonmonotonic dependence on salt concentration. Up until r = 0.08, v_0 increases with increasing salt concentration. At r = 0.08, the solvent velocity is faster than the cation velocity. Beyond r = 0.08, v_0 decreases. The solvent has a velocity under an applied electric field due to ion-solvent interactions. As has been previously reported, ion-solvent interactions increase with increasing salt concentration in the low concentration regime and increase electroosmotic drag of the solvent, which causes this increase in v_0.[58] Ion-ion and ion-solvent interactions continue to change at higher salt concentrations. Notably, there are fewer solvent molecules available to solvate cations and molecular dynamic simulations indicate anions interact more with the cation.[146] The decrease in v_0 above r = 0.08 is likely due to frictional effects, as seen with v_+ and v_-. At the highest concentration, we see a convergence of species' velocities. At higher concentration, larger solvation structures and more complex ion clustering is expected. Similar species' averaged velocities at these high concentrations reflect greater ion-ion and ion-solvent interactions, with more cations, anions, and solvents migrating together. At the highest salt concentration, r = 0.24, we see the solvent velocity is again faster than the cation.

The cation transference number with respect to the solvent velocity, t_+^0, can be determined from species' velocities via equation 6.2.[13]

$$t_+^0 = \frac{v_+ - v_0}{v_+ - v_-}. \tag{6.2}$$

We plot t_+^0 as a function of salt concentration in Figure 6.5b. Grey data has been previously published and blue data is new to this work. The transference number represents the proportion of the current carried by the cation relative to the solvent velocity in an electrolyte of uniform composition. Generally, high transference numbers ($t_+^0 > 0.5$), signaling the majority of the current is carried by the working ion, are considered desirable. The LiTFSI/tetraglyme electrolyte has low transference numbers across the concentration range. t_+^0 is highest at the lowest salt concentration, decreases until a minimum of -0.16 is reached at r = 0.08, increases until r = 0.16, and then decreases across the rest of the high concentration regime. t_+^0 is strongly affected by the magnitude of solvent velocity. At the two points where the solvent velocity is faster than the cation velocity (at r = 0.08 and r = 0.24), we obtain negative transference numbers. The nonmonotonic dependence of t_+^0 on r is due to changes in solvation motifs with increasing salt concentration.[58,146]

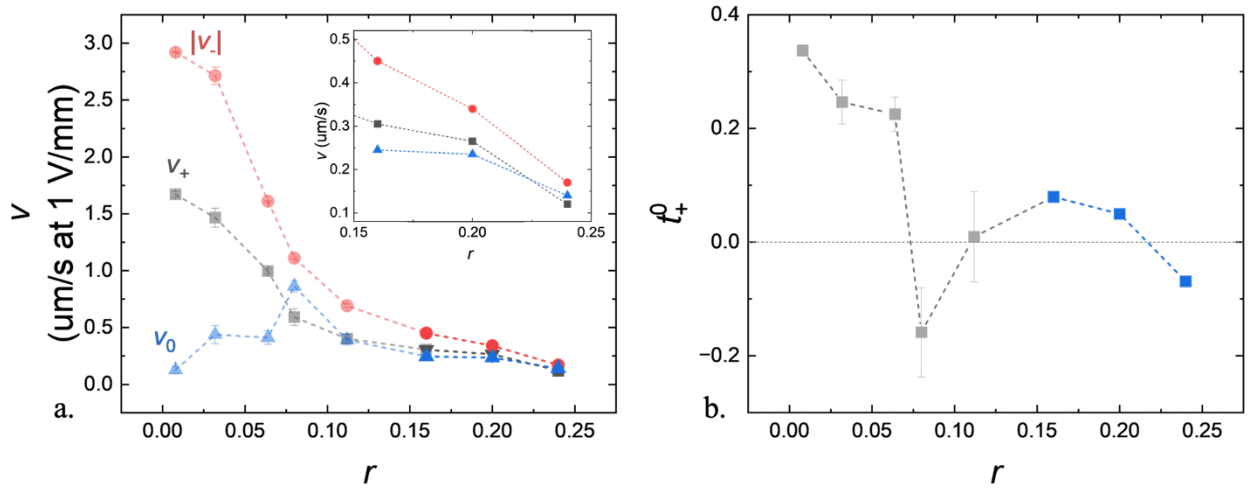

Figure 6.5. Electrophoretic NMR results for LiTFSI/tetraglyme showing a) cation, v_+, anion, v_-, and solvent, v_0, velocities and b) cation transference numbers with respect to the solvent velocity as a function of salt concentration, r.

Transference numbers from eNMR can be combined with concentration cell experiments to determine the thermodynamic factor, T_f, using equation 6.3.[5]

$$T_f = 1 + \frac{d\ln\gamma_{+-}}{d\ln m} = -\frac{F}{2RT(1 - t_+^0)}\frac{dU}{d\ln m} \tag{6.3}$$

Here, γ_{+-} is the mean molal activity coefficient of the salt, and $dU/d\ln m$ describes the change in U measured in concentration cells with respect to $\ln m$. In Figure 6.6, we plot T_f as a function of r. $dU/d\ln m$ can be determined using multiple fitting methods. Here, we use a finite difference method as has been previously described.[89] Fitting can somewhat impact the magnitude of T_f, and

this seems to matter more at the extremes of the data set. For this reason, we plot T_f determined from the finite difference method and an exponential fit, $U = a - be^{c+d(lnm)}$. The thermodynamic factor describes the ideality of an electrolyte. If the electrolyte were ideal, T_f would be 1 across the entire salt concentration range. T_f is expected to be 1 in the limit of infinite dilution, decrease in the low concentration range due to Debye-Huckel interactions, and increase at higher concentrations due to increasingly complex interactions between cations, anions, and solvent molecules. This increase in the high concentration regime reflects the nonideality of such highly concentrated systems.

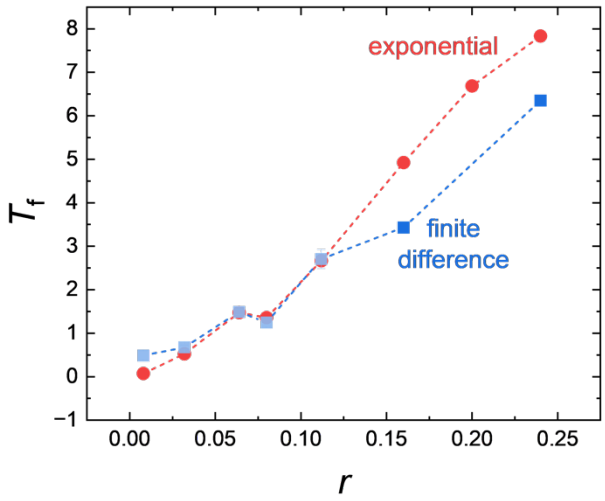

Figure 6.6. Thermodynamic factor, T_f, as a function of salt concentration, r. T_f is calculated using two methods of determining $dU/dlnm$, including a finite difference method and an exponential fit. These fitting methods give slightly different, but qualitatively similar results in the high concentration range. T_f is unity in the limit of infinite dilution.

The measured transport and thermodynamic properties can be used to model steady-state concentration and potential gradients in response to the passage of current. Concentration gradients can be modeled using equation 6.4.[14,102]

$$\int_{r(x=0)}^{r(x)} \frac{c(r)D(r)}{r\tau\left(1-t_+^0(r)\right)}\, dr = \frac{i_{ss}L}{Fz_-\nu_-}\left(\frac{x}{L}\right), \tag{6.4}$$

c is the salt concentration in units of molarity (mol/cm^3), t_+^0 is the cation transference number determined from eNMR, i_{ss} is the applied steady-state current, L is the electrolyte thickness, F is Faraday's constant, z_- is the charge number of the anion, ν_- is the number of anions the salt dissociates into, and x/L is the relative position in the electrolyte. c, D, t_+^0 are fit to continuous functions and combined into one continuous, integrable function. Salt concentration data was taken from previously published data.[147] More details about fitting of data for use in concentration gradient modeling can be found in Chapter 4. An initial guess for $r(x = 0)$ is used to solve the integral iteratively for a given i_{ss} and L until the trapezoidal average across all positions of $r(x) = r_{av}$. The concentration gradient for an applied length-normalized current density, $i_{ss}L$, of 2.5 ×

10^{-3} mA/cm for various salt concentrations is shown in Figure 6.7a. As salt concentration increases, the magnitude of the salt concentration gradient also increases.

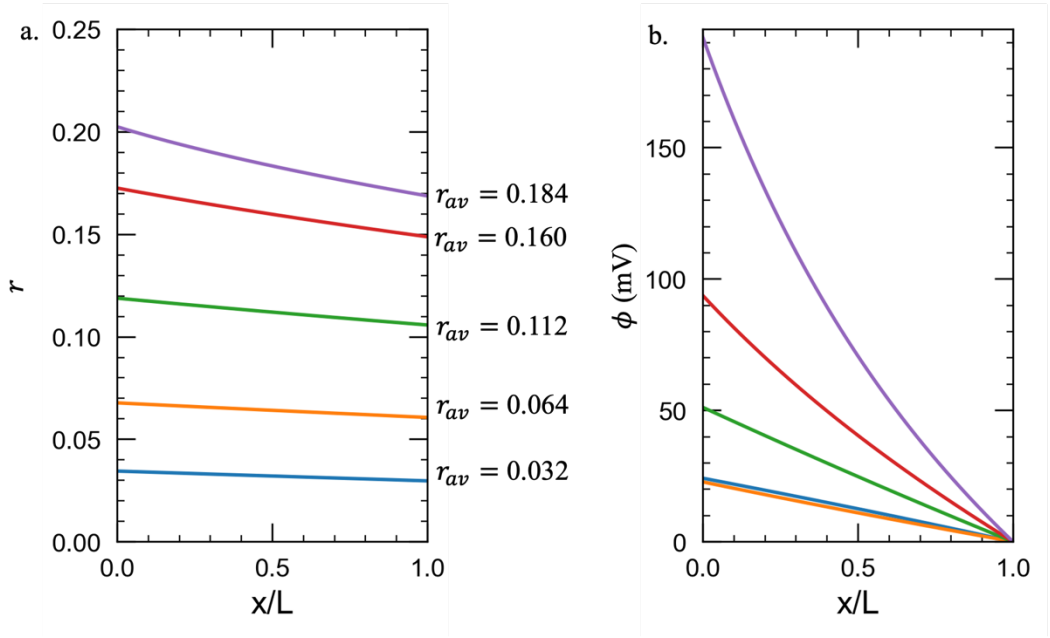

Figure 6.7. Results from modeling shown as a function of relative position in the electrolyte, x/L for for an applied length-normalized current density, i_{ss}L, of 2.5 × 10^{-3} mA/cm. a) Modeled concentration gradients for various salt concentrations and b) modeled potential gradients for the same salt concentrations.

The salt concentration gradient can be used to solve for the steady-state potential gradient, Φ_{ss}, via equation 6.5.[14,102]

$$\Phi_{ss}(x) = -Fz_{-}\nu_{-}\int_{r(x=L)}^{r(x=0)} \frac{c(r)D(r)}{r\phi_c\kappa(r)\rho_{+}(r)\left(1-t_{+}^{0}(r)\right)}dr \tag{6.5}$$

Here, Φ_{ss} refers to the potential of the positive electrode relative to the negative electrode. φ_c is the volume fraction of the separator. Modeled Φ_{ss} results are shown in Figure 6.7b for $i_{ss}L$, of 2.5 × 10^{-3} mA/cm for the same salt concentrations as Figure 6.7a. Φ_{ss} increases with increasing salt concentration. We further analyze this in Figure 6.8 and plot the length normalized potential, Φ_{ss}/L, as a function of salt concentration. Φ_{ss}/L has a nonmonotonic dependence on salt concentration and is minimized at r = 0.048. This minimum corresponds to the maximum in $\kappa\rho_{+}$ and a relatively high t_{+}^{0}. In the high salt concentration regime, Φ_{ss}/L continuously increases with increasing salt concentration. At the highest modeled salt concentration, r = 0.184, Φ_{ss}/L is ~16 times greater than the minimum at r = 0.048. Generally, minimizing salt concentration and potential gradients is considered desirable for electrolyte design, as large potential gradients limit the rate at which batteries can be charged or discharged. Gradients can be minimized by improving transport properties, such as through high conductivities and high transference numbers.[148,149] At the highest salt concentrations, κ, D, and ρ_{+} are small and t_{+}^{0} is near zero or negative, resulting in a maximum in Φ_{ss}/L. As transport is worse at these highest concentrations, highly concentrated

electrolytes may exacerbate some of the existing challenges of liquid electrolytes, such as low transference numbers and strong concentration gradients.[135,142] Although high concentration electrolytes are less reactive at lithium metal anodes and offer the promise of high voltage stability, the tradeoffs in bulk transport may impact their utility. Some solutions to these problems may involve the use of diluents or localized high concentration electrolytes (LHCEs), which take advantage of the benefits of highly concentrated electrolytes while keeping viscosity low.[143,145,150,151]

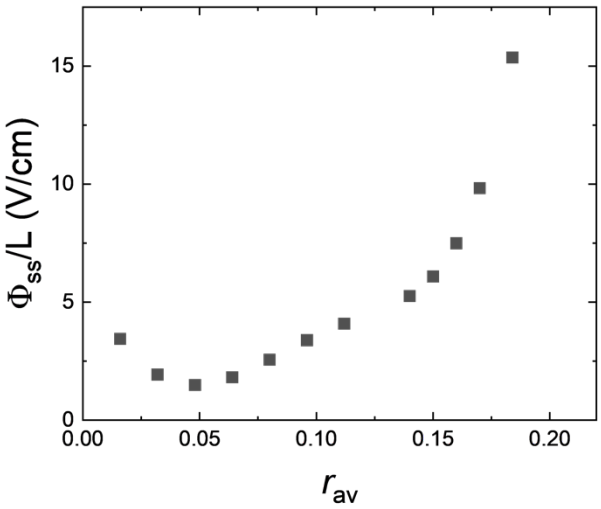

Figure 6.8. Modeled length normalized potential, Φ_{ss}/L, shown as a function of average electrolyte salt concentration, r_{av}.

6.5 Conclusion

In this work, we have fully characterized transport and thermodynamic properties of LiTFSI/tetraglyme over a wide concentration range, from $0.008 < r < 0.24$. All properties show a strong dependence on salt concentration. Conductivity, salt diffusion coefficient, and current fraction are reduced at high concentrations. The cation transference number determined using electrophoretic NMR has a nonmonotonic dependence on salt concentration, which reflects changes to solvation motifs with increasing salt concentration. Concentration and potential gradients, predicted using Newman's concentrated theory, suggest the reduced transport properties at high concentrations will cause much stronger concentration gradients and concentration overpotentials. The benefits from high salt concentration electrolytes, namely high concentration of charge carriers, reduced proportion of free solvent molecules, and high electrochemical stability, may not offset the worsening of ion transport in the bulk of the electrolyte. As high viscosity is one of the main reasons attributed to worsened ion transport, the addition of low viscosity diluents may enable the practical use of highly concentrated electrolytes.

6.6 Acknowledgements

This work was supported by the Vehicle Technologies Office of the U.S. Department of Energy's Office of Energy Efficiency and Renewable Energy under the guidance of the Advanced Battery

Cell Research Program (eXtreme fast charge Cell Evaluation of Lithium-ion batteries, XCEL). We thank Dr Hasan Celik and UC Berkeley's NMR facility in the College of Chemistry (CoC-NMR) for spectroscopic assistance. The NMR instrument used in this work was supported by the National Science Foundation under grant no. 2018784. Julia Im measured all reported electrophoretic NMR data with the support and mentorship of David M. Halat. D.M.H. and J.I. gratefully acknowledge support as a Pines Magnetic Resonance Center.

6.7 Nomenclature

T_f	Thermodynamic factor
κ	Ionic conductivity (S cm^{-1})
D	Salt diffusion coefficient (cm^2 s^{-1})
t_+^0	Cation transference number with respect to the solvent velocity
r	Measure of ratio of lithium ions to oxygen atoms in solvent
m	Molality (mol kg^{-1})
ΔV	Applied voltage (V)
I_{ss}	Steady-state current (mA)
ρ_+	Current fraction
$R_{i,0}$	Initial interfacial resistance (Ω)
$R_{i,ss}$	Steady-state interfacial resistance (Ω)
I_Ω	Initial current calculated via Ohm's law, $I_\Omega = \Delta V / R_T$ (mA)
U	Open circuit potential (mV)
k_0	Offset voltage (mV)
a	Fit parameter for restricted diffusion
b	Fit parameter for restricted diffusion
l	Thickness of the separator (cm)
t	Time (s)
D_s	Salt diffusion coefficient through the separator (cm^2 s^{-1})
α	Minimum time cutoff for restricted diffusion
τ	Tortuosity of separator
v_+	Cation velocity (μm cm^{-1})
v_-	Anion velocity (μm cm^{-1})
v_0	Solvent velocity (μm cm^{-1})
γ_{+-}	Mean molar activity coefficient
F	Faraday's constant (C mol^{-1})
R	Universal gas constant (8.314 J mol^{-1} K^{-1})
T	Temperature (°C)
$dU/dlnm$	Change in open circuit potential with respect to log of molality measured in a concentration cell experiment
c	Concentration of the salt (mol cm^{-3})
i_{ss}	Steady-state applied current density, used in concentration gradient modeling (mA cm^{-2})
L	Distance between electrodes, used in concentration gradient modeling
x/L	Dimensionless position across the electrolyte, used in concentration gradient modeling

F	Faraday's constant (C mol^{-1})
z_-	Anion charge number
ν_-	Number of anions the salt dissolves into
r_{av}	Average concentration of the electrolyte, used in concentration gradient modeling
Φ_{ss}	Potential of the positive electrode relative to the negative electrode during steady-state polarization (V)
φ_c	Volume fraction of conducting phase in separator

7 Conclusions

All practical battery electrolytes are composed of concentrated solutions that are difficult to fully characterize due to ion-ion interactions, cation solvation, and thermodynamic nonidealities. Although conductivity is often used as the primary metric to screen the viability of a given electrolyte, electrolytes are only fully described with two additional transport properties – the salt diffusion coefficient and cation transference number with respect to the solvent velocity – and a thermodynamic factor. Newman's concentrated theory provides a framework to study these properties, which has been extensively used to describe polymer electrolytes. This methodology involves four independent experiments that can be combined to determine the cation transference number. Error from each experiments compounds and reduces precision in the derived transference number. Characterization of liquid electrolytes poses additional challenges because of the inherent reactivity against lithium metal. In this dissertation, we describe a new methodology to fully characterize liquid electrolytes.

In Chapter 2, we presented a new methodology for characterizing bulk ion transport in liquid electrolytes that combines electrochemical experiments with electrophoretic NMR. We fully characterized an exemplar liquid electrolyte, LiTFSI salt dissolve in tetraglyme, using ac impedance spectroscopy to measure conductivity, restricted diffusion to measure salt diffusion coefficient, polarization experiments to measure current fraction, and concentration cells to measure the change in open circuit potential with respect to log of molality. In accordance with traditional methods, these four experiments were combined to give estimates of the transference number and thermodynamic factor. We then directly determined the cation transference number using measurements of cation, anion, and solvent velocities from electrophoretic NMR. Electrophoretic NMR more precisely determined cation transference numbers compared to electrochemical methods and additionally enabled precise determination of the thermodynamic factor.

In Chapter 3, we extended the methodology established in Chapter 2 to investigate low temperature impacts on ion transport, which is a contemporary problem for various technologies involving lithium-ion batteries. We studied the same tetraglyme-based electrolyte over a wide temperature range from -20 to 45°C. Conductivity and salt diffusion coefficient both decreased with temperature, but the magnitude of this decrease strongly depended on salt concentration. The decrease in conductivity with temperature is almost entirely described by increases in electrolyte viscosity. The salt diffusion coefficient, however, is not, as the salt diffusion coefficient is dependent on both viscosity and thermodynamic effects. We found the product of viscosity and the Stefan-Maxwell diffusion coefficient, which is based on a thermodynamic driving force, is independent of both temperature and salt concentration. Measured cation, anion, and solvent velocities decreased monotonically with temperature. We find the cation transference number measured has a complex dependence on temperature that varies with salt concentration. The trends in the transference number are very dependent on trends in the measured solvent velocity, which can have a nonmonotonic dependence on temperature. This is attributed to changes in cation solvation with temperature. We found the thermodynamic factor was a weak function of temperature. Concentration and potential gradients predicted using the measured transport parameters and concentrated solution theory indicated concentration polarization is much more severe at cold temperatures. For a given applied potential, the resulting steady current was found to be 130-202 times less at -20°C relative to 45°C.

In Chapter 4, we returned to the discrepancy in transference numbers found from electrochemical techniques and electrophoretic NMR in Chapter 2. Current versus voltage characteristics of an electrolyte can be predicted using concentrated solution theory for a fully characterized electrolyte. The combination of electrochemical methods with electrophoretic NMR creates an abundance of information for modeling. In this work, we compared two methods of modeling – one based on transference numbers determined from electrochemical methods and one based on transference numbers from electrophoretic NMR. Electrochemical methods largely determine more negative transference numbers than electrophoretic NMR across all salt concentrations and temperatures. Modeled concentration gradients are much larger for electrochemical methods, attributed to the smaller, more negative transference numbers. However, both methods predicted remarkably similar potential gradients. At small potentials, these predictions agreed well with experiments. If characterization of this electrolyte was restricted to current-voltage relationships, it would be impossible to tell which value of the transference number is correct. Additional experiments, in the form of measured *in situ* concentration gradients or limiting current experiments, would be needed to uniquely determine the transference number.

In Chapters 5 and 6, we used the established methodology to further study ion transport in glyme-based electrolytes. In Chapter 5, we looked at the impact of chain length on ion transport for oligoether glyme solvents, including tetraglyme, pentaglyme, and octaglyme. We found that increasing chain length resulted in monotonic decreases in ion conductivities, salt diffusion coefficients, and the magnitude of species' velocities measured via electrophoretic NMR. The cation transference number, however, was similar in magnitude across all electrolytes and had a characteristic "V shaped" dependence on salt concentration. The transference number was highest at the low salt concentrations, decreased with increasing salt concentration until a minimum was reached, and then increased in the higher concentration range. The minimum in the transference number corresponds to the maximum in solvent velocity, or when the maximum number of solvent molecules are involved in solvation. This value is well predicted by a simple critical salt concentration, which is the inverse of the number of oxygens involved in the solvation of one cation.

In Chapter 6, we examined the impact of high salt concentration on transport and thermodynamic properties. Conductivity, salt diffusion coefficient, and current fraction were all reduced at high salt concentrations. The transference number was found to have a nonmonotonic dependence on salt concentration but was near or below zero at high salt concentrations. Worsened transport at high salt concentrations negatively impacted modeled salt concentration and potential gradients. Concentration polarization increases with increasing salt concentration. High viscosity at high salt concentrations is one of the main factors worsening ion transport.

8 References

(1) US EPA, O. *Sources of Greenhouse Gas Emissions*. https://www.epa.gov/ghgemissions/sources-greenhouse-gas-emissions (accessed 2024-07-29).

(2) Zhang, J.; Zhang, J.; Liu, T.; Wu, H.; Tian, S.; Zhou, L.; Zhang, B.; Cui, G. Toward Low-Temperature Lithium Batteries: Advances and Prospects of Unconventional Electrolytes. *Adv. Energy Sustain. Res.* **2021**, *2* (10), 2100039. https://doi.org/10.1002/aesr.202100039.

(3) Hubble, D.; Brown, D. E.; Zhao, Y.; Fang, C.; Lau, J.; McCloskey, B. D.; Liu, G. Liquid Electrolyte Development for Low-Temperature Lithium-Ion Batteries. *Energy Environ. Sci.* **2022**, *15* (2), 550–578. https://doi.org/10.1039/D1EE01789F.

(4) Xu, K. Nonaqueous Liquid Electrolytes for Lithium-Based Rechargeable Batteries. *Chem. Rev.* **2004**, *104* (10), 4303–4418. https://doi.org/10.1021/cr030203g.

(5) John Newman; Nitash Balsara. *Electrochemical Systems*; John Wiley & Sons Inc., 2021.

(6) Pesko, D. M.; Timachova, K.; Bhattacharya, R.; Smith, M. C.; Villaluenga, I.; Newman, J.; Balsara, N. P. Negative Transference Numbers in Poly(Ethylene Oxide)-Based Electrolytes. *J. Electrochem. Soc.* **2017**, *164* (11), E3569–E3575. https://doi.org/10.1149/2.0581711jes.

(7) Galluzzo, M. D.; Maslyn, J. A.; Shah, D. B.; Balsara, N. P. Ohm's Law for Ion Conduction in Lithium and beyond-Lithium Battery Electrolytes. *J. Chem. Phys.* **2019**, *151* (2), 020901. https://doi.org/10.1063/1.5109684.

(8) Ma, Y.; Doyle, M.; Fuller, T. F.; Doeff, M. M.; De Jonghe, L. C.; Newman, J. The Measurement of a Complete Set of Transport Properties for a Concentrated Solid Polymer Electrolyte Solution. *J. Electrochem. Soc.* **1995**, *142* (6), 1859–1868. https://doi.org/10.1149/1.2044206.

(9) Gao, K. W.; Balsara, N. P. Electrochemical Properties of Poly(Ethylene Oxide) Electrolytes above the Entanglement Threshold. *Solid State Ion.* **2021**, *364*, 115609. https://doi.org/10.1016/j.ssi.2021.115609.

(10) Holz, M. Electrophoretic NMR. *Chem. Soc. Rev.* **1994**, *23* (3), 165. https://doi.org/10.1039/cs9942300165.

(11) Walls, H. J.; T. A. Zawodzinski. Anion and Cation Transference Numbers Determined by Electrophoretic NMR of Polymer Electrolytes Sum to Unity. *Electrochem. Solid-State Lett.* **1999**, *3* (7), 321. https://doi.org/10.1149/1.1391136.

(12) Gouverneur, M.; Kopp, J.; Van Wüllen, L.; Schönhoff, M. Direct Determination of Ionic Transference Numbers in Ionic Liquids by Electrophoretic NMR. *Phys. Chem. Chem. Phys.* **2015**, *17* (45), 30680–30686. https://doi.org/10.1039/C5CP05753A.

(13) Timachova, K.; Newman, J.; Balsara, N. P. Theoretical Interpretation of Ion Velocities in Concentrated Electrolytes Measured by Electrophoretic NMR. *J. Electrochem. Soc.* **2019**, *166* (2), A264–A267. https://doi.org/10.1149/2.0591902jes.

(14) Pesko, D. M.; Feng, Z.; Sawhney, S.; Newman, J.; Srinivasan, V.; Balsara, N. P. Comparing Cycling Characteristics of Symmetric Lithium-Polymer-Lithium Cells with Theoretical Predictions. *J. Electrochem. Soc.* **2018**, *165* (13), A3186–A3194. https://doi.org/10.1149/2.0921813jes.

(15) Di Lecce, D.; Marangon, V.; Jung, H.-G.; Tominaga, Y.; Greenbaum, S.; Hassoun, J. Glyme-Based Electrolytes: Suitable Solutions for next-Generation Lithium Batteries. *Green Chem.* **2022**, *24* (3), 1021–1048. https://doi.org/10.1039/D1GC03996B.

(16) Yoshida, K.; Tsuchiya, M.; Tachikawa, N.; Dokko, K.; Watanabe, M. Change from Glyme Solutions to Quasi-Ionic Liquids for Binary Mixtures Consisting of Lithium Bis(Trifluoromethanesulfonyl)Amide and Glymes. *J. Phys. Chem. C* **2011**, *115* (37), 18384–18394. https://doi.org/10.1021/jp206881t.
(17) Ueno, K.; Yoshida, K.; Tsuchiya, M.; Tachikawa, N.; Dokko, K.; Watanabe, M. Glyme–Lithium Salt Equimolar Molten Mixtures: Concentrated Solutions or Solvate Ionic Liquids? *J. Phys. Chem. B* **2012**, *116* (36), 11323–11331. https://doi.org/10.1021/jp307378j.
(18) Aguilera, L.; Xiong, S.; Scheers, J.; Matic, A. A Structural Study of LiTFSI–Tetraglyme Mixtures: From Diluted Solutions to Solvated Ionic Liquids. *J. Mol. Liq.* **2015**, *210*, 238–242. https://doi.org/10.1016/j.molliq.2015.04.053.
(19) Borodin, O.; Smith, G. D. Li + Transport Mechanism in Oligo(Ethylene Oxide)s Compared to Carbonates. *J. Solut. Chem.* **2007**, *36* (6), 803–813. https://doi.org/10.1007/s10953-007-9146-1.
(20) Borodin, O.; Smith, G. D. Mechanism of Ion Transport in Amorphous Poly(Ethylene Oxide)/LiTFSI from Molecular Dynamics Simulations. *Macromolecules* **2006**, *39* (4), 1620–1629. https://doi.org/10.1021/ma052277v.
(21) *Batteries for Sustainability: Selected Entries from the Encyclopedia of Sustainability Science and Technology*; Brodd, R. J., Ed.; Springer New York: New York, NY, 2013. https://doi.org/10.1007/978-1-4614-5791-6.
(22) Fang, C.; Halat, D. M.; Balsara, N. P.; Wang, R. Dynamic Heterogeneity of Solvent Motion and Ion Transport in Concentrated Electrolytes. *J. Phys. Chem. B* **2023**, *127* (8), 1803–1810. https://doi.org/10.1021/acs.jpcb.2c08029.
(23) Fang, C.; Loo, W. S.; Wang, R. Salt Activity Coefficient and Chain Statistics in Poly(Ethylene Oxide)-Based Electrolytes. *Macromolecules* **2021**, *54* (6), 2873–2881. https://doi.org/10.1021/acs.macromol.0c01850.
(24) Zhang, C.; Ueno, K.; Yamazaki, A.; Yoshida, K.; Moon, H.; Mandai, T.; Umebayashi, Y.; Dokko, K.; Watanabe, M. Chelate Effects in Glyme/Lithium Bis(Trifluoromethanesulfonyl)Amide Solvate Ionic Liquids. I. Stability of Solvate Cations and Correlation with Electrolyte Properties. *J. Phys. Chem. B* **2014**, *118* (19), 5144–5153. https://doi.org/10.1021/jp501319e.
(25) Jankowski, P.; Dranka, M.; Wieczorek, W.; Johansson, P. TFSI and TDI Anions: Probes for Solvate Ionic Liquid and Disproportionation-Based Lithium Battery Electrolytes. *J. Phys. Chem. Lett.* **2017**, *8* (15), 3678–3682. https://doi.org/10.1021/acs.jpclett.7b01160.
(26) Shigenobu, K.; Dokko, K.; Watanabe, M.; Ueno, K. Solvent Effects on Li Ion Transference Number and Dynamic Ion Correlations in Glyme- and Sulfolane-Based Molten Li Salt Solvates. *Phys. Chem. Chem. Phys.* **2020**, *22* (27), 15214–15221. https://doi.org/10.1039/D0CP02181D.
(27) Saito, S.; Watanabe, H.; Hayashi, Y.; Matsugami, M.; Tsuzuki, S.; Seki, S.; Canongia Lopes, J. N.; Atkin, R.; Ueno, K.; Dokko, K.; Watanabe, M.; Kameda, Y.; Umebayashi, Y. Li^+ Local Structure in Li–Tetraglyme Solvate Ionic Liquid Revealed by Neutron Total Scattering Experiments with the $^{6/7}$ Li Isotopic Substitution Technique. *J. Phys. Chem. Lett.* **2016**, *7* (14), 2832–2837. https://doi.org/10.1021/acs.jpclett.6b01266.
(28) Dong, D.; Sälzer, F.; Roling, B.; Bedrov, D. How Efficient Is Li^+ Ion Transport in Solvate Ionic Liquids under Anion-Blocking Conditions in a Battery? *Phys. Chem. Chem. Phys.* **2018**, *20* (46), 29174–29183. https://doi.org/10.1039/C8CP06214E.

(29) Shigenobu, K.; Shibata, M.; Dokko, K.; Watanabe, M.; Fujii, K.; Ueno, K. Anion Effects on Li Ion Transference Number and Dynamic Ion Correlations in Glyme–Li Salt Equimolar Mixtures. *Phys. Chem. Chem. Phys.* **2021**, *23* (4), 2622–2629. https://doi.org/10.1039/D0CP06381A.
(30) Nachaki, E. O.; Kuroda, D. G. Transitioning from Regular Electrolytes to Solvate Ionic Liquids to High-Concentration Electrolytes: Changes in Transport Properties and Ionic Speciation. *J. Phys. Chem. C* **2024**, *128* (28), 11522–11533. https://doi.org/10.1021/acs.jpcc.4c02248.
(31) Arai, N.; Watanabe, H.; Nozaki, E.; Seki, S.; Tsuzuki, S.; Ueno, K.; Dokko, K.; Watanabe, M.; Kameda, Y.; Umebayashi, Y. Speciation Analysis and Thermodynamic Criteria of Solvated Ionic Liquids: Ionic Liquids or Superconcentrated Solutions? *J. Phys. Chem. Lett.* **2020**, *11* (11), 4517–4523. https://doi.org/10.1021/acs.jpclett.0c00906.
(32) Terada, S.; Ikeda, K.; Ueno, K.; Dokko, K.; Watanabe, M. Liquid Structures and Transport Properties of Lithium Bis(Fluorosulfonyl)Amide/Glyme Solvate Ionic Liquids for Lithium Batteries. *Aust. J. Chem.* **2019**, *72* (2), 70. https://doi.org/10.1071/CH18270.
(33) Ueno, K.; Yoshida, K.; Tsuchiya, M.; Tachikawa, N.; Dokko, K.; Watanabe, M. Glyme–Lithium Salt Equimolar Molten Mixtures: Concentrated Solutions or Solvate Ionic Liquids? *J. Phys. Chem. B* **2012**, *116* (36), 11323–11331. https://doi.org/10.1021/jp307378j.
(34) Mandai, T.; Yoshida, K.; Ueno, K.; Dokko, K.; Watanabe, M. Criteria for Solvate Ionic Liquids. *Phys. Chem. Chem. Phys.* **2014**, *16* (19), 8761. https://doi.org/10.1039/c4cp00461b.
(35) Goodenough, J. B.; Kim, Y. Challenges for Rechargeable Li Batteries. *Chem. Mater.* **2010**, *22* (3), 587–603. https://doi.org/10.1021/cm901452z.
(36) Pesko, D. M.; Sawhney, S.; Newman, J.; Balsara, N. P. Comparing Two Electrochemical Approaches for Measuring Transference Numbers in Concentrated Electrolytes. *J. Electrochem. Soc.* **2018**, *165* (13), A3014–A3021. https://doi.org/10.1149/2.0231813jes.
(37) Landesfeind, J.; Gasteiger, H. A. Temperature and Concentration Dependence of the Ionic Transport Properties of Lithium-Ion Battery Electrolytes. *J. Electrochem. Soc.* **2019**, *166* (14), A3079–A3097. https://doi.org/10.1149/2.0571912jes.
(38) Hou, T.; Monroe, C. W. Composition-Dependent Thermodynamic and Mass-Transport Characterization of Lithium Hexafluorophosphate in Propylene Carbonate. *Electrochimica Acta* **2020**, *332*, 135085. https://doi.org/10.1016/j.electacta.2019.135085.
(39) Craig, N.; Mullin, S. A.; Pratt, R.; Crane, G. B. Determination of Transference Number and Thermodynamic Factor by Use of Anion-Exchange Concentration Cells and Concentration Cells. *J. Electrochem. Soc.* **2019**, *166* (13), A2769–A2775. https://doi.org/10.1149/2.0351913jes.
(40) Stewart, S.; Newman, J. Measuring the Salt Activity Coefficient in Lithium-Battery Electrolytes. *J. Electrochem. Soc.* **2008**, *155* (6), A458. https://doi.org/10.1149/1.2904526.
(41) Evans, J.; Vincent, C. A.; Bruce, P. G. Electrochemical Measurement of Transference Numbers in Polymer Electrolytes. *Polymer* **1987**, *28* (13), 2324–2328. https://doi.org/10.1016/0032-3861(87)90394-6.
(42) Bruce, P. G.; Vincent, C. A. Steady State Current Flow in Solid Binary Electrolyte Cells. *J. Electroanal. Chem. Interfacial Electrochem.* **1987**, *225* (1–2), 1–17. https://doi.org/10.1016/0022-0728(87)80001-3.
(43) Watanabe, M.; Nagano, S.; Sanui, K.; Ogata, N. Estimation of Li+ Transport Number in Polymer Electrolytes by the Combination of Complex Impedance and Potentiostatic

Polarization Measurements. *Solid State Ion.* **1987**. https://doi.org/10.1016/0167-2738(88)90303-7.
(44) Frenck, L.; Sethi, G. K.; Maslyn, J. A.; Balsara, N. P. Factors That Control the Formation of Dendrites and Other Morphologies on Lithium Metal Anodes. *Front. Energy Res.* **2019**, *7*, 115. https://doi.org/10.3389/fenrg.2019.00115.
(45) Brissot, C.; Rosso, M.; Chazalviel, J.-N.; Baudry, P.; Lascaud, S. In Situ Study of Dendritic Growth Inlithium/PEO-Salt/Lithium Cells. *Electrochimica Acta* **1998**, *43* (10–11), 1569–1574. https://doi.org/10.1016/S0013-4686(97)10055-X.
(46) Grundy, L. S.; Shah, D. B.; Nguyen, H. Q.; Diederichsen, K. M.; Celik, H.; DeSimone, J. M.; McCloskey, B. D.; Balsara, N. P. Impact of Frictional Interactions on Conductivity, Diffusion, and Transference Number in Ether- and Perfluoroether-Based Electrolytes. *J. Electrochem. Soc.* **2020**, *167* (12), 120540. https://doi.org/10.1149/1945-7111/abb34e.
(47) Schmidt, F.; Schönhoff, M. Solvate Cation Migration and Ion Correlations in Solvate Ionic Liquids. *J. Phys. Chem. B* **2020**, *124* (7), 1245–1252. https://doi.org/10.1021/acs.jpcb.9b11330.
(48) Pietsch, P.; Wood, V. X-Ray Tomography for Lithium Ion Battery Research: A Practical Guide. *Annu. Rev. Mater. Res.* **2017**, *47* (1), 451–479. https://doi.org/10.1146/annurev-matsci-070616-123957.
(49) Pietsch, P.; Westhoff, D.; Feinauer, J.; Eller, J.; Marone, F.; Stampanoni, M.; Schmidt, V.; Wood, V. Quantifying Microstructural Dynamics and Electrochemical Activity of Graphite and Silicon-Graphite Lithium Ion Battery Anodes. *Nat. Commun.* **2016**, *7* (1), 12909. https://doi.org/10.1038/ncomms12909.
(50) Sun, F.; Moroni, R.; Dong, K.; Markötter, H.; Zhou, D.; Hilger, A.; Zielke, L.; Zengerle, R.; Thiele, S.; Banhart, J.; Manke, I. Study of the Mechanisms of Internal Short Circuit in a Li/Li Cell by Synchrotron X-Ray Phase Contrast Tomography. *ACS Energy Lett.* **2017**, *2* (1), 94–104. https://doi.org/10.1021/acsenergylett.6b00589.
(51) Sun, F.; Zielke, L.; Markötter, H.; Hilger, A.; Zhou, D.; Moroni, R.; Zengerle, R.; Thiele, S.; Banhart, J.; Manke, I. Morphological Evolution of Electrochemically Plated/Stripped Lithium Microstructures Investigated by Synchrotron X-Ray Phase Contrast Tomography. *ACS Nano* **2016**, *10* (8), 7990–7997. https://doi.org/10.1021/acsnano.6b03939.
(52) Harry, K. J.; Hallinan, D. T.; Parkinson, D. Y.; MacDowell, A. A.; Balsara, N. P. Detection of Subsurface Structures underneath Dendrites Formed on Cycled Lithium Metal Electrodes. *Nat. Mater.* **2014**, *13* (1), 69–73. https://doi.org/10.1038/nmat3793.
(53) Shah, D. B.; Nguyen, H. Q.; Grundy, L. S.; Olson, K. R.; Mecham, S. J.; DeSimone, J. M.; Balsara, N. P. Difference between Approximate and Rigorously Measured Transference Numbers in Fluorinated Electrolytes. *Phys. Chem. Chem. Phys.* **2019**, *21* (15), 7857–7866. https://doi.org/10.1039/C9CP00216B.
(54) Newman, J.; Chapman, T. W. Restricted Diffusion in Binary Solutions. *AIChE J.* **1973**, *19* (2), 343–348. https://doi.org/10.1002/aic.690190220.
(55) Thompson, S. D.; Newman, J. Differential Diffusion Coefficients of Sodium Polysulfide Melts. *J. Electrochem. Soc.* **1989**, *136* (11), 3362–3369. https://doi.org/10.1149/1.2096451.
(56) Ho, A. S.; Parkinson, D. Y.; Finegan, D. P.; Trask, S. E.; Jansen, A. N.; Tong, W.; Balsara, N. P. 3D Detection of Lithiation and Lithium Plating in Graphite Anodes during Fast Charging. *ACS Nano* **2021**, *15* (6), 10480–10487. https://doi.org/10.1021/acsnano.1c02942.
(57) Maslyn, J. A.; Frenck, L.; Veeraraghavan, V. D.; Müller, A.; Ho, A. S.; Marwaha, N.; Loo, W. S.; Parkinson, D. Y.; Minor, A. M.; Balsara, N. P. Limiting Current in Nanostructured

Block Copolymer Electrolytes. *Macromolecules* **2021**, *54* (9), 4010–4022. https://doi.org/10.1021/acs.macromol.1c00425.
(58) Halat, D. M.; Fang, C.; Hickson, D.; Mistry, A.; Reimer, J. A.; Balsara, N. P.; Wang, R. Electric-Field-Induced Spatially Dynamic Heterogeneity of Solvent Motion and Cation Transference in Electrolytes. *Phys. Rev. Lett.* **2022**, *128* (19), 198002. https://doi.org/10.1103/PhysRevLett.128.198002.
(59) Hallberg, F.; Furó, I.; Yushmanov, P. V.; Stilbs, P. Sensitive and Robust Electrophoretic NMR: Instrumentation and Experiments. *J. Magn. Reson.* **2008**, *192* (1), 69–77. https://doi.org/10.1016/j.jmr.2008.02.001.
(60) Fawdon, J.; Ihli, J.; Mantia, F. L.; Pasta, M. Characterising Lithium-Ion Electrolytes via Operando Raman Microspectroscopy. *Nat. Commun.* **2021**, *12* (1), 4053. https://doi.org/10.1038/s41467-021-24297-0.
(61) Stewart, S. G.; Newman, J. The Use of UV/Vis Absorption to Measure Diffusion Coefficients in LiPF6 Electrolytic Solutions. *J. Electrochem. Soc.*
(62) Valøen, L. O.; Reimers, J. N. Transport Properties of LiPF6-Based Li-Ion Battery Electrolytes. *J. Electrochem. Soc.* **2005**. https://doi.org/10.1149/1.1872737.
(63) Balsara, N. P.; Newman, J. Relationship between Steady-State Current in Symmetric Cells and Transference Number of Electrolytes Comprising Univalent and Multivalent Ions. *J. Electrochem. Soc.* **2015**, *162* (14), A2720–A2722. https://doi.org/10.1149/2.0651514jes.
(64) Michael Galluzzo. Salt Concentration Gradients in Block Copolymer Electrolytes, University of California, Berkeley, Berkeley, CA, 2021. https://escholarship.org/uc/item/67c3087r.
(65) Loo, W. S.; Fang, C.; Balsara, N. P.; Wang, R. Uncovering Local Correlations in Polymer Electrolytes by X-Ray Scattering and Molecular Dynamics Simulations. *Macromolecules* **2021**, *54* (14), 6639–6648. https://doi.org/10.1021/acs.macromol.1c00995.
(66) France-Lanord, A.; Grossman, J. C. Correlations from Ion Pairing and the Nernst-Einstein Equation. *Phys. Rev. Lett.* **2019**, *122* (13), 136001. https://doi.org/10.1103/PhysRevLett.122.136001.
(67) Nilsson, V.; Bernin, D.; Brandell, D.; Edström, K.; Johansson, P. Interactions and Transport in Highly Concentrated LiTFSI-based Electrolytes. *ChemPhysChem* **2020**, *21* (11), 1166–1176. https://doi.org/10.1002/cphc.202000153.
(68) P. Debye; E. Huckel. Theorie Der Elektrolyte. *Phys. Z.* **1923**, *24* (9).
(69) Lin, H. -p.; Chua, D.; Salomon, M.; Shiao, H.-C.; Hendrickson, M.; Plichta, E.; Slane, S. Low-Temperature Behavior of Li-Ion Cells. *Electrochem. Solid-State Lett.* **2001**, *4* (6), A71. https://doi.org/10.1149/1.1368736.
(70) Jow, T. R.; Ding, M. S.; Xu, K.; Zhang, S. S.; Allen, J. L.; Amine, K.; Henriksen, G. L. Nonaqueous Electrolytes for Wide-Temperature-Range Operation of Li-Ion Cells. *J. Power Sources* **2003**, *119–121*, 343–348. https://doi.org/10.1016/S0378-7753(03)00153-8.
(71) Zhang, S. S.; Xu, K.; Jow, T. R. The Low Temperature Performance of Li-Ion Batteries. *J. Power Sources* **2003**, *115* (1), 137–140. https://doi.org/10.1016/S0378-7753(02)00618-3.
(72) Jow, R.; Zhang, S. S.; Xu, K.; Allen, J. Electrolytes for Low Temperature Operations of Li-Ion Batteries. *ECS Trans.* **2007**, *3* (27), 51–58. https://doi.org/10.1149/1.2793578.
(73) Li, Q.; Lu, D.; Zheng, J.; Jiao, S.; Luo, L.; Wang, C.-M.; Xu, K.; Zhang, J.-G.; Xu, W. Li^+-Desolvation Dictating Lithium-Ion Battery's Low-Temperature Performances. *ACS Appl. Mater. Interfaces* **2017**, *9* (49), 42761–42768. https://doi.org/10.1021/acsami.7b13887.

(74) Wang, C.; Appleby, A. J.; Little, F. E. Low-Temperature Characterization of Lithium-Ion Carbon Anodes via Microperturbation Measurement. *J. Electrochem. Soc.* **2002**, *149* (6), A754. https://doi.org/10.1149/1.1474427.
(75) Huang, C.-K.; Sakamoto, J. S.; Wolfenstine, J.; Surampudi, S. The Limits of Low-Temperature Performance of Li-Ion Cells. *J. Electrochem. Soc.* **2000**, *147* (8), 2893. https://doi.org/10.1149/1.1393622.
(76) Smart, M. C.; Ratnakumar, B. V.; Surampudi, S. Electrolytes for Low-Temperature Lithium Batteries Based on Ternary Mixtures of Aliphatic Carbonates. *J. Electrochem. Soc.* **1999**, *146* (2), 486–492. https://doi.org/10.1149/1.1391633.
(77) Logan, E. R.; Tonita, E. M.; Gering, K. L.; Li, J.; Ma, X.; Beaulieu, L. Y.; Dahn, J. R. A Study of the Physical Properties of Li-Ion Battery Electrolytes Containing Esters. *J. Electrochem. Soc.* **2018**, *165* (2), A21–A30. https://doi.org/10.1149/2.0271802jes.
(78) Ma, X.; Arumugam, R. S.; Ma, L.; Logan, E.; Tonita, E.; Xia, J.; Petibon, R.; Kohn, S.; Dahn, J. R. A Study of Three Ester Co-Solvents in Lithium-Ion Cells. *J. Electrochem. Soc.* **2017**, *164* (14), A3556–A3562. https://doi.org/10.1149/2.0411714jes.
(79) Ringsby, A. J.; Fong, K. D.; Self, J.; Bergstrom, H. K.; McCloskey, B. D.; Persson, K. A. Transport Phenomena in Low Temperature Lithium-Ion Battery Electrolytes. *J. Electrochem. Soc.* **2021**, *168* (8), 080501. https://doi.org/10.1149/1945-7111/ac1735.
(80) Ma, L.; Glazier, S. L.; Petibon, R.; Xia, J.; Peters, J. M.; Liu, Q.; Allen, J.; Doig, R. N. C.; Dahn, J. R. A Guide to Ethylene Carbonate-Free Electrolyte Making for Li-Ion Cells. *J. Electrochem. Soc.* **2017**, *164* (1), A5008–A5018. https://doi.org/10.1149/2.0191701jes.
(81) Lazar, M. L.; Lucht, B. L. Carbonate Free Electrolyte for Lithium Ion Batteries Containing γ-Butyrolactone and Methyl Butyrate. *J. Electrochem. Soc.* **2015**, *162* (6), A928–A934. https://doi.org/10.1149/2.0601506jes.
(82) Petibon, R.; Harlow, J.; Le, D. B.; Dahn, J. R. The Use of Ethyl Acetate and Methyl Propanoate in Combination with Vinylene Carbonate as Ethylene Carbonate-Free Solvent Blends for Electrolytes in Li-Ion Batteries. *Electrochimica Acta* **2015**, *154*, 227–234. https://doi.org/10.1016/j.electacta.2014.12.084.
(83) Ma, X.; Li, J.; Glazier, S. L.; Ma, L.; Gering, K. L.; Dahn, J. R. A Study of Highly Conductive Ester Co-Solvents in Li[Ni0.5Mn0.3Co0.2]O2/Graphite Pouch Cells. *Electrochimica Acta* **2018**, *270*, 215–223. https://doi.org/10.1016/j.electacta.2018.03.006.
(84) Krachkovskiy, S. A.; Bazak, J. D.; Fraser, S.; Halalay, I. C.; Goward, G. R. Determination of Mass Transfer Parameters and Ionic Association of $LiPF_6$: Organic Carbonates Solutions. *J. Electrochem. Soc.* **2017**, *164* (4), A912–A916. https://doi.org/10.1149/2.1531704jes.
(85) Ding, M. S.; Xu, K.; Zhang, S. S.; Amine, K.; Henriksen, G. L.; Jow, T. R. Change of Conductivity with Salt Content, Solvent Composition, and Temperature for Electrolytes of LiPF6 in Ethylene Carbonate-Ethyl Methyl Carbonate. *J. Electrochem. Soc.* **2001**. https://doi.org/10.1149/1.1403730.
(86) Ehrl, A.; Landesfeind, J.; Wall, W. A.; Gasteiger, H. A. Determination of Transport Parameters in Liquid Binary Electrolytes: Part II. Transference Number. *J. Electrochem. Soc.* **2017**, *164* (12), A2716–A2731. https://doi.org/10.1149/2.1681712jes.
(87) Nyman, A.; Behm, M.; Lindbergh, G. Electrochemical Characterisation and Modelling of the Mass Transport Phenomena in LiPF6–EC–EMC Electrolyte. *Electrochimica Acta* **2008**, *53* (22), 6356–6365. https://doi.org/10.1016/j.electacta.2008.04.023.

(88) Rabette, C.; Tekaya, I.; Farkhondeh, M.; Fleutot, B.; Delacourt, C. Determination of Electrolyte Transport Properties with a Multi-Reference-Electrode Cell. *J. Electrochem. Soc.* **2021**, *168* (6), 060509. https://doi.org/10.1149/1945-7111/ac03f1.
(89) Hickson, D. T.; Halat, D. M.; Ho, A. S.; Reimer, J. A.; Balsara, N. P. Complete Characterization of a Lithium Battery Electrolyte Using a Combination of Electrophoretic NMR and Electrochemical Methods. *Phys. Chem. Chem. Phys.* **2022**, *24* (43), 26591–26599. https://doi.org/10.1039/D2CP02622H.
(90) Chakraborty, S.; Halat, D. M.; Im, J.; Hickson, D. T.; Reimer, J. A.; Balsara, N. P. Lithium Transference in Electrolytes with Star-Shaped Multivalent Anions Measured by Electrophoretic NMR. *Phys. Chem. Chem. Phys.* **2023**, *25* (31), 21065–21073. https://doi.org/10.1039/D3CP00923H.
(91) Fang, Y.; Yushmanov, P. V.; Furó, I. Improved Accuracy and Precision in Electrophoretic NMR Experiments. Current Control and Sample Cell Design. *J. Magn. Reson.* **2020**, *318*, 106796. https://doi.org/10.1016/j.jmr.2020.106796.
(92) Jerschow, A.; Müller, N. Convection Compensation in Gradient Enhanced Nuclear Magnetic Resonance Spectroscopy. *J. Magn. Reson.* **1998**, *132* (1), 13–18. https://doi.org/10.1006/jmre.1998.1400.
(93) He, Q.; Wei, Z. Convection Compensated Electrophoretic NMR. *J. Magn. Reson.* **2001**, *150* (2), 126–131. https://doi.org/10.1006/jmre.2001.2321.
(94) Pettersson, E.; Furó, I.; Stilbs, P. On Experimental Aspects of Electrophoretic NMR: Experimental Electrophoretic NMR. *Concepts Magn. Reson. Part A* **2004**, *22A* (2), 61–68. https://doi.org/10.1002/cmr.a.20012.
(95) Robinson, R. A.; Stokes, R. H. *Electrolyte Solutions*, 2nd rev. ed.; Dover Publications: Mineola, NY, 2002.
(96) Schreiner, C.; Zugmann, S.; Hartl, R.; Gores, H. J. Fractional Walden Rule for Ionic Liquids: Examples from Recent Measurements and a Critique of the So-Called Ideal KCl Line for the Walden Plot. *J. Chem. Eng. Data* **2010**, *55* (5), 1784–1788. https://doi.org/10.1021/je900878j.
(97) Walden, P. Über Organische Lösungs- Und Ionisierungsmittel: III. Teil: Innere Reibung Und Deren Zusammenhang Mit Dem Leitvermögen. *Z. Für Phys. Chem.* **1906**, *55U* (1), 207–249. https://doi.org/10.1515/zpch-1906-5511.
(98) Apelblat, A. Limiting Conductances of Electrolytes and the Walden Product in Mixed Solvents in a Phenomenological Approach. *J. Phys. Chem. B* **2008**, *112* (23), 7032–7044. https://doi.org/10.1021/jp802113v.
(99) Ue, M.; Mori, S. Mobility and Ionic Association of Lithium Salts in a Propylene Carbonate-Ethyl Methyl Carbonate Mixed Solvent. *J. Electrochem. Soc.* **1995**, *142* (8), 2577–2581. https://doi.org/10.1149/1.2050056.
(100) Webber, A. Conductivity and Viscosity of Solutions of LiCF3 SO 3, Li (CF 3 SO 2) 2 N , and Their Mixtures. *J. Electrochem. Soc.* **1991**, *138* (9), 2586–2590. https://doi.org/10.1149/1.2087287.
(101) Frenck, L.; Veeraraghavan, V. D.; Maslyn, J. A.; Balsara, N. P. Comparing Measurement of Limiting Current in Block Copolymer Electrolytes as a Function of Salt Concentration with Theoretical Predictions. *Electrochimica Acta* **2022**, *409*, 139911. https://doi.org/10.1016/j.electacta.2022.139911.
(102) Shah, D. B.; Kim, H. K.; Nguyen, H. Q.; Srinivasan, V.; Balsara, N. P. Comparing Measurements of Limiting Current of Electrolytes with Theoretical Predictions up to the

Solubility Limit. *J. Phys. Chem. C* **2019**, *123* (39), 23872–23881. https://doi.org/10.1021/acs.jpcc.9b07121.
(103) Stolz, L.; Hochstädt, S.; Röser, S.; Hansen, M. R.; Winter, M.; Kasnatscheew, J. Single-Ion *versus* Dual-Ion Conducting Electrolytes: The Relevance of Concentration Polarization in Solid-State Batteries. *ACS Appl. Mater. Interfaces* **2022**, *14* (9), 11559–11566. https://doi.org/10.1021/acsami.2c00084.
(104) Mistry, A.; Yu, Z.; Peters, B. L.; Fang, C.; Wang, R.; Curtiss, L. A.; Balsara, N. P.; Cheng, L.; Srinivasan, V. Toward Bottom-Up Understanding of Transport in Concentrated Battery Electrolytes. *ACS Cent. Sci.* **2022**, *8* (7), 880–890. https://doi.org/10.1021/acscentsci.2c00348.
(105) Mistry, A.; Srinivasan, V.; Steinrück, H. Characterizing Ion Transport in Electrolytes via Concentration and Velocity Profiles. *Adv. Energy Mater.* **2023**, *13* (9), 2203690. https://doi.org/10.1002/aenm.202203690.
(106) Klett, M.; Giesecke, M.; Nyman, A.; Hallberg, F.; Lindström, R. W.; Lindbergh, G.; Furó, I. Quantifying Mass Transport during Polarization in a Li Ion Battery Electrolyte by in Situ ^{7} Li NMR Imaging. *J. Am. Chem. Soc.* **2012**, *134* (36), 14654–14657. https://doi.org/10.1021/ja305461j.
(107) Gribble, D. A.; Frenck, L.; Shah, D. B.; Maslyn, J. A.; Loo, W. S.; Mongcopa, K. I. S.; Pesko, D. M.; Balsara, N. P. Comparing Experimental Measurements of Limiting Current in Polymer Electrolytes with Theoretical Predictions. *J. Electrochem. Soc.* **2019**, *166* (14), A3228–A3234. https://doi.org/10.1149/2.0391914jes.
(108) Diederichsen, K. M.; McShane, E. J.; McCloskey, B. D. Promising Routes to a High Li^{+} Transference Number Electrolyte for Lithium Ion Batteries. *ACS Energy Lett.* **2017**, *2* (11), 2563–2575. https://doi.org/10.1021/acsenergylett.7b00792.
(109) Mynam, M.; Kumari, S.; Ravikumar, B.; Rai, B. Effect of Temperature on Concentrated Electrolytes for Advanced Lithium Ion Batteries. *J. Chem. Phys.* **2021**, *154* (21), 214503. https://doi.org/10.1063/5.0049259.
(110) Lundgren, H.; Behm, M.; Lindbergh, G. Electrochemical Characterization and Temperature Dependency of Mass-Transport Properties of $LiPF_6$ in EC:DEC. *J. Electrochem. Soc.* **2015**, *162* (3), A413–A420. https://doi.org/10.1149/2.0641503jes.
(111) Gering, Kevin L.; Tien Q. Duong. Prediction of Electrolyte Transport Properties Using a Solvation-Based Chemical Physics Model., 2003.
(112) Hall, D. S.; Self, J.; Dahn, J. R. Dielectric Constants for Quantum Chemistry and Li-Ion Batteries: Solvent Blends of Ethylene Carbonate and Ethyl Methyl Carbonate. *J. Phys. Chem. C* **2015**, *119* (39), 22322–22330. https://doi.org/10.1021/acs.jpcc.5b06022.
(113) Fang, C.; Halat, D. M.; Mistry, A.; Reimer, J. A.; Balsara, N. P.; Wang, R. Quantifying Selective Solvent Transport under an Electric Field in Mixed-Solvent Electrolytes. *Chem. Sci.* **2023**, *14* (20), 5332–5339. https://doi.org/10.1039/D3SC01158E.
(114) Hou, T.; Fong, K. D.; Wang, J.; Persson, K. A. The Solvation Structure, Transport Properties and Reduction Behavior of Carbonate-Based Electrolytes of Lithium-Ion Batteries. *Chem. Sci.* **2021**, *12* (44), 14740–14751. https://doi.org/10.1039/D1SC04265C.
(115) Mistry, A.; Grundy, L. S.; Halat, D. M.; Newman, J.; Balsara, N. P.; Srinivasan, V. Effect of Solvent Motion on Ion Transport in Electrolytes. *J. Electrochem. Soc.* **2022**, *169* (4), 040524. https://doi.org/10.1149/1945-7111/ac6329.
(116) Grundy, L. S.; Galluzzo, M. D.; Loo, W. S.; Fong, A. Y.; Balsara, N. P.; Takacs, C. J. Inaccessible Polarization-Induced Phase Transitions in a Block Copolymer Electrolyte: An

Unconventional Mechanism for the Limiting Current. *Macromolecules* **2022**, *55* (17), 7637–7649. https://doi.org/10.1021/acs.macromol.2c00922.
(117) Chang, H. J.; Ilott, A. J.; Trease, N. M.; Mohammadi, M.; Jerschow, A.; Grey, C. P. Correlating Microstructural Lithium Metal Growth with Electrolyte Salt Depletion in Lithium Batteries Using ^{7} Li MRI. *J. Am. Chem. Soc.* **2015**, *137* (48), 15209–15216. https://doi.org/10.1021/jacs.5b09385.
(118) Bazak, J. D.; Allen, J. P.; Krachkovskiy, S. A.; Goward, G. R. Mapping of Lithium-Ion Battery Electrolyte Transport Properties and Limiting Currents with In Situ MRI. *J. Electrochem. Soc.* **2020**, *167* (14), 140518. https://doi.org/10.1149/1945-7111/abc0c9.
(119) Sethi, G. K.; Frenck, L.; Sawhney, S.; Chakraborty, S.; Villaluenga, I.; Balsara, N. P. Effect of Microphase Separation on the Limiting Current Density in Hybrid Organic-Inorganic Copolymer Electrolytes. *Solid State Ion.* **2021**, *368*, 115702. https://doi.org/10.1016/j.ssi.2021.115702.
(120) Chazalviel, J.-N. Electrochemical Aspects of the Generation of Ramified Metallic Electrodeposits. *Phys. Rev. A* **1990**, *42* (12), 7355–7367. https://doi.org/10.1103/PhysRevA.42.7355.
(121) Bai, P.; Li, J.; Brushett, F. R.; Bazant, M. Z. Transition of Lithium Growth Mechanisms in Liquid Electrolytes. *Energy Environ. Sci.* **2016**, *9* (10), 3221–3229. https://doi.org/10.1039/C6EE01674J.
(122) Walls, H. J. Anion and Cation Transference Numbers Determined by Electrophoretic NMR of Polymer Electrolytes Sum to Unity. *Electrochem. Solid-State Lett.* **1999**, *3* (7), 321. https://doi.org/10.1149/1.1391136.
(123) Hickson, D. T.; Im, J.; Halat, D. M.; Karvat, A.; Reimer, J. A.; Balsara, N. P. Low-Temperature Characterization of a Nonaqueous Liquid Electrolyte for Lithium Batteries. *J. Electrochem. Soc.* **2024**, *171* (3), 030514. https://doi.org/10.1149/1945-7111/ad2d91.
(124) Zhang, Z.; Madsen, L. A. Observation of Separate Cation and Anion Electrophoretic Mobilities in Pure Ionic Liquids. *J. Chem. Phys.* **2014**, *140* (8), 084204. https://doi.org/10.1063/1.4865834.
(125) Zhao, Q.; Zhang, Y.; Sun, G.; Cong, L.; Sun, L.; Xie, H.; Liu, J. Binary Mixtures of Highly Concentrated Tetraglyme and Hydrofluoroether as a Stable and Nonflammable Electrolyte for Li–O $_{2}$ Batteries. *ACS Appl. Mater. Interfaces* **2018**, *10* (31), 26312–26319. https://doi.org/10.1021/acsami.8b08346.
(126) Chen, J.; Chen, C.; Huang, T.; Yu, A. LiTFSI Concentration Optimization in TEGDME Solvent for Lithium–Oxygen Batteries. *ACS Omega* **2019**, *4* (24), 20708–20714. https://doi.org/10.1021/acsomega.9b02941.
(127) Carvalho, P. J.; Fonseca, C. H. G.; Moita, M.-L. C. J.; Santos, Â. F. S.; Coutinho, J. A. P. Thermophysical Properties of Glycols and Glymes. *J. Chem. Eng. Data* **2015**, *60* (12), 3721–3737. https://doi.org/10.1021/acs.jced.5b00662.
(128) Hoffman, Z. J.; Shah, D. B.; Balsara, N. P. Temperature and Concentration Dependence of the Ionic Transport Properties of Poly(Ethylene Oxide) Electrolytes. *Solid State Ion.* **2021**, *370*, 115751. https://doi.org/10.1016/j.ssi.2021.115751.
(129) Villaluenga, I.; Pesko, D. M.; Timachova, K.; Feng, Z.; Newman, J.; Srinivasan, V.; Balsara, N. P. Negative Stefan-Maxwell Diffusion Coefficients and Complete Electrochemical Transport Characterization of Homopolymer and Block Copolymer Electrolytes. *J. Electrochem. Soc.* **2018**, *165* (11), A2766–A2773. https://doi.org/10.1149/2.0641811jes.

(130) Zhang, Y.; Zuo, T.-T.; Popovic, J.; Lim, K.; Yin, Y.-X.; Maier, J.; Guo, Y.-G. Towards Better Li Metal Anodes: Challenges and Strategies. *Mater. Today* **2020**, *33*, 56–74. https://doi.org/10.1016/j.mattod.2019.09.018.
(131) He, X.; Bresser, D.; Passerini, S.; Baakes, F.; Krewer, U.; Lopez, J.; Mallia, C. T.; Shao-Horn, Y.; Cekic-Laskovic, I.; Wiemers-Meyer, S.; Soto, F. A.; Ponce, V.; Seminario, J. M.; Balbuena, P. B.; Jia, H.; Xu, W.; Xu, Y.; Wang, C.; Horstmann, B.; Amine, R.; Su, C.-C.; Shi, J.; Amine, K.; Winter, M.; Latz, A.; Kostecki, R. The Passivity of Lithium Electrodes in Liquid Electrolytes for Secondary Batteries. *Nat. Rev. Mater.* **2021**, *6* (11), 1036–1052. https://doi.org/10.1038/s41578-021-00345-5.
(132) Yamada, Y.; Yamada, A. Review—Superconcentrated Electrolytes for Lithium Batteries. *J. Electrochem. Soc.* **2015**, *162* (14), A2406–A2423. https://doi.org/10.1149/2.0041514jes.
(133) Yamada, Y.; Wang, J.; Ko, S.; Watanabe, E.; Yamada, A. Advances and Issues in Developing Salt-Concentrated Battery Electrolytes. *Nat. Energy* **2019**, *4* (4), 269–280. https://doi.org/10.1038/s41560-019-0336-z.
(134) Borodin, O.; Self, J.; Persson, K. A.; Wang, C.; Xu, K. Uncharted Waters: Super-Concentrated Electrolytes. *Joule* **2020**, *4* (1), 69–100. https://doi.org/10.1016/j.joule.2019.12.007.
(135) Giffin, G. A. The Role of Concentration in Electrolyte Solutions for Non-Aqueous Lithium-Based Batteries. *Nat. Commun.* **2022**, *13* (1), 5250. https://doi.org/10.1038/s41467-022-32794-z.
(136) Sayah, S.; Ghosh, A.; Baazizi, M.; Amine, R.; Dahbi, M.; Amine, Y.; Ghamouss, F.; Amine, K. How Do Super Concentrated Electrolytes Push the Li-Ion Batteries and Supercapacitors beyond Their Thermodynamic and Electrochemical Limits? *Nano Energy* **2022**, *98*, 107336. https://doi.org/10.1016/j.nanoen.2022.107336.
(137) Yamada, Y.; Furukawa, K.; Sodeyama, K.; Kikuchi, K.; Yaegashi, M.; Tateyama, Y.; Yamada, A. Unusual Stability of Acetonitrile-Based Superconcentrated Electrolytes for Fast-Charging Lithium-Ion Batteries. *J. Am. Chem. Soc.* **2014**, *136* (13), 5039–5046. https://doi.org/10.1021/ja412807w.
(138) Qian, J.; Henderson, W. A.; Xu, W.; Bhattacharya, P.; Engelhard, M.; Borodin, O.; Zhang, J.-G. High Rate and Stable Cycling of Lithium Metal Anode. *Nat. Commun.* **2015**, *6* (1), 6362. https://doi.org/10.1038/ncomms7362.
(139) Suo, L.; Borodin, O.; Gao, T.; Olguin, M.; Ho, J.; Fan, X.; Luo, C.; Wang, C.; Xu, K. "Water-in-Salt" Electrolyte Enables High-Voltage Aqueous Lithium-Ion Chemistries. *Science* **2015**, *350* (6263), 938–943. https://doi.org/10.1126/science.aab1595.
(140) Xie, J.-D.; Liu, W.-J.; Li, C.; Patra, J.; Gandomi, Y. A.; Dong, Q.-F.; Chang, J.-K. Superior Coulombic Efficiency of Lithium Anodes for Rechargeable Batteries Utilizing High-Concentration Ether Electrolytes. *Electrochimica Acta* **2019**, *319*, 625–633. https://doi.org/10.1016/j.electacta.2019.07.020.
(141) Zheng, J.; Kim, M. S.; Tu, Z.; Choudhury, S.; Tang, T.; Archer, L. A. Regulating Electrodeposition Morphology of Lithium: Towards Commercially Relevant Secondary Li Metal Batteries. *Chem. Soc. Rev.* **2020**, *49* (9), 2701–2750. https://doi.org/10.1039/C9CS00883G.
(142) Lundgren, H.; Scheers, J.; Behm, M.; Lindbergh, G. Characterization of the Mass-Transport Phenomena in a Superconcentrated LiTFSI:Acetonitrile Electrolyte. *J. Electrochem. Soc.* **2015**, *162* (7), A1334–A1340. https://doi.org/10.1149/2.0961507jes.

(143) Zheng, X.; Huang, L.; Ye, X.; Zhang, J.; Min, F.; Luo, W.; Huang, Y. Critical Effects of Electrolyte Recipes for Li and Na Metal Batteries. *Chem* **2021**, *7* (9), 2312–2346. https://doi.org/10.1016/j.chempr.2021.02.025.
(144) Halat, D. M.; Mistry, A.; Hickson, D.; Srinivasan, V.; Balsara, N. P.; Reimer, J. A. Transference Number of Electrolytes from the Velocity of a Single Species Measured by Electrophoretic NMR. *J. Electrochem. Soc.* **2023**, *170* (3), 030535. https://doi.org/10.1149/1945-7111/acbee7.
(145) Ueno, K.; Murai, J.; Ikeda, K.; Tsuzuki, S.; Tsuchiya, M.; Tatara, R.; Mandai, T.; Umebayashi, Y.; Dokko, K.; Watanabe, M. Li^+ Solvation and Ionic Transport in Lithium Solvate Ionic Liquids Diluted by Molecular Solvents. *J. Phys. Chem. C* **2016**, *120* (29), 15792–15802. https://doi.org/10.1021/acs.jpcc.5b11642.
(146) Fang, C.; Halat, D. M.; Balsara, N. P.; Wang, R. Dynamic Heterogeneity of Solvent Motion and Ion Transport in Concentrated Electrolytes. *J. Phys. Chem. B* **2023**, *127* (8), 1803–1810. https://doi.org/10.1021/acs.jpcb.2c08029.
(147) Deep B. Shah. Ion Transport Properties in Novel and Traditional Liquid Electrolytes for Lithium-Based Batteries, University of California, Berkeley, Berkeley, 2019.
(148) Zugmann, S.; Fleischmann, M.; Amereller, M.; Gschwind, R. M.; Wiemhöfer, H. D.; Gores, H. J. Measurement of Transference Numbers for Lithium Ion Electrolytes via Four Different Methods, a Comparative Study. *Electrochimica Acta* **2011**, *56* (11), 3926–3933. https://doi.org/10.1016/j.electacta.2011.02.025.
(149) Scrosati, B. Power Sources for Portable Electronics and Hybrid Cars: Lithium Batteries and Fuel Cells. *Chem. Rec.* **2005**, *5* (5), 286–297. https://doi.org/10.1002/tcr.20054.
(150) Saito, S.; Watanabe, H.; Ueno, K.; Mandai, T.; Seki, S.; Tsuzuki, S.; Kameda, Y.; Dokko, K.; Watanabe, M.; Umebayashi, Y. Li^+ Local Structure in Hydrofluoroether Diluted Li-Glyme Solvate Ionic Liquid. *J. Phys. Chem. B* **2016**, *120* (13), 3378–3387. https://doi.org/10.1021/acs.jpcb.5b12354.
(151) Saito, M.; Yamada, S.; Ishikawa, T.; Otsuka, H.; Ito, K.; Kubo, Y. Factors Influencing Fast Ion Transport in Glyme-Based Electrolytes for Rechargeable Lithium–Air Batteries. *RSC Adv* **2017**, *7* (77), 49031–49040. https://doi.org/10.1039/C7RA07501D.